

**Image and Signal Processing  
in  
Intravascular Ultrasound**

This dissertation was prepared at the laboratory of Experimental Echocardiography, Erasmus University Rotterdam, The Netherlands.

The studies presented in this dissertation were financially supported by the Interuniversity Cardiology Institute of the Netherlands (ICIN), the Dutch Technology Foundation (STW) and the Netherlands Heart Foundation (NHS).

ISBN: 90-9010679-0

Cover illustrations

*Top: In vivo IVUS images with color flow mapping showing changes in blood velocities during a cardiac cycle (from left to right: low, medium and high flow rates).*

*Middle: Corresponding IVUS image with derived luminal contour.*

*Bottom: Volume flow plotted as a function of time showing cyclic changes of the flow rate. Corresponding cardiac phases of three color flow images are shown with dots in the curve.*

Printed by: Ridderprint B.V., Ridderkerk.

**IMAGE AND SIGNAL PROCESSING IN  
INTRAVASCULAR ULTRASOUND**

BEELD- EN SIGNAALVERWERKING IN  
INTRAVASCULAIR ULTRAGELUID

**PROEFSCHRIFT**

ter verkrijging van de graad van doctor  
aan de Erasmus Universiteit Rotterdam  
op gezag van de rector magnificus  
Prof. Dr P.W.C. Akkermans M.A.  
en volgens besluit van het college voor promoties

De openbare verdediging zal plaatsvinden op  
vrijdag, 27 juni 1997 om 16 uur

door

**WENGUANG LI**  
geboren te Guangzhou, P.R. China

## PROMOTIECOMMISSIE

Promotores: Prof. Dr Ir N. Bom  
Prof. Dr J.R.T.C. Roelandt  
Dr Ir A.F.W. van der Steen (tevens co-promotor)

Overige leden: Prof. Dr Ir J.H.C. Reiber  
Prof. Dr Ir A.P.G. Hoeks  
Prof. Dr H. van Urk



Financial support by the Netherlands Heart Foundation (NHS) and the Interuniversity Cardiology Institute of the Netherlands (ICIN) for the publication of this thesis is gratefully acknowledged.

Also, financial contributions of Cardialysis B.V., EndoSonics Europe B.V. and TomTec Imaging Systems GmbH are gratefully acknowledged.

君子曰：學不可以已。青，取之于藍，而青于藍；冰，水為之，而寒于水。

故不登高山，不知天之高也；不臨深峪，不知地之厚也；不聞先王之遺言，不知學問之大也。

摘自 荀況《勸學篇》 *Xun Zi, On Learning.*



|   |           |
|---|-----------|
| <b>CHAPTER 1.....</b>   | <b>1</b>  |
| <b>Introduction</b>   |           |
| <b>CHAPTER 2.....</b>   | <b>19</b> |
| <b>Validation of quantitative analysis of intravascular ultrasound images</b>   |           |
| <i>W. Li, E. J. Gussenhoven, Y. Zhong, S. H. K. The, C. Di Mario, S. Madretsma, F. van Egmond, P. de Feyter, H. Pieterman, H. van Urk, H. Rijsterborgh, N. Bom.</i>                                 |           |
| <b>CHAPTER 3.....</b>   | <b>33</b> |
| <b>Semi-automatic frame-to-frame tracking of the luminal border from Intravascular ultrasound: Technical development and clinical applications</b>  |           |
| <i>W. Li, S.H.K. The, R.A. Wilson, J. G. Bosch, E.J. Gussenhoven, C. Di Mario, J.H.C. Reiber, N. Bom, P.D. Verdouw, J.R.T.C. Roelandt.</i>  |           |
| <b>CHAPTER 4.....</b>   | <b>47</b> |
| <b>Three-dimensional reconstruction and volumetric quantification of intravascular ultrasound</b>   |           |
| <i>W. Li, C. von Birgelen, A. Harlooper, A. van der Lugt, F.C. van Egmond, C. Di Mario, E. Boersma, N. van der Putten, J. G. Bosch, E.J. Gussenhoven, J.H.C. Reiber, N. Bom, J.R.T.C. Roelandt.</i> |           |
| <b>CHAPTER 5.....</b>   | <b>69</b> |
| <b>Morphometric analysis in three-dimensional intracoronary ultrasound: An in vitro and in vivo study using a novel system for the contour detection of lumen and plaque</b>                        |           |
| <i>C. von Birgelen, C. Di Mario, W. Li, J.C.H. Schuurbijs, C.J. Slager, P.J. de Feyter, P.W. Serruys, J.R.T.C. Roelandt.</i>  |           |
| <b>CHAPTER 6.....</b>   | <b>91</b> |
| <b>Temporal averaging for quantification of lumen dimensions in intravascular ultrasound images</b>   |           |
| <i>W. Li, E.J. Gussenhoven, Y. Zhong, S.H.K. The, H. Pieterman, H. van Urk, N. Bom.</i>   |           |

**CHAPTER 7.....103**

**Temporal correlation of blood scattering signals in vivo from radio frequency intravascular ultrasound**

*W. Li, A.F.W. van der Steen, C.T. Lancée, J. Honkoop, E. J. Gussenhoven, N. Bom.*

**CHAPTER 8.....119**

**Decorrelation properties of intravascular echo signals**

*W. Li, C.T. Lancée, E.I. Céspedes, A.F.W. van der Steen, N. Bom.*

**CHAPTER 9.....139**

**Estimation of local blood velocity and volume flow with intravascular ultrasound**

*W. Li, A.F.W. van der Steen, C.T. Lancée, E.I. Céspedes, E. J. Gussenhoven, N Bom.*

**CHAPTER 10.....163**

**Summary**

**Samenvatting**

**APPENDIX I: MINIMUM COST ALGORITHM ..... A - 1**

**APPENDIX II: IMPULSE RESPONSE MODEL..... A - 5**

**ACKNOWLEDGEMENTS ..... A-11**

**PUBLICATIONS..... A-13**

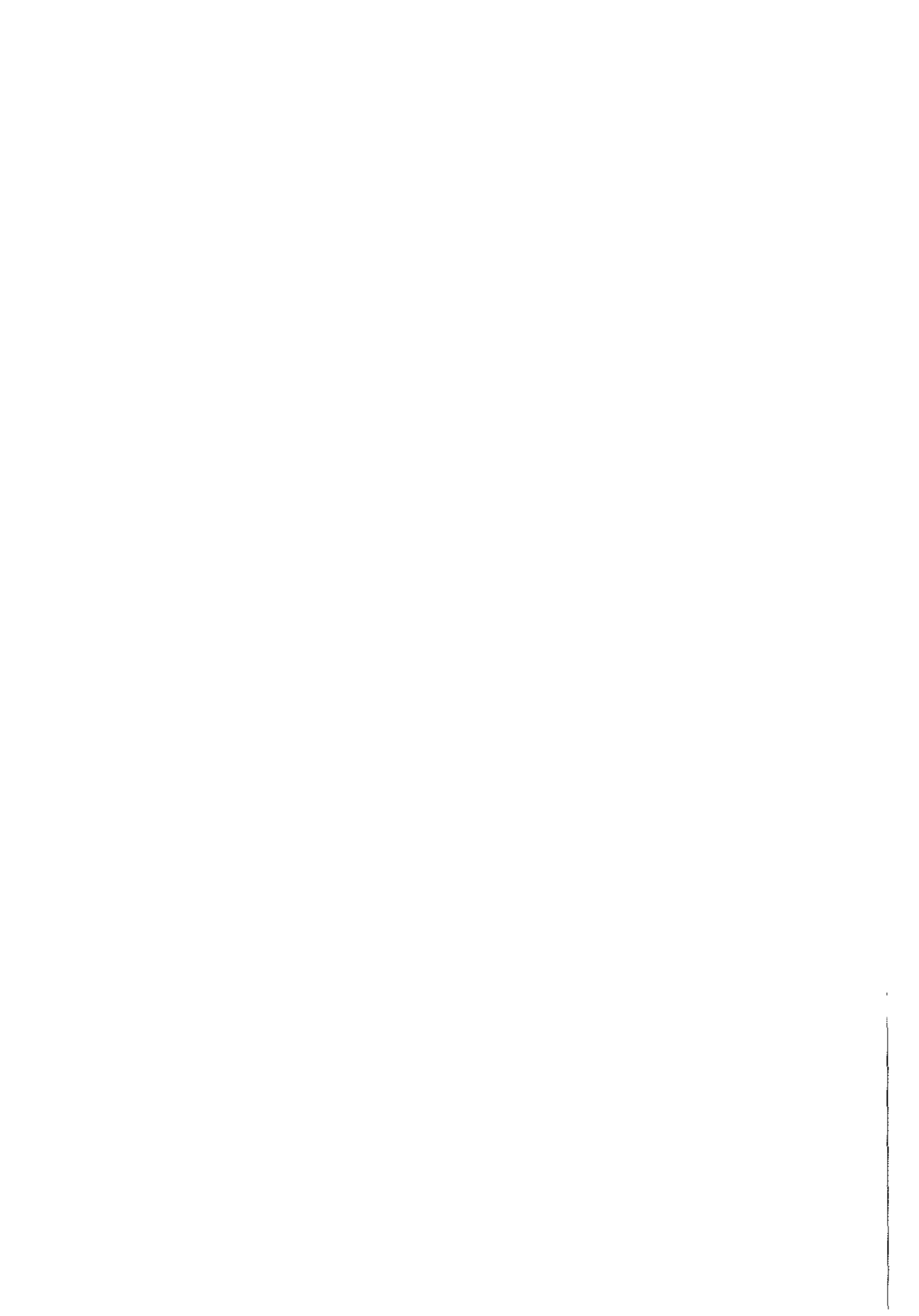
**CURRICULUM VITAE..... A-21**



## CHAPTER 1

---

### INTRODUCTION



Intravascular ultrasound (IVUS) is a new imaging modality providing real-time, cross-sectional, high-resolution images of the arterial lumen and vessel wall. In contrast to conventional x-ray angiography that only displays silhouette views of the vessel lumen, IVUS imaging permits visualization of lesion morphology and accurate measurements of arterial cross-sectional dimensions in patients. These unique capabilities have led to many important clinical applications including quantitative assessment of the severity, restenosis, progression of atherosclerosis [1-6], selection and guidance of catheter-based therapeutic procedures and short- and long-term evaluation of the outcome of an intravascular intervention [7-12].

Like the progress of other medial imaging modalities, the advent of IVUS techniques has brought in new challenges in the field of signal and image processing. Quantitative analysis of IVUS images requires the identification of arterial structures such as the lumen and plaque within an image. Manual contour tracing is well known to be time consuming and subjective. Development of an automated contour detection method may improve the reproducibility of quantitative IVUS and avoid a tedious manual procedure. Computerized three-dimensional (3D) reconstruction of an IVUS image series may extend the tomographic data to a more powerful volumetric assessment of the vessel segment. Obviously, this could not be achieved without the advance of 3D image processing techniques. Furthermore, it is demonstrated that processing of the original radio frequency (RF) echo signals provides an efficient means to improve the IVUS image quality as well as a new approach to extract volumetric flow information. The goals of the studies reported in this thesis are therefore directed toward development of video image and RF signal processing techniques for image enhancement, automated contour detection, 3D reconstruction and flow imaging.

In this chapter several IVUS scanning mechanisms and some background information about ultrasonic imaging are briefly introduced. The principles of different video-based contour detection approaches and examples of contour detection in echocardiograms are discussed. Subsequently, applications of RF analysis in IVUS images are reviewed, followed by the scope of this thesis in the final part.

## **1 INTRAVASCULAR SCANNING**

Cross-sectional imaging of a vessel is generated by sweeping the ultrasound beam sequentially in a 360° scan angle. Technical details of different scanning mechanism for intravascular imaging have been discussed by Bom and co-workers [13]. Briefly, current IVUS systems are based either on mechanical scan with a single element transducer or on electronical scan with a circular phased array.

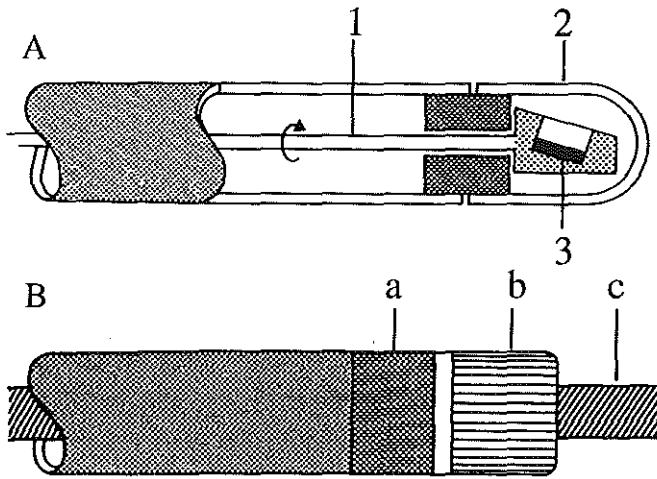


*Fig. 1. A, Mechanical rotating single-element catheter tip consisting of 1) rotating shaft; 2) transparent dome; 3) transducer element. B, Electronically switched phased array catheter tip consisting of a) integrated circuitry for reduction of the number of wires; b) multi-element transducer; 3) guide wire.*

In mechanical system real-time imaging is generated by rotating a single element transducer with a flexible drive shaft (Fig. 1a). Alternatively, a rotating mirror can be used to direct the beam to all angular positions. One advantage of mechanical systems is that the water path between the transducer and the dome minimizes the ring-down effect and interference in the extreme near-field. The mechanical nature of these methods, however, may introduce image artifacts when the catheter is bended in a severely curved vessel.

By mounting a large number of small transducer elements cylindrically at the circumference of a catheter tip, the ultrasound beam can be steered electronically to form a cross-sectional scan (Fig. 1b). The advantage of an electronically steering system is the absence of any mechanical image distortion as above-discussed and the possibility to introduce a central guide wire. Although initial image quality of the electrical scanning systems was poor, more recent catheters using synthetic phased arrays have shown a considerable improvement in image quality.

## 2 IMAGING SYSTEM

A typical 30 MHz mechanical scanning system (Du-Med, Rotterdam, The Netherlands) contains several signal processing blocks as illustrated in Fig. 2. The motor that rotates a drive-shaft inside the echo catheter is built in a portable unit called motor unit. This unit needs to be situated at the bed-site next the patient, whereas the main frame is

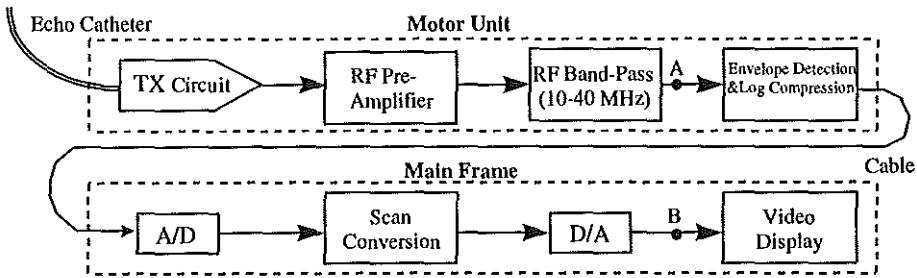


Fig. 2. Block diagram of an IVUS imaging system. The motor unit is isolated from the main frame by an electro-optical cable connection. Point A and B indicate the signal interfaces for RF and video image processing, respectively.

usually positioned outside the sterile zone. The signal interface for analysis of RF data is provided after the band-pass amplifier. The digital scan conversion circuitry displays an ultrasound image in a standard video format.

### *Spatial resolution*

The spatial resolution of an ultrasound imaging system is defined as the reciprocal of the minimum distance between two small targets, which can be specified in three directions: axial, lateral and elevational resolution. The axial (range) resolution defined along the beam direction depends mainly on the length of the ultrasound pulse that is inversely proportional to the central ultrasound frequency of a transducer. Thus, the use of higher ultrasound frequencies yields a finer image resolution. An axial resolution of better than 100  $\mu\text{m}$  can be achieved using 30 MHz central frequency with 20 MHz bandwidth.

The lateral (azimuthal) resolution is related to the beam width within the scan plane, whereas the elevational resolution is determined by the beam width perpendicular to the scan plane. Since the beam width is range dependent, these two resolutions may vary in different scan depths. For 3D reconstruction, the resolution in elevation defines the minimum thickness of an echographic slice.

### *Temporal resolution*

The temporal resolution is determined by the image frame rate in two-dimensional (2D) imaging. A complete cross-sectional scan is made up of a number of individual scan lines. Therefore, the maximum frame rate depends on the required line number and the time to build a scan line. In a mechanical IVUS imaging system, the frame rate is limited by the maximum rotation speed of a driving unit. For instance, the motor unit

with a maximum speed specified for 1000 rpm produces a scan rate of 16 frames/second.

### 3 INTERACTIONS OF ULTRASOUND WITH BIOLOGICAL MEDIUM

The interaction of a propagating sound wave with tissue or blood yields the echo signal which can be detected by a transducer to generate an ultrasound image. Attenuation, reflection/refraction and scattering are some commonly observed effects with which the appearance of an echo image is closely associated [14].

#### *Reflection*

When an ultrasound wave travels across the boundary between two types of media, part of the wave is reflected at the interface while the rest of the wave propagates through the second medium. The ratio between the reflected sound intensity and the intensity that continues on is related to the difference in the acoustic impedance  $Z$ . If the size of the reflecting interface is much larger than the wavelength of incident sound, specular reflection occurs in which the reflected wave intensity is given by

$$I_r = I_i \left[ \frac{Z_2 - Z_1}{Z_2 + Z_1} \right]^2,$$

where  $I_i$  is the intensity of the incident sound and  $Z_1$  and  $Z_2$  are the impedance of the first and second medium, respectively. The intensity relation indicates that if the ratio of  $Z_1$  and  $Z_2$  is  $\ll 1$ , the majority of the sound wave power is bounced back with minimal energy penetrating through the boundary. This explains why a calcified lesion often presents as a strong echo accompanied by a post acoustic shadow, owing to a significant change in the impedance from tissue to calcium.

#### *Scattering*

A scattering process occurs when an ultrasound medium contains a lot of fine structures or small particles that have a size much smaller than the wavelength of incident sound waves. In this circumstance, each structure or particle (scatterer) acts as an independent source that radiates the sound wave in all directions. The received signal is the summation of the responses of all individual scatterers back onto the transducer surface (backscatter). Since the spatial distribution of these scatterers is mostly random, the summation of two scattered sound waves can either increase (constructive interference) or decrease (destructive interference) the added amplitude, depending on their relative positions towards the transducer. These random interference patterns result in amplitude variations in the received echo signals which are referred to as speckle or texture of the ultrasound image. In a fully developed

scattering process (Rayleigh scattering), the intensity of a scattered signal is proportional to the fourth power of the ultrasonic frequency. The distribution of echo amplitudes is characterized by Rayleigh distribution that has fixed signal (mean value) to noise (variance) ratio of 1.91. Although a perfect point scatterer does not exist in medical ultrasound imaging, the scattering process of soft tissue, soft lesion and blood is often approximated by a point scattering model.

#### **4 CONTOUR DETECTION IN ULTRASOUND IMAGES**

A contour or edge detection process that identifies the boundary of an object of interest is a key step towards automated quantitative analysis. This is often achieved by means of computerized processing of ultrasound images recorded in a video format. Three categories of image information can be used for extracting a contour from ultrasound images.

The first category is the changes in gray intensity between the object and background that yield an intensity boundary of the object. Gray scale parameters such as the mean, variance and gradient are the basic information for edge detection.

The second type of image information is the temporal feature of a sequence of echograms. It has been well acknowledged that, in addition to the intensity boundary, the dynamic motion of an object on real-time echo images provides an extra clue for recognizing the anatomic structures. Even when an object is hardly recognizable on the still-frame display due to a poor image quality, an experienced operator is still able to quickly estimate its location by reviewing the cineloop of the echo image sequence. Thus, a means of incorporating image data from several frames into computer processing may as well improve a contour detection algorithm.

The third information source is high-level knowledge about the object to be detected. For example, the prior knowledge about the shape, location and spatial relation of desired image objects can be used to guide a contour detection procedure.

The main challenge in contour detection of medical ultrasound images is the speckle noise, an inherent random intensity pattern caused by the scattering process of tissue or blood. A high level of speckle noises may mask the intensity boundary, resulting in a rather poor definition of the object border. Furthermore, drop-out of echo signals in parts of the object boundary also complicates contour detection in ultrasound images.

#### **5 CONTOUR DETECTION ALGORITHMS**

In general, contour detection algorithms in video image processing can be categorized into three types: parallel edge detection, sequential edge detection and methods based on global optimization [15-17]. In this section, the three contour detection methods are

briefly described and some applications in detection of the endocardial and epicardial boundaries in echocardiograms are reviewed.

### *Parallel detection*

In parallel edge detection, it is determined whether or not a pixel is the contour point on the basis of local information only. The decision is not affected by the processing results in other locations. Therefore, this technique may in principle be applied simultaneously everywhere in the image to find the complete object boundary. A classic parallel approach consists of 1) applying an edge operator to enhance the image boundary; 2) finding edge pixels by thresholding of the enhanced image data; 3) removing multiple edge points by a thinning algorithm; 4) linking the edge points to form a contour that encompasses all pixels of the object.

Skorton and co-workers described a parallel contour detection scheme based on a global gray threshold method [18]. Based on a similar approach, Collins et al. evaluated the performance of four different edge operators in measurements of excised hearts [19]. In addition to the use of a conventional edge operator, nonlinear morphologic processing [20] or a knowledge-based approach [21] was used to enhance a contour detection algorithm.

### *Sequential detection*

Sequential edge detection is based on the principle that the contour of a physical object should be continuous. When an edge point is identified, its successor is likely to be found in a nearby neighborhood. Consequently, the sequential approach search for one edge point at a time, which allows utilizing both local information and the result of the previously examined points for decision making. A typical implementation of the sequential approach is a radial search method for detection of an object with a closed and generally circular or elliptical shape, for example, the arterial lumen. The radial search approach may consist of 1) finding the object center to define a set of radii; 2) applying an edge operator; 3) searching for an edge point along the radius originated from the center. 4) combining all the radial edge points to form a contour. The advantage of a sequential approach is that a two-dimensional boundary detection problem is simplified to a one-dimensional search along a set of straight lines.

Many authors have exploited the radial search approach by incorporating temporal information of the echocardiographic sequence [22,24]. For example, Zhang et al. developed a method based on a temporal co-occurrence matrix derived by examining the between-frame changes in gray intensity [22]. Other methods such as utilizing a cost function to evaluate the goodness of an edge point [25,26], a two-stage image segmentation strategy based on global and local processing [27], a nonlinear



processing method in the edge linking procedure [28], and a fuzzy reasoning technique to mimic the human decision making procedure [29] were also proposed.

### *Optimization-based approaches*

Methods based on global optimization are in particular devised to cope with noisy images [30]. In contrast to the previous two methods, an optimization approach first examines all the possible contours for an expected object. The decision is then made based on some optimization rules to pick up an optimal contour. A global optimization approach often consists of 1) defining an approximated model for an object of interest; 2) evaluating every possible contour deviated from the pre-defined model, 3) determining the optimal contour by maximizing a merit function or by minimizing a cost function/energy function.

An example of the global optimization methods is the dynamic programming technique that utilizes a cost function to evaluate the merit of a trial contour. Unser et al. applied a template matching method for automated extraction of myocardial borders in M-mode echocardiograms [31]. By comparing different tracking algorithms, they demonstrated that the dynamic programming technique was the most effective algorithm. Friedland et al. proposed a global optimization approach for sequential image detection using simulated annealing [32]. Bosch and co-workers used the minimum-cost algorithm for detection of the endocardial boundary [33] and demonstrated the possibility of a real-time implementation of this method [34].

In summary, averaging or median filters were applied in most methods to reduce the speckle noise. Many efforts have been made in utilizing the temporal feature of an echographic sequence or the high-level knowledge of heart anatomy. In the above-discussed approaches, the global optimization based methods appeared to be the most robustness to speckle noise and echo drop-outs. Our development strategy for contour detection in IVUS images was therefore based on the global optimization process using the minimum-cost algorithm.

## **6 RADIO FREQUENCY SIGNAL PROCESSING**

Despite the fact that numerous algorithms have been developed, automated contour detection in medical ultrasound images has so far remained to be a difficult task. One inherent limitation of these approaches is that video imaging processing only utilizes the amplitude of the original RF signals; the phase information is removed by the demodulation process. It is well known that the constructive and destructive interference of individual scattering signals may cause changes in both amplitudes and phases of the received echo signals. Thus, processing of the original RF data should

provide a more efficient way to tackle the problem of speckle noise. The advantage of RF processing has been demonstrated in the fields of motion detection or tissue characterization, where an RF based approach is often shown more accurate and sensitive than analyzing video data. In this section, we shall review some of the RF signal processing methods for IVUS applications.

### *Acoustic properties*

Quantitative measurements of acoustic properties in blood and tissue provide fundamental knowledge for design of IVUS systems, interpretation of image data and development of tissue characterization techniques. Lockwood et al. measured the attenuation, backscatter and speed of sound of vascular tissue in vitro using a 35~65 MHz ultrasound backscatter microscope [35]. A high scattering level of blood was found that was within an order of magnitude comparable to the level measured in some tissue. De Kroon and co-workers studied the angle-dependent backscatter of the arterial wall [36] and integrated backscatter of whole blood as a function of shear stress [37] using a 30 MHz system. Their results indicated that quantitative tissue characterization based on integrated scatter could be complicated by the dependence on the angle of incidence. Foster et al. extended the measurement of whole blood in [35] to the frequencies of 30~70 MHz and found a strong dependence of the frequency-dependent backscatter and shear rate [38]. These measurements showed that Rayleigh scattering assumption does not hold as the wavelength of ultrasound sources approaches the size of blood scatterers, especially in a low shear rate where significant aggregates of the red cells occur.

### *Tissue characterization*

Ultrasonic tissue characterization methods have been developed for quantitative assessment of tissue types in different human organs such as heart [39-41], liver [42-44] and eye [45,46]. Recently, these methods have been applied in identification of arterial tissues using high frequency ultrasound. Wickline et al. applied the integrated backscatter measurement (the average power of the spectrum of an RF signal) in vitro to various vessels and demonstrated differentiation of fatty, fibrous and normal aortic intima was possible [47]. Wilson and co-workers described an attenuation-slope mapping method for plaque detection [48]. High attenuation slope was seen in areas of plaque with various forms such as lipid pools or calcification. In [49], spectral analysis of RF ultrasound data was applied by Spencer and co-workers to characterize loose, moderately and dense fibrotic tissue and calcified plaque. When measurements of acoustic parameters are performed locally with a small range-gated window, parametric imaging of the arterial wall can be generated in a similar way as gray scale

imaging. Bridal et al. demonstrated that the local assessment of a combined parameter of integrated backscatter and attenuation yielded a parametric image that provided a system-independent, quantitative view of arterial tissues [50].

### *Intravascular elastography*

“Sonoelasticity imaging” [51,52] or elastography [53,54] is alternative approaches for tissue characterization by means of measuring the mechanical properties of tissues such as elasticity and mechanical impedance. The principle of elastography involves local displacement estimation by cross-correlating the RF data before and after deformation [55]. Based on this principle, Ryan et al. analyzed the accumulated displacement of a vessel specimen under different pressure ranges [56]. Using the inflation of a balloon as an external deformation force, Shapo and co-workers proposed a method to obtain displacement and strain imaging of coronary arteries [57]. The potentials of intravascular elastography were demonstrated by Céspedes et al. in a phantom study [58]. Possible image artifacts concerning elastography were investigated by De Korte et al. [59].

In summary, RF signal processing has been widely applied in measurements of acoustic properties and tissue characterization based on quantitation of acoustic or mechanical properties of the arterial wall. Although most of these developments is still in the stage of in vitro validation, combination of conventional video image data with high resolution parametric imaging can potentially improve the accuracy and reliability of an automated contour detection approach.

## **7 OUTLINE OF THIS THESIS**

This thesis concerns aspects of quantitative analysis, signal and image processing in high frequency intravascular ultrasound. The work presented in this thesis consists of 1) study in the accuracy and reproducibility of quantitative IVUS for measurements of 2D and 3D vessel dimensions (*Chapter 2&5*); 2) image processing for automated contour detection and 3D reconstruction (*Chapter 3&4*); 3) image enhancement using either video data or RF signals (*Chapter 6&7*); 4) development of an RF processing method for extraction of local blood velocities and volumetric flow (*Chapter 8&9*).

Before it can be applied in clinical routine, a new imaging modality needs to be validated often by comparing to known technologies. *Chapter 2* presents a validation study in which the accuracy and reproducibility of quantitative IVUS measurements were investigated. Ultrasound measurements obtained in vitro and in vivo were compared with data from histology and x-ray angiography. Intra- and interobserver

variability in lumen area measurements, lesion area and percent area obstruction were assessed in clinical data.

Computerized detection of the lumen and plaque boundaries is the key step to automate the quantitative analysis procedure. In *Chapter 3* a semi-automatic method is described that allows frame-to-frame tracking of the lumen boundary for analysis of regional wall displacements. The performance of this method was evaluated by comparing computer-derived data with manual contour tracing. A higher beat-to-beat reproducibility was observed in measurements using the semi-automatic approach. Results of two clinical applications demonstrated the feasibility of this method in assessment of vascular distensibility and wall compliance.

In *Chapter 4* various techniques to obtain optimal reconstruction and display of the 3D intravascular ultrasound data are discussed. A semi-automatic approach for detection of the lumen and plaque contours on a slice sequence was developed to obtain volumetric measurement of a vessel segment. This approach optimizes the contour detection algorithm by combining information from two perpendicular longitudinal views. A preliminary validation study was performed in patient data obtained in peripheral arteries. In *Chapter 5* the accuracy and reproducibility of the quantitative 3D system was further evaluated in a phantom study as well as in intracoronary ultrasound data. A tubular phantom with segments of different luminal dimensions was examined with multiple catheter pull-backs. Subsequently intra- and interobserver variations in measurements of cross-sectional and volumetric lumen and plaque dimensions were investigated in vivo in diseased human coronary arteries. This study indicated that the proposed system can be used to perform highly reproducible area and volume measurements in 3D intracoronary ultrasound in vivo.

As indicated by several studies [35, 37,38], the backscatter from blood may have a level equal to or greater than the echo intensity of lesions and wall tissues due to the use of high ultrasonic frequency in IVUS imaging. *Chapter 6* and *Chapter 7* tackle the problem of echogenic blood using two approaches. In *Chapter 6* a video image averaging method is described that enables enhancement of the luminal boundary for off-line analysis. The utility of this method was tested by comparing the lumen area measurements on the temporal-averaged image with the data of the same cross-section obtained from the single-frame and saline-filled images. A lower degree of observer variations was found in the averaging method when compared to the measurements in still-frame images. This method, however, is only suitable for off-line application due to the inherent limitation of a video based approach.

In *Chapter 7* the time-varying characteristics of blood scattering were investigated in vivo by means of analysis of an RF sequence acquired at a fixed angle. Two RF processing techniques, temporal averaging and correlation, were tested for suppression

of the blood echo intensity. The RF correlation method has shown to be highly effective in distinguishing scattering echoes of moving blood from those of static tissues. A significant enhancement at the luminal interface was obtained when applying the correlation approach to a cross-sectional image data. The RF processing technique can in principle be used for real-time image enhancement and automated contour detection of the luminal boundary.

The unique spatial relationship between the blood flow and the ultrasound beam provides a new potential to quantify volumetric flow with IVUS imaging techniques. The feasibility of extracting blood velocity from the decorrelation of an RF sequence was investigated in *Chapter 8* and *Chapter 9*. The decorrelation properties of intravascular echo signals were studied through theoretical analysis and computer simulation in *Chapter 8*. A computer model based on the impulse response method was developed to describe the near-field of a 30 MHz circular transducer. The decorrelation due to the displacement of scatterers as well as other non-motion related decorrelation sources were discussed. *Chapter 9* presents a decorrelation-based method for measuring local blood velocity and quantifying volume flow from cross-sectional RF data. Serial in vitro measurements were performed with a flow phantom to test the principle of the proposed velocity estimate method. Measurements were also carried out in vivo in pig experiments to determine the usefulness of this method in clinical settings.

## 8 REFERENCES

1. Gussenhoven WJ, Essed CE, Lancée CT, Mastik F, Frietman P, van Egmond FC, Reiber J, Bosch H, van Urk H, Roelandt J, Bom N. Arterial wall characteristics determined by intravascular ultrasound imaging: an in vitro study. *J Am Coll Cardiol* 1989;14:947-952.
2. Yock PG, Linker DT. Intravascular ultrasound. Looking below the surface of vascular disease. *Circulation* 1990;81:1715-1718.
3. Nissen SE, Gurley JC, Grines CL, Booth DC, McClure R, Berk M, Fischer C, DeMaria AN. Intravascular ultrasound assessment of lumen size and wall morphology in normal subjects and patients with coronary disease. *Circulation* 1991;84:1087-1099.
4. Fitzgerald PJ, St Goar FG, Connolly AJ, Pinto FJ, Billingham ME, Popp RL, Yock PG. Intravascular ultrasound imaging of coronary arteries: is three layers the norm? *Circulation* 1992;86:154-158.
5. Ge J, Erbel R, Rupprecht HJ, Koch L, Kearney P, Gorge G, Haude M, Meyer J. Comparison of intravascular ultrasound and angiography in the assessment of myocardial bridging. *Circulation* 1994;89:1725-1732.
6. Mintz GS, Popma JJ, Pichard AD, Kent KM, Satler LE, Chuang YC, Ditrano CJ, Leon MB. Patterns of calcification in coronary artery disease: a statistical analysis of

- intravascular ultrasound and coronary angiography in 1155 lesions. *Circulation* 1995;91:1959-1965.
7. Yock PG, Fitzgerald PJ, Linker DT, Angelsen BAJ. Intravascular ultrasound guidance for catheter-based coronary interventions. *J Am Coll Cardiol* 1991;17:39B-45B.
  8. The SHK, Gussenhoven EJ, Zhong Y, Li W, van Egmond F, Pieterman H, van Urk H, Gerritsen GP, Borst C, Wilson RA, et al. Effect of balloon angioplasty on femoral artery evaluated with intravascular ultrasound imaging. *Circulation* 1992;86(2):483-493.
  9. Tenaglia AN, Buller CE, Kisslo KB, Stack RS, Davidson CJ. Mechanisms of balloon angioplasty and directional coronary atherectomy as assessed by intracoronary ultrasound. *J Am Coll Cardiol* 1992;20:685-691.
  10. Matar FA, Mintz GS, Farb A, Douek P, Pichard AD, Kent KM, Satler LF, Popma JJ, Keller MB, Pinnow E, Merritt AJ, Lindsay JR, Leon MB. The contribution of tissue removal to lumen improvement after directional coronary atherectomy. *Am J Cardiol* 1994;74:647-650.
  11. Miniz GS, Griffin J, Chuang YC, Pichard AD, Kent KM, Satler LF, Popma JJ, Leon MB. Reproducibility of the intravascular ultrasound assessment of stent implantation in saphenous vein grafts. *Am J Cardiol* 1995;75(17):1267-1270.
  12. von Birgelen C, Gil R, Ruygrok P, Prati F, Di Mario C, van der Giessen WJ, de Feyter PJ, Serruys PW. Optimized expansion of the Wallstent compared with the Palmaz-Schatz stent: online observations with two- and three-dimensional intracoronary ultrasound after angiographic guidance. *Am Heart J* 1996;131:1067-1075.
  13. Bom N, Hoff HT, Lancée CT, Gussenhoven WJ, Bosch JG. Early and recent intraluminal ultrasound devices. *Int J Cardiac Imag* 1989; 4: 79-88.
  14. Wells PNT. *Biomedical ultrasonics*: Academic Press 1977.
  15. Davis LS. A survey of edge detection techniques. *Computer Graphics and Image Processing* 1975; 4:248-270.
  16. Geiser EA, Oliver LH. Echocardiography: Image processing in two-dimensional echocardiographic images. *Automedica*, 1984;5:171-188.
  17. Skorton DJ, Collins SM, Carcia E, Geiser EA, Hillard W, Koppes W, Linker D, Schwartz G. Digital signal and image processing in echocardiography. *Am Heart J* 1985; 110(6): 1266-1283.
  18. Skorton DJ, McNary CA, Child JS, Newton FC, Shah PM. Digital image processing of two-dimensional echocardiograms: Identification of the endocardium. *Am J Cardiol* 1981;48:479-486.
  19. Collins SM, Skorton DJ, Geiser EA, Nichols JA, Conetta DA, Pandian NG, Kerber RE. Computer-assisted edge detection in two-dimensional echocardiography: comparison with anatomic data. *Am J Cardiol* 1984;53:1380-1387.

20. Klingler JW, Vaughan CL, Fraker TD, Andrews LT. Segmentation of echocardiographic images using mathematical morphology. *IEEE Trans Biomed Eng* 1988; MBE-35(11):925-934.
21. Han CY, Lin KN, Wee WG, Mintz RM, Porembka DT. Knowledge-based image analysis for automated boundary extraction of transesophageal echocardiographic left-ventricular images. *IEEE Trans Med Imaging* 1991;10(4):602-610.
22. Zhang LF, Geiser EA. An approach to optimal threshold selection on a sequence of two-dimensional echocardiographic images, *IEEE Trans. Biomed. Eng.*, 1982; BME-29(8):577-581.
23. Zhang LF, Geiser EA. An effective algorithm for extracting serial endocardial borders from 2-Dimensional Echocardiograms. *IEEE Trans Biomed Eng* 1984; MBE-31(6):441-447.
24. Buda AJ, Delp EJ, Meyer CR, Jenkins JM, Smith DN, Bookstein FL, Pitt B. Automatic computer processing of digital 2-dimensional echocardiograms. *Am J Cardiol* 1983;52:384-389.
25. Ezekiel A, Garcia E, Areeda J, Corday S. Automatic and intelligent left ventricular contour detection from two-dimensional echocardiograms. In: *Computers in Cardiology 1985*. IEEE Computer Society Press, 1985: 261-264.
26. Ezekiel A, Areeda J, Corday S. Intelligent left ventricular contour detection results from two-dimensional echocardiograms. In: *Computers in Cardiology 1987*. IEEE Computer Society Press, 1987: 603-606.
27. Adam D, Hareuveni O, Sideman S. Semiautomatic border tracking of cine echocardiogram ventricular images. *IEEE Trans Med Imaging* 1987;6(3):266-271.
28. Chu CH, Delp EJ, Buda AJ. Detecting left ventricular endocardial boundaries by digital two-dimensional echocardiography. *IEEE Trans Med Imaging* 1988;7(2):81-90.
29. Feng J, Lin WC, Chen CT. Epicardial boundary detection using fuzzy reasoning. *IEEE Trans Med Imaging* 1991;10(2):187-199.
30. Gerbrands JJ. Segmentation of noisy images. Ph.D. Thesis, Delft University of Technology, 1988.
31. Unser M, Pelle G, Brun P, Eden M. Automated extraction of serial myocardial borders from M-mode echocardiograms. *IEEE Trans Med Imaging* 1989;8(1):96-103.
32. Friedland N, Adam D. Automatic ventricular cavity boundary detection from sequential ultrasound images using simulated annealing. *IEEE Trans Med Imaging* 1989;8(4):344-353.
33. Bosch JG, Reiber JHC, Burken G van, Gerbrands JJ, Gussenhoven WJ, Bom N, Roelandt JRTC. Automated endocardial contour detection in short-axis 2-D echocardiograms: methodology and assessment of variability. In: *Computers in Cardiology 1988*. IEEE Computer Society Press, 1988: 137-140.

34. Bosch JG, Reiber JHC, Burken G van, Gerbrands JJ, Kostov A, van de Goor AJ, van Daele MERM, Roelandt JRTC. Developments towards real-time frame-to-frame automatic contour detection on echocardiograms. In: Computers in Cardiology 1990. IEEE Computer Society Press, 1990: 435-438.
35. Lockwood GR, Ryan LK, Hunt JW, Foster FS. Measurement of the ultrasonic properties of vascular tissues and blood from 35-65 MHz. *Ultrasound Med. Biol.* 1991;17: 653-666.
36. De Kroon MGM, Van der Wal LF, Gussenhoven WJ, Bom N. Angle dependent backscatter from the arterial wall. *Ultrasound Med Bio* 1991;17:121-126.
37. De Kroon MGM. Acoustic backscatter in arteries: Measurements and modelling of arterial wall and blood, Ph.D. Thesis, Erasmus University Rotterdam, 1993.
38. Foster FS, Obara H, Bloomfield T, Ryan LK, Lockwood GR. Ultrasound backscatter from blood in the 30 to 70 MHz frequency range. in *Proc IEEE Ultrasonics Symposium* 1994: 1599-1602.
39. Miller JG, Pérez JE, Sobel BE. Ultrasonic characterization of myocardium. *Prog Cardiovasc Dis* 1985;(28):85-110.
40. Rijsterborgh H, Mastik F, Lanceé CT, van der Steen AFW, Sassen LMA, Verdouw PD, Roelandt J, Bom N. Ultrasonic myocardial integrated backscatter and myocardial wall thickness in animal experiments. *Ultrasound in Med & Biol* 1990(16):29-36.
41. van der Steen AFW, Rijsterborgh H, Mastik F, Lanceé CT, van Hoorn WM, Bom N. Influence of attenuation on measurements of ultrasonic myocardial integrated backscatter during cardiac cycle (an in vitro study). *Ultrasound in Med & Biol* 1991;17(9):869-877
42. Lizzi FL, King DL, Rorke MC. Comparison of theoretical scattering results and ultrasonic data from clinical liver examinations. *Ultrasound in Med & Biol* 1988(14):377-385.
43. Oosterveld BJ, Thijssen JM, Hartman PC, Rosenbusch GJE. Detection of diffuse liver disease by quantitative echography: dependence on a prior choice of parameters. *Ultrasound in Med & Biol* 1993(19):21-26.
44. van der Steen AFW, Thijssen JM, Ebben GPJ, van der Laak JAWM, de Wilde PCM. Correlation of histology and acoustical parameters of liver tissue on a microscopic scale. *Ultrasound in Med & Biol* 1994; 20(2): 177-186.
45. Romijn RL, Thijssen JM, Oosterveld BJ, Verbeek AM. Ultrasonic differentiation of intraocular melanomas: parameters and estimation methods. *Ultrasonic Imag* 1991;(13)27-55.
46. de Korte CL, van der Steen AFW, Thijssen JM. Acoustic velocity and attenuation of eye tissues at 20 MHz. *Ultrasound in Med & Biol* 1994;20(5): 471-480.



47. Wickline SA, Miller JG, Rechia D, Sharkey AM, Bridal L, Christy D. Beyond intravascular imaging: Quantitative ultrasonic tissue characterization of vascular pathology. *IEEE Ultrasonics Symp* 1994;3:1589-1597.
48. Wilson LS, Neale ML, Talham HE, Appleberg M. Preliminary results from attenuation-slope mapping of plaque using intravascular ultrasound. *Ultrasound Med. Biol.* 1994;20: 529-542.
49. Spencer T, Ramo MP, Salter DM, Anderson T, Kearney PP, Sutherland GR, Fox KAA, McDicken WN. Characterisation of atherosclerotic plaque by spectral analysis of intravascular ultrasound: an in-vitro methodology. *Ultrasound Med. Biol.* (in press).
50. Bridal SL, Fornes P, Bruneval P, Berger G. Parametric (integrated backscatter and attenuation) images constructed using backscattered radio frequency signals (25 to 56 MHz) from human aortae in vitro. *Ultrasound Med. Biol.* (in press).
51. Ophir J, Céspedes I, Ponnekanti H, Yazdi Y, Li X. Elastography: A method for imaging the elasticity in biological tissues. *Ultrasonic Imaging* 1991;13(1):111-134.
52. Céspedes I, Ophir J, Ponnekanti H, Maklad N. Elastography: elasticity imaging using ultrasound with application to muscle and breast in vivo. *Ultrasonic Imaging* 1993;15(2):73-88.
53. Ophir J, Céspedes I, Garra B, Ponnekanti H, Huang Y, Maklad N. Elastography: ultrasonic imaging of tissue strain and elastic modulus in vivo. *European J Ultrasound* 1996;(3):49-70.
54. Lerner RM, Huang SR, Parker KJ. "Sonoelasticity" images derived from ultrasound signals in mechanically vibrated tissue. *Ultrasound Med & Biol* 1990;16(3):231-239.
55. Parker KJ, Huang SR, Musulin RA, Lerner RM. Tissue response to mechanical vibrations for "sonelasticity imaging". *Ultrasound Med & Biol* 1990;16(3):241-246.
56. Ryan LK, Lockwood GR, Starkoski BG, Holdsworth DW, Rickey DW, Dranova M, Fenster A, Foster FS. A high frequency intravascular ultrasound imaging system for investigation of vessel wall properties. in *Proc IEEE Ultrason Symp* 1992:1101-1105
57. Shapo BM, Crowe JR, Skovoroda AR, Eberle MJ, Cohn NA, O'Donnell M. Displacement and strain imaging of coronary arteries with intraluminal ultrasound. *IEEE Trans Ultrason Ferroelec Freq Contr* 1996;43:84-102.
58. Céspedes EI, de Korte CL, van der Steen AFW, Lancée CT. Intravascular elastography: principles and potentials. *Seminars in Interventional Cardiology* 1996 (in press).
59. de Korte CL, Céspedes EI, van der Steen AFW, Lancée CT. Image artifacts in intravascular elastography. in *proc IEEE EMBS* 1996: p 685.



## CHAPTER 2

---

# VALIDATION OF QUANTITATIVE ANALYSIS OF INTRAVASCULAR ULTRASOUND IMAGES

W. Li, E. J. Gussenhoven, Y. Zhong, S. H. K. The, C. Di Mario,  
S. Madretsma, F. v. Egmond, P. d. Feyter, H. Pieterman,  
H. v. Urk, H. Rijsterborgh, N. Bom

Published in: International Journal of Cardiac Imaging 1991(6): 247-253.



## **ABSTRACT**

This study investigated the accuracy and reproducibility of a computer-aided method for quantification of intravascular ultrasound. The computer analysis system was developed on an IBM compatible PC/AT equipped with a framegrabber. The quantitative assessment of lumen area, lesion area and percent area obstruction was performed by tracing the boundaries of the free lumen and original lumen.

Accuracy of the analysis system was tested in a phantom study. Echographic measurements of lumen and lesion area derived from 16 arterial specimens were compared with data obtained by histology. The differences in lesion area measurements between histology and ultrasound were minimal (mean  $\pm$  SD:  $-0.27 \pm 1.79 \text{ mm}^2$ ,  $p > 0.05$ ). Lumen area measurements from histology were significantly smaller than those with ultrasound due to mechanical deformation of histologic specimens ( $-5.38 \pm 5.09 \text{ mm}^2$ ,  $p < 0.05$ ). For comparison with angiography, 18 ultrasound cross-sections were obtained in vivo from 8 human peripheral arteries. The arterial lumen area measured with ultrasound revealed a  $5.9\% \pm 2.4\%$  change between the systolic and diastolic phases of one cardiac cycle. Luminal areas obtained by angiography were similar to those by ultrasound ( $-0.52 \pm 5.15 \text{ mm}^2$ ,  $p > 0.05$ ). Finally, intra- and interobserver variability of quantitative intravascular ultrasound was evaluated in measurements of 100 in vivo ultrasound images. The results showed that variations in lumen area measurements were low (5%) whereas variations in lesion area and percent area obstruction were relatively high (13% and 10%, respectively).

Results of this study indicate that quantitation of intravascular ultrasound with the computerized method provides accurate and reproducible measurements of lumen and lesion area, and thus can be used for clinical investigation in assessment of vascular stenosis and evaluation of therapeutic intervention.

## **1 INTRODUCTION**

Intravascular ultrasound imaging is a new technique providing real-time, cross-sectional, high resolution images of the arterial wall. The capability to obtain absolute measurements of arterial cross-sectional dimensions, such as lumen area and lesion thickness, makes this tomographic technique most suitable for quantitative assessment of the extent and severity of arterial atherosclerotic diseases [1-2]. Several studies have demonstrated the feasibility of intravascular ultrasound in qualitative as well as quantitative assessment of vascular stenosis, and its potential clinical application to evaluate intravascular intervention [3-5]. However, extensive study is still necessary to determine the adequacy of quantitative analysis regarding observer variations in measurements and possible error sources in the imaging mechanism. A computer

analysis system has been developed in our laboratory to provide quantitative analysis of intravascular ultrasound images. The purpose of the present study was to validate the accuracy and reproducibility of the computerized method for quantification of intravascular ultrasound through in vitro and in vivo study of both normal and diseased arteries.

Four steps were followed: 1) accuracy of the analysis system was evaluated in a phantom study; 2) lumen and lesion area measurements from in vitro echograms of arterial specimens were compared with those from histology; 3) lumen area obtained from in vivo study of normal peripheral arteries were compared with data from standard angiography; area measurements were performed in systole and diastole in each arterial cross-section to evaluate the possible measurement discrepancy caused by cardiac contraction; 4) intra- and interobserver variability in measurements of lumen area, lesion area and percent area obstruction was studied using images from current clinical trials of intravascular ultrasound in diseased peripheral arteries.

## 2 METHOD

### 2.1 Intravascular ultrasound system

The intravascular ultrasound imaging system (Du-MED, Rotterdam, The Netherlands) comprises a 32 MHz single-element transducer mounted on the tip of a 5F catheter and rotated by a flexible drive-shaft. Cross-sectional images with 512 x 512 pixels and 256 grey levels can be scanned at a maximum speed of 16 frames per second. Axial resolution of the system is <math><0.1\text{ mm}</math>. The maximum scan depth is 9 mm. Acquired physiological signals such as ECG and blood pressure can be displayed on the screen simultaneously.

### 2.2 Computer methodology

The computer analysis system has been described previously [6]. Briefly, the analysis system was developed on an IBM compatible PC/AT equipped with a DT 2851 framegrabber and a PC mouse for manual contour tracing (Fig. 1). The analysis procedure consists of three main steps: image acquisition, contour tracing and parameter calculation. During image acquisition, video signals from a standard

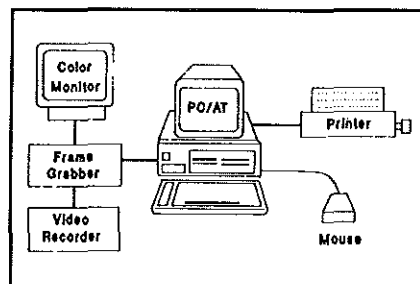


*Fig. 1. Configuration of the computer analysis system*

VHS videotape are converted into 512 x 512 x 8 bits digital image data with the framegrabber and stored on the hard disk of the PC. Manual tracings of the circumferential outline are processed by the computer to produce a smoothed, connected and closed contour. Parameter calculations are automatically performed after the contour has been completed or modified.

### 2.3 Boundary tracing

The contour of the free lumen was obtained by tracking the bright echoes of the internal elastic lamina. In the presence of a lesion, the inner boundary of the lesion was traced. For in vivo images containing strong backscatter echoes from flowing blood, the real-time images were reviewed several times on a separate videomonitor to identify blood backscatter echoes, which appeared as spontaneous contrast within the lumen.

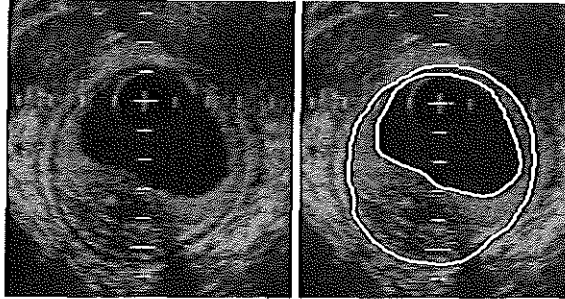


*Fig. 2. Intravascular ultrasound of the superficial femoral artery (left) and the traced contours of the free and original lumen (right). The region enclosed by the two contours is the lesion.*

To obtain the measurement of lesion area, the contour of the original lumen was derived from the typical three-layered appearance of a muscular vessel [7,8]. The original luminal contour overlapped the free luminal contour in the region with a normal arterial wall. For the region containing a lesion, the interface between the lesion and the underlying echolucent media was traced to estimate the boundary of the original lumen.

With the traced contours of the free and original lumen, the lesion area is simply defined as the region enclosed by these two contours. An example of tracing the free and original luminal contours is given in Fig. 2.

### 2.4 Parameter calculation

Both free and original luminal areas were computed by counting the pixels enclosed by these contours. The lesion area was derived by subtracting the area of the free lumen from that of the original lumen. A mean diameter ( $d = 2r$ ) of the free lumen was defined using a circular model ( $A = \pi r^2$ ). The percent area obstruction was derived by the following equation:

$$\text{Percent area obstruction} = \frac{(\text{original lumen area} - \text{free lumen area}) \times 100}{\text{original lumen area}}$$

Calibration was performed by measuring the scale markers on the images both vertically and horizontally and converting the pixels into square millimeters.

### **2.5 Phantom study**

To test the accuracy of the analysis system, three phantoms containing water-filled cylinders with diameters of 4, 8 and 16 mm were used. The catheter was positioned coaxially at the center of the cylinders. Each of the phantoms was imaged five times by the ultrasound system and measured using the computer analysis system described above.

### **2.6 In vitro measurements compared with histology**

Specimens obtained from 16 peripheral arteries were embedded in 1.2% agar-agar solution and filled with purified water. The catheter was placed at the center of the specimen and a number of cross-sections was obtained from proximal to distal at 1 mm intervals. The echogram showing the largest lesion was selected for comparative purposes. Lumen and lesion areas were measured and compared with the corresponding histologic data.

The histologic sections were analyzed using a commercially available system (IBAS, Kontron, USA). Lumen and lesion areas were calculated from manual tracings of the edges of the lumen and the internal elastic lamina.

### **2.7 In vivo studies compared with angiography**

For comparison with angiography, 18 in vivo echo images were obtained from 8 normal peripheral arteries. For each of 18 arterial cross-sections, echo images of early systole and end-diastole were analyzed separately. The percentage change in the lumen area was calculated from these two measurements. Because the angiographic data were obtained from an arbitrary phase of the cardiac cycle, the mean lumen area of the two ultrasonic measurements was used for comparison with angiography.

Cinefilms acquired at the same arterial position were measured using the Coronary Angiography Analysis System [9]. The angiographic measurement of the lumen area was estimated with the measured diameter based on a circular model.



## 2.8 Intra- and interobserver variability study

Intra- and interobserver variability was studied in measurements of 100 in vivo intravascular ultrasound images obtained from 22 patients who underwent balloon angioplasty of the superficial femoral artery.

The study was performed by two independent observers. Both observers were instructed to review the real-time echo images during the contour tracing. One of the observers repeated the measurements one month later. The observer variations were analyzed for quantitative assessments of lumen area, lesion area and percent area obstruction. Contraction of a vessel may induce measurement differences during a cardiac cycle; this effect was assessed in each patient by measuring the luminal area frame-by-frame throughout a complete cardiac cycle. A percent luminal change was defined as the ratio of the area difference between the early-systole and end-diastole and the mean lumen area averaged over the entire cycle.

## 2.9 Statistical analysis

Agreement between the two techniques was evaluated with the mean values and standard deviations of the paired differences [10]. Linear regression with the method of least squares was used to calculate the slopes and intercept parameters. Observer differences were assessed with the mean values and standard deviations of the paired differences. The degree of observer variability was estimated by standard deviations of the paired differences. The significance of the differences for data was determined by a paired t-test. A probability value of  $<0.05$  was considered significant.

# 3 RESULTS

## 3.1 Phantom study

Accuracy of the analysis system for the phantom measurements was very high (mean diameter  $\pm$  SD:  $3.84 \pm 0.01$  {4 mm},  $7.97 \pm 0.04$  {8 mm}, and  $16.24 \pm 0.06$  {16 mm}, respectively). The data showed excellent agreement with the dimensions of the phantoms.

## 3.2 Comparison with histology

The regression equations for data between histology and ultrasound were  $y = 1.22 \times [\textit{histology}] - 0.95$  for lumen area and  $y = 0.94 \times [\textit{histology}] + 0.85$  for lesion area (Fig. 3). No significant differences in lesion area measurements were found between the two methods ( $-0.27 \pm 1.79 \text{ mm}^2$ ,  $p > 0.05$ ). However, the mean lumen area obtained

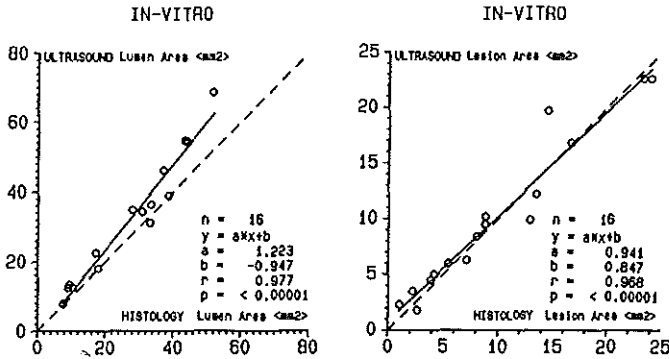


Fig. 3. Comparison of histology and ultrasound data for lumen area (left) and lesion area (right).

by histology was 17% smaller than with ultrasound ( $-5.38 \pm 5.09 \text{ mm}^2$ ,  $p < 0.05$ , mean of the measurements:  $31.1 \text{ mm}^2$ ).

### 3.3 Comparison with angiography

The percent change of the systolic and diastolic luminal areas is shown in Fig. 4. The mean value measured from 8 patients revealed a  $5.9\% \pm 2.4\%$  difference in the luminal area between systole and diastole of a cardiac cycle.

The regression result of lumen area measurements from angiography and ultrasound was close to the line of identity ( $y = 0.95x$  [angiography] + 2.07) (Fig. 5). The paired differences between ultrasonic and angiographic lumen area measurements were minimal ( $-0.52 \pm 5.15 \text{ mm}^2$ ,  $p > 0.05$ ).

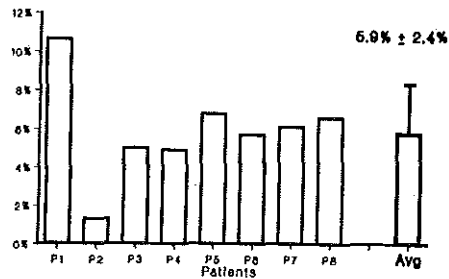


Fig. 4. Percent differences of the lumen area between early-systole and end-diastole in 8 patients.

### 3.4 Intra- and interobserver variability

Data of observer variability studies in measurements of lumen area, lesion area and percent area obstruction are shown in Figs 6-8, with scatter plots of the differences versus the measured mean values. For all measurements, no significant observer bias (a non-zero mean of the paired differences) was present. In both intra- and interobserver differences, observer variations (standard deviations of the paired differences) in lumen

area measurements were relatively smaller than those of lesion area measurements (intraobserver:  $0.6 \text{ mm}^2$  for lumen area vs  $1.1 \text{ mm}^2$  for lesion area, interobserver:  $1.2 \text{ mm}^2$  for lumen area vs  $1.9 \text{ mm}^2$  for lesion area). Intra- and interobserver variations in measurements of percent area obstruction were 2.6% and 5.6%, respectively.

#### 4 DISCUSSION

In both in vitro and in vivo studies, quantitative assessment of intravascular ultrasound agreed well with histology and angiography, except for the 17% underestimate in histologic lumen area measurements. The underestimate by histology can probably be attributed to the fixation and tissue processing during histologic preparation of the specimens. After this procedure, the shape of the vessel lumen may alter and tissue shrinkage may occur, resulting in a slight decrease in histologic measurements.

Results of the in vivo measurement indicate the luminal area may differ during different phases of a cardiac cycle. We observed approximately 6% differences between the systolic and diastolic lumen areas in peripheral arteries. This might not be

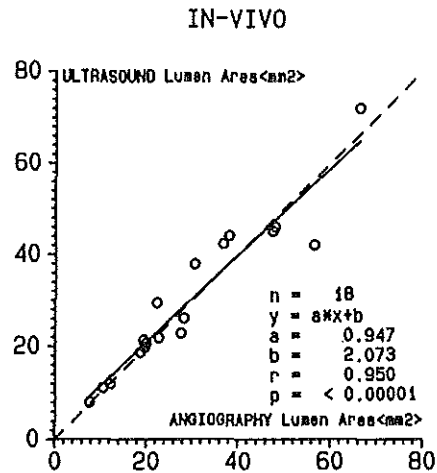


Fig. 5. Comparison of angiography and ultrasound data for lumen area.

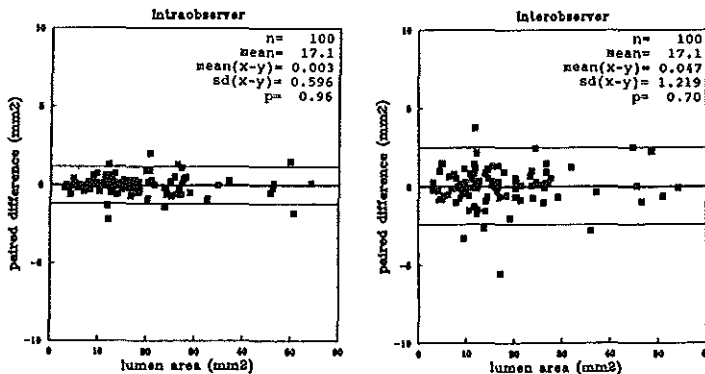


Fig. 6. Intra- and interobserver variability in lumen area measurements. The 95% confidence interval is indicated by the upper (mean + 2SD) and lower (mean - 2SD) vertical lines.

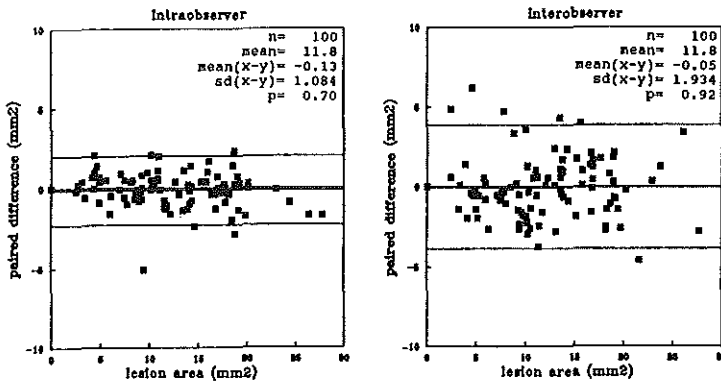


Fig. 7 Intra- and interobserver variability in lesion area measurements. The 95% confidence interval is indicated by the upper (mean + 2SD) and lower (mean - 2SD) vertical lines.

significant for individual measurements, but should be taken into account for data comparison, for instance, before and after balloon angioplasty. Particularly, it could be more important for intracoronary application as the pulsatile change in the coronary lumen may have a much larger value of 18% [11]. Thus, comparison of the two independent measurements will require synchronization of ECG or blood pressure signals. In the present study, the cardiac phase information was not registered in angiographic measurements. To minimize a possible discrepancy caused by comparing data of different cardiac phases, the systolic and diastolic lumen areas in the ultrasound measurement were averaged before comparison with angiography. On the other hand, it should be noted that intravascular ultrasound is a tomographic technique and angiography is a silhouette technique. Therefore, identical results may only be expected in vessels with circular geometry. For healthy vessels with often almost circular cross-sections, no significant differences were found in our comparison study with angiography.

The images used in the observer variability studies were of clinical quality, selected by another clinical group for assessment of the effect of vascular intervention with intravascular ultrasound. The aim was to evaluate observer variability under conditions similar to practical applications. For a rough guide of observer variability from our results, one may estimate observer variations in percent defined by the ratio between standard deviations of the paired differences and their mean measurements. Using the means of intra- and interobserver data, the percent observer variations for quantitative data of lumen area, lesion area and percent area obstruction were 5%, 13% and 10%, respectively. The repeatability in the quantitative assessment of lumen area was very good. The influence of blood backscatter echoes on determination of the luminal

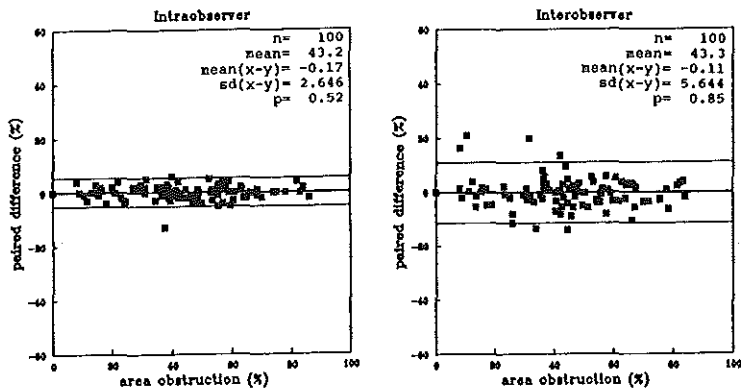


Fig. 8 Intra- and interobserver variability in percent area obstruction measurements. The 95% confidence interval is indicated by the upper (mean + 2SD) and lower (mean - 2SD) vertical lines.

contour can be minimized by reviewing the real-time images. The higher degree of observer variations in lesion area measurements suggests that it is relatively more difficult to determine the boundary of the media than the arterial lumen. This is intimately related to the presence of an advanced atherosclerotic lesion with partial dropout of far-field echoes, and complex wall structure such as rupture or dissection of the lesion following intervention.

Other factors may also affect the accuracy of quantitative results, including minor differences in sound velocity between saline and blood [12], image distortion caused by the mechanical system [13] and overestimation of the cross-sectional dimensions due to the off-axis catheter position [14]. Of these three factors, the off-axis catheter position seems to be the most serious problem. Although the angle between the catheter and the arterial wall was difficult to determine for *in vivo* measurements, our experience in peripheral artery studies showed that, in most cases, the catheter was aligned with the normal or minimal diseased part of the wall [15]. With straighter peripheral arteries one can expect that alignment allows an approximately co-axis catheter position.

## 5 CONCLUSION

In the phantom study and the comparison with histology and angiography, we demonstrated the feasibility to obtain accurate quantitative assessment of lumen, lesion area and percent area obstruction with intravascular ultrasound. Observer variability in measurements proved to be satisfactorily low in terms of analyzing images from a new technique. Using our method, quantitative analysis of intravascular ultrasound can be

used for clinical applications such as assessment of vascular stenosis and evaluation of therapeutic intervention.

## 6 REFERENCES

1. Bom N, Hoff HT, Lancée CT, Gussenhoven WJ, Bosch JG. Early and recent intraluminal ultrasound devices. *Int J Cardiac Imag* 1989; 4: 79-88.
2. Roelandt J, Serruys PW. Intraluminal real-time ultrasonic imaging: Clinical perspectives. *Int J Cardiac Imag* 1989; 4: 89-97.
3. Pandian NG, Weintraub A, Kreis A, Schwartz SL, Konstam MA, Salem DN. Intracardiac, intravascular, two dimensional high frequency ultrasound imaging of pulmonary artery and its branches in humans and animals. *Circulation* 1990; 81: 2007-12.
4. Neville RF, Bartorelli AL, Sidawy AN, Almagor Y, Potkin B, Leon MB. An in-vivo feasibility study of intravascular ultrasound imaging. *Am J Surg* 1989; 158: 142-45.
5. Tobis JM, Mallery JA, Gessert J, Griffith J, Mahon D, Bessen M, Moriuchi M, McRae M, Henry WL. Intravascular ultrasound cross-sectional arterial imaging before and after balloon angioplasty in-vitro. *Circulation* 1989; 80: 873-82.
6. Li W, Gussenhoven WJ, Bosch JG, Mastik F, Reiber JHC, Bom N. A computer-aided analysis system for the quantitative assessment of intravascular ultrasound images. In: *Computers in Cardiology* 1991. Los Alamitos: IEEE Computer Society Press, 1991: 333-336.
7. Gussenhoven EJ, Essed CE, Lancée CT, Mastik F, Frietman P, Egmond F van, Reiber J, Bosch H, Urk Hv, Roelandt J, Bom N. Arterial wall characteristics determined by intravascular ultrasound imaging: An in-vitro study. *J Am Coll Cardiol* 1989; 14: 947-52.
8. Potkin BN, Bartorelli AL, Gessert JM, Neville RF, Almagor Y, Roberts WC, Leon MB. Coronary artery imaging with intravascular ultrasound. *Circulation* 1990; 81: 1575-85.
9. Reiber JHC, Serruys PW, Kooijman CJ. Assessment of short-, medium-, and long-term variations in arterial dimensions from computer-assisted quantitation of coronary cineangiograms. *Circulation* 1985; 71: 280-88.
10. Bland JM, Altman DG. Statistical methods for assessing agreement between two methods of clinical measurement. *Lancet* 1986; 8:307-10.
11. Nissen SE, Gurely, JC. Application of intravascular ultrasound for detection and quantitation of coronary atherosclerosis. *Int J Cardiac Imag* 1991;6:165-77.
12. Moriuchi M, Tobis JM, Mahon D, Gessert J, Griffith J, McRae M, Moussabeck O, Henry WL. The reproducibility of intravascular ultrasound imaging in-vitro. *J Am Soc Echo* 1990; 3: 444-50.
13. Hoff HT, Korbijn A, Smit TH, Klinkhamer JFF, Bom N. Imaging artifacts in mechanically driven ultrasound catheters. *Int J Cardiac Imag* 1989; 4: 195-99.

14. Nishimura RC, Edwards WD, Warnes CA, Reeder GS, Holmes DR, Tajik AJ, Yock PG. Intravascular ultrasound imaging: In-vitro validation and pathologic correlation. *J Am Coll Cardiol* 1990; 16: 145-54.
15. van Urk H, Gussenhoven EJ, Gerritsen GP, The SHK, van Egmond F, Lancée CT, Bom N. Assessment of arterial disease reconstructions by intravascular ultrasound. *Int J Cardiac Imag* 1991; 6: 157-164.





**SEMI-AUTOMATIC FRAME-TO-FRAME TRACKING  
OF THE LUMINAL BORDER FROM  
INTRAVASCULAR ULTRASOUND:**

**Technical Development and Clinical Applications**

W. Li<sup>\*</sup>, S.H.K. The<sup>\*\*</sup>, R.A. Wilson<sup>\*\*\*</sup>,  
J. G. Bosch, E.J. Gussenhoven, C. Di Mario,  
J.H.C. Reiber, N. Bom, P.D. Verdouw, J.R.T.C. Roelandt.

Based on the publications:

\* Semiautomatic frame-to-frame tracking of the luminal border from intravascular ultrasound. In: *Computers in Cardiology 1992. IEEE Comp Soc Press 1992:353-356.*

\*\* Assessment of regional vascular distensibility in diseased iliofemoral arteries by intravascular ultrasound. *Ultrasound Med Biol 1995;21:17-24.*

\*\*\* In vivo measurement of regional large artery compliance by intravascular ultrasound under pentobarbital anesthesia. *Angiology 1995;46:481-488.*

\*, \*\*, \*\*\* indicate the first authors of the published papers.



**ABSTRACT**

A template-matching method is described that allows measurement of the frame-to-frame changes in luminal cross-sectional area from intravascular ultrasound images by analysis of the regional wall displacement. Template matching is performed by cross-correlating the template data derived from the first frame with image data of the remaining frames. Optimal matching is determined using the minimum-cost algorithm. Comparison of the results from the template-matching method with those from manual tracing showed that the difference in area change was small (mean  $\pm$  SD:  $0.013 \pm 0.59$  mm<sup>2</sup>). The beat-to-beat variations evaluated with data from our method were smaller than obtained with manual tracing (computer: 1.0% vs manual: 2.7%). The proposed method has been applied in two studies: 1) in vivo measurement of regional large artery compliance in pigs; and 2) assessment of vascular distensibility in human diseased iliofemoral arteries. Results of both studies indicate that the template-matching method is suitable for wall compliance studies using intravascular ultrasound.

**1 INTRODUCTION**

Catheter-based intravascular ultrasound (IVUS) is a new technique to obtain real-time, cross-sectional and high-resolution images of the arterial wall. The real-time echogram provides information on the dynamic contraction of the arterial wall during a cardiac cycle. One potential clinical application is to study arterial wall compliance with quantitative IVUS. By measuring changes in the cross-sectional dimensions simultaneously with blood pressure, arterial wall compliance can be analyzed from their relationship [1-5]. In this chapter, a template-matching method is described that estimates the luminal border by analyzing the displacement of the wall segment. Results of applying the method in animal and patient studies are presented.

**Boundary tracking:** Frame-by-frame manual tracing of the luminal boundary is a straightforward method to measure changes in lumen area. However, manual procedures are often time-consuming and may suffer from considerable observer variability in deriving the small wall motion. On the other hand, direct application of an automatic contour detection technique is hampered by strong interference from the backscatter echoes of blood [6,7]. To overcome these problems, a semi-automatic tracing method has been developed from the minimum-cost algorithm [8,9]. The proposed method was tested by comparing the computer data with those obtained by manual tracings. Beat-to-beat variations were determined for both the computer tracking and manual tracing methods.

**Animal Study:** The presence of smooth muscle fibers on the wall of large arteries suggests that arterial compliance might change in response to vasoactive substances

[10-14]. The purpose of the animal study is to determine the basal level of vasomotor tone in these arteries in a commonly used animal model and to learn whether the compliance of large conductance arteries is altered in vivo by vasoactive agents.

Patient Study: Arterial distensibility is reported to be reduced in patients with atherosclerosis, hypertension and with increasing age [15-17]. The aims of the retrospective patient study are to investigate the influence of the percentage area stenosis and the effect of balloon angioplasty on the distensibility of iliac and superficial femoral arteries.

## 2 METHOD

### 2.1 Data acquisition

The IVUS imaging system (Du-MED, Rotterdam, The Netherlands) is a mechanically driven, single element system operating at 30 MHz. The axial resolution of the system is 75  $\mu\text{m}$  and the lateral resolution is no less than 225  $\mu\text{m}$  at a depth of 1 mm. The ultrasonic scan (16 frames per second) is converted into the video format via a video memory buffer and recorded with a standard VHS system. The analysis system was implemented on an IBM compatible PC/AT. The images recorded on the videotapes were digitized by a DT 2851 framegrabber and stored in 512 x 512 x 8 bits digital format on the hard disk. Simultaneously displayed blood pressure or ECG signal was used to select a complete set of frames throughout one cardiac cycle.

### 2.2 Tracking algorithm

#### *Two-dimensional template extraction*

The templates are extracted from a reference image obtained by averaging several frames in the diastolic period of a cardiac cycle. The first advantage of this temporal smoothing technique is that it may reduce image noise in the data for generating the templates. Second, the backscatter echoes of flowing blood can be recognized as natural contrast in real-time images, but are difficult to identify on a still frame. The averaging procedure takes advantage of relative randomness of the blood echoes and small wall motion in the diastolic frames. Averaging a number of consecutive frames from this period tends to smooth the blood echoes while having only minimal blurring effect on the arterial wall. Consequently, this processing improves visibility of the interface between blood and the wall and allows easier tracing of the luminal boundary. An example demonstrating this improvement is shown in Fig. 1.

To specify the position of the wall, the luminal boundary is manually traced on the reference image using a mouse. The image is transformed into polar coordinates with

the centerpoint defined by the center of gravity of the luminal contour. The arterial wall is then divided into 32 segments through the resampling lines. Each of the segments is characterized by a two-dimensional data profile  $\{X_i(l,k)\}$ ,  $i = 1, \dots, 32$ ,  $l = 1, \dots, L$  and  $k = 1, \dots, K$  in a window positioned by the user's defined contour points.  $L$  and  $K$  define the size of the template in the radial and angular directions, respectively. This procedure generates 32 two-dimensional templates that overlap each other by 50%.

### *Matching procedure*

The matching procedure is based on the cross-correlation between the reference template and the test data. Since we are interested in only the radial displacement of the arterial wall, the similarity test is performed by shifting the template with one radial unit each time over a search region. The value of the cross-correlation indicates how well the template fits the data at this position. Hence, a simple strategy to determine the best fit is finding the maximum value over the search region for each segment. However, this method takes decisions based on information from only one segment and could result in mismatches due to disturbances caused by changes in the backscatter pattern or partial dropouts of the wall. A more robust method is to determine an optimal match using information from all the segments. Therefore, the so-called minimum-cost algorithm that has been successfully applied for automatic contour detection in other clinical images has been used as a global optimization technique [8,9]. Details of this algorithm are described in Appendix I. The algorithm makes use of dynamic programming techniques to find a path that has the overall minimal cost in a cost matrix. In our case the cost values are defined by a correlation coefficient that

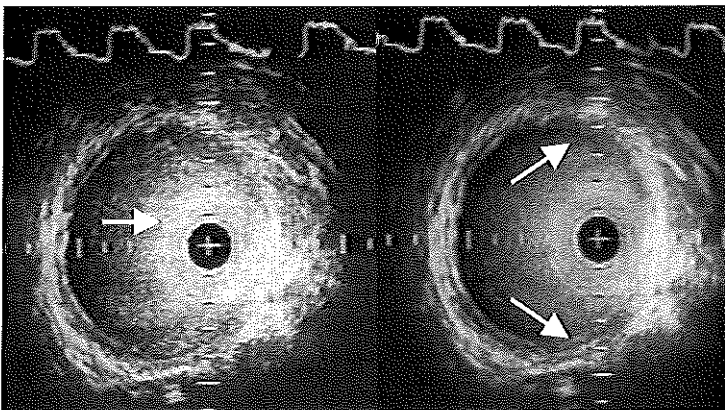


*Fig. 1. Left: A single frame of an arterial cross-section showing the echoes from flowing blood. Right: Time-averaged image showing enhancement of the luminal boundary (arrows).*

reflects the goodness of the match at different radial positions. The path derived by the minimum-cost algorithm represents an optimal match in the sense of satisfying constraints on connectivity and smoothness. The matching procedure has the following steps:

First, polar transform is performed on the single frame using the same centerpoint as the reference frame. The transformed array is shown in Fig. 2a. The use of the same centerpoint for all the frames permits analysis of the wall displacement with the same reference position.

The next step is to define a running search window by expanding the previously tracked luminal contour  $-W$  and  $W$  pixels in the radial direction. This dynamic adjustment of the searching region has the effect of using the previously detected positions as a model in the minimum-cost algorithm. The left and right dotted lines in Fig. 2b delineate the data to be cross-correlated with the templates. Then, a normalized cross-correlation coefficient between the template  $\{X_i(l,k)\}$  and the data in its corresponding segment  $\{Y_i(l,k)\}$  is calculated by:

$$C_{i,j} = \frac{\sum_{l=0}^L \sum_{k=0}^K (X_i(l,k) - \bar{X}_i)(Y_i(l,k+j) - \bar{Y}_i)}{\sqrt{\sum_{l=0}^L \sum_{k=0}^K (X_i(l,k) - \bar{X}_i)^2 \sum_{l=0}^L \sum_{k=0}^K (Y_i(l,k+j) - \bar{Y}_i)^2}},$$

where  $i = 1, \dots, I$  is the number of segments and  $j = 1, \dots, J$  is the radial displacement in relation to the start position of the search window. A cost matrix is generated from these  $I$  by  $J$  coefficient values (Fig. 2c). The total cost for a path from the top to the bottom line is evaluated over all possible paths in this matrix and the one with the minimal cost is found by the algorithm, shown in Fig. 2d. Finally, a set of displacement values is calculated from the differences between the path and the template position.

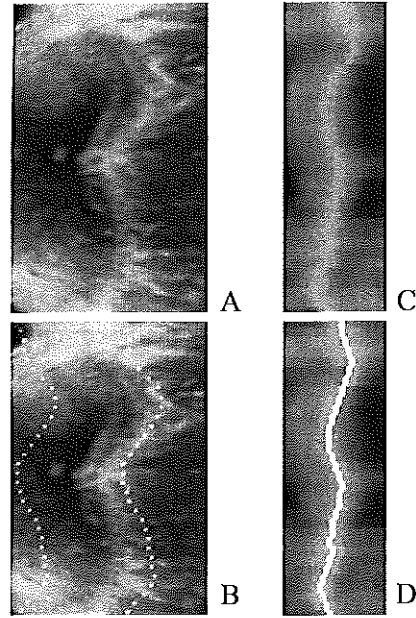
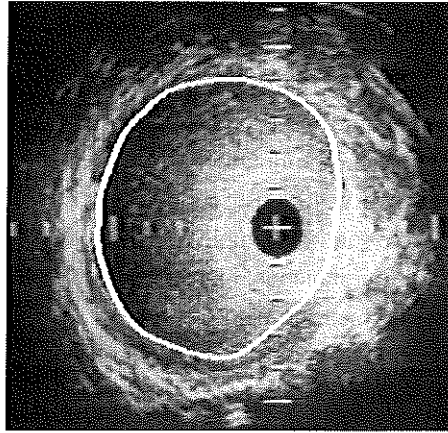


Fig. 2. A) transformed array. B) search region defined by the left and right lines. C) cost matrix. D) minimal cost path

### *Border estimation*

To obtain the absolute measurement of the lumen area, the last step in the analysis procedure is to estimate the luminal border from the displacement information and the manually derived contour. The precise definition of the luminal edge in each segment can be extracted from the manually defined contour by grouping the contour points according to their angles. By modifying every contour point in the group with its corresponding displacement value, the circumferential luminal contour is obtained after interpolating and smoothing the contour pieces from all the segments on the single frame (Fig. 3).



*Fig. 3. The luminal contour as derived from the wall displacement.*

### **2.3 Validation study**

To evaluate our method, measurements were performed on in vivo echograms of peripheral arteries acquired from 8 patients. For each patient, one cross-section with visible pulsation of the arterial wall was selected from the echograms and the luminal area was measured frame-by-frame over two cardiac cycles by two independent observers. One observer used the semi-automatic tracking method and the other traced all frames manually with a mouse. Since the measure of the luminal area change is more important than its absolute value in compliance studies, the difference in the area between two consecutive frames ( $\delta A = A_i - A_{i+1}$ ) was used as the first parameter to compare the two methods. The mean difference between the two methods was calculated from the values of the paired difference of  $\delta A$ . Second, to evaluate the reproducibility of the measurement, beat-to-beat variations were estimated separately for both methods with data from two cardiac cycles. The measurements obtained in the two consecutive cycles were grouped in pairs according to the cardiac phase. The standard deviations of the paired data were calculated. A percent variation coefficient defined by the ratio of the standard deviations and their mean values was used to provide a quantitative measure of beat-to-beat variations.

## 2.4 Animal study

Proximal iliac arterial compliance was measured in 7 pentobarbital-anesthetized pigs, before and during local infusion of adenosine and norepinephrine. Luminal area was measured every 40 milliseconds by means of the semi-automatic tracking program. Simultaneous high-fidelity pressure measurements were obtained by means of a catheter-tipped pressure microtransducer positioned at the origin of the iliac artery. Linear regression analysis of the area/pressure relationship in two consecutive cardiac cycles (systolic phase only) was performed before and during adenosine and norepinephrine infusion. *Arterial compliance* was defined by the slope of the area/pressure regression line. Measurements after three minutes of infusions of adenosine (5-5000 g/minute) and norepinephrine (0.001-10 g/minute) were compared with the control measurements. Fig. 4 shows a typical compliance measurement. The measured curve of the luminal area derived from two cardiac cycles is plotted as a function of time (upper). The corresponding internal blood pressure measurement is shown on the lower panel. The luminal area changes approximately 7% from systole to diastole. The compliance index was derived from the relationship between the area and pressure curves during the systolic phase.

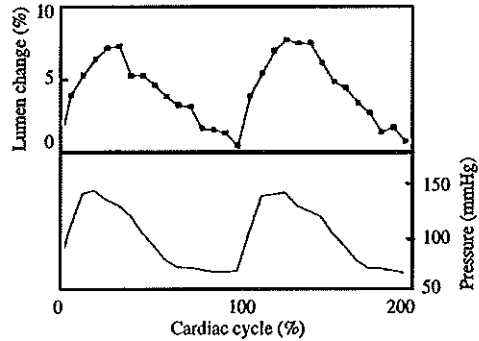


Fig. 4. The percent change of the luminal area in two cardiac cycles (upper) and the internal blood pressure measurements (lower). The lumen area change was 7%.

consecutive cardiac cycles (systolic phase only) was performed before and during adenosine and norepinephrine infusion. *Arterial compliance* was defined by the slope of the area/pressure regression line. Measurements after three minutes of infusions of adenosine (5-5000 g/minute) and norepinephrine (0.001-10 g/minute) were compared with the control measurements. Fig. 4 shows a typical compliance measurement. The measured curve of the luminal area derived from two cardiac cycles is plotted as a function of time (upper). The corresponding internal blood pressure measurement is shown on the lower panel. The luminal area changes approximately 7% from systole to diastole. The compliance index was derived from the relationship between the area and pressure curves during the systolic phase.

## 2.5 Patient study

Twenty-eight patients with disabling claudication (mean age 65 years) were scheduled for balloon angioplasty (iliac artery in 7 and superficial femoral artery in 21 patients). The common femoral artery was cannulated with a 7F introducer sheath and the ultrasound catheter was advanced into the iliac or superficial femoral artery. Under fluoroscopic guidance the position of the catheter tip was marked using a radiopaque reference ruler [18]. The electrocardiogram was registered simultaneously with the ultrasound studies. At levels of interest, the catheter was not moved during at least 10 seconds to acquire sufficient images for the distensibility study.

In 10 patients, initial inspection showed that free lumen area remained unchanged during one cardiac cycle. From the remaining 18 patients, a total of 135 cross-sections



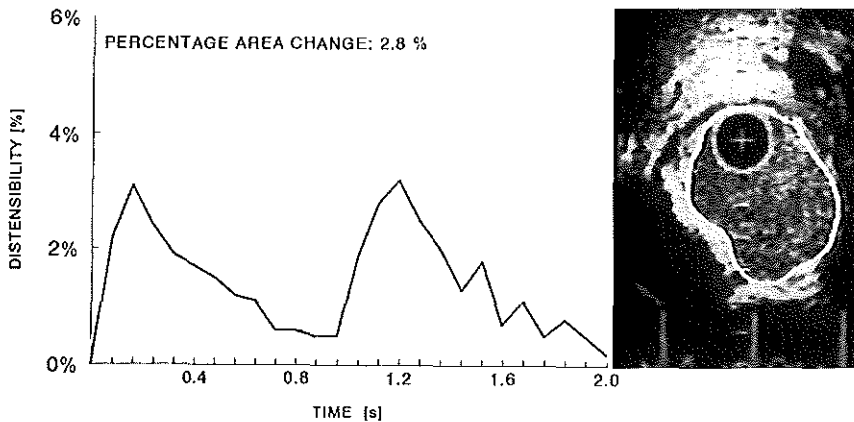


*Fig. 5. Distensibility (%) measured in a femoral arterial cross-section showing an eccentric-hard lesion (<50% stenosis). The percentage lumen area change was 2.8%.*

underwent quantitative analysis. *Arterial distensibility* was defined as the area difference between the systolic and diastolic measurements divided by the mean lumen area registered during the two cardiac cycles. Cross-sections without a lesion were compared with those showing <50%, 50~90% and >90% area stenosis. The effect of balloon angioplasty on the arterial distensibility was evaluated with data obtained before and after intervention. An example of the distensibility measurement in a hard lesion is shown in Fig. 5.

### 3 RESULTS

#### 3.1 Validation study

The mean difference between the two methods for the measure of the area change was minimal (mean difference  $\pm$  SD:  $0.013 \pm 0.59 \text{ mm}^2$ ,  $p > 0.05$ ). The beat-to-beat variation in data from the semi-automatic method was smaller than that from manual tracing (computer: 1.0% vs manual 2.7%).

#### 3.2 Animal study in large artery compliance

Even at the highest infusion rate, adenosine did not significantly increase arterial compliance compared with baseline ( $25 \pm 7$  vs  $19 \pm 4 \text{ mm}^2/\text{mmHg} \times 10^{-3}$ , respectively,  $p = \text{ns}$ ). In contrast, norepinephrine decreased arterial compliance compared with the second baseline control ( $13 \pm 3$  vs  $20 \pm 3 \text{ mm}^2/\text{mmHg} \times 10^{-3}$ , respectively,  $p < 0.01$ ).

### 3.3 Patient study in regional distensibility

The distensibility data associated with the area stenosis are summarized Table 1. Distensibility values in iliac arteries were significantly higher than those in femoral arteries. In addition, no significant change in distensibility was evidenced when lesion volume increased up to 90% stenosis both in iliac and femoral arteries. Conversely, a significant decrease in distensibility (0.4%) was observed in four femoral artery cross-sections (three patients) in which the percentage area stenosis was >90% ( $p < 0.05$ ). Lesions with > 90% stenosis were not found in the iliac artery.

The influence of balloon angioplasty on arterial distensibility was more marked in iliac than in femoral arteries. In iliac arteries, distensibility increased significantly from  $5.3 \pm 3.0\%$  pre-intervention to  $8.2 \pm 3.1$  post-intervention ( $p < 0.05$ ); in femoral arteries, the distensibility showed practically no change after intervention:  $2.5 \pm 1.8\%$  before vs  $2.8 \pm 1.5\%$  after intervention.

Table 1: Distensibility (%) in iliac and femoral arteries grouped according to the degree of percentage area stenosis.

|         | NO LESION | <50% | 50-90% | >90% |
|---------|-----------|------|--------|------|
| Iliac   | 6.5%      | 5.8% | 9.3%   | -    |
| Femoral | 3.5%      | 2.4% | 3.1%   | 0.4% |

## 4 DISCUSSION

A method that measures changes in luminal area by of analyzing the regional wall displacement rather than direct detection of the lumen boundary. Use of the minimum-cost algorithm in the decision unit enforces the connectivity and smoothness constraints of a physical object. As this method maximizes use of image information, it is insensitive to image noise and disturbance caused by the blood echoes and, therefore, allows accurate estimation of the luminal border with absence of a clear blood-wall interface in a still frame. The cross-correlation coefficient used for the matching is a powerful similarity measure that is independent of variations in amplitude and baseline, but rather computationally intensive. In our implementation, the processing time has been limited to a few seconds as the matching processing for each segment is carried out only along one direction in a small range.

Change in lumen area was in the order of 5% in the wall distensibility study. Thus, a high beat-to-beat reproducibility is essential for the measurement of such a small change. As expected, the beat-to-beat variation in the manual method was relatively high due to observer variability in the manual contour tracing. With the semi-automatic tracking method, the variation was reduced to 1% of the mean lumen area. The only

user interaction in this method is the manual definition of the luminal border on the reference image. Since the borders are estimated with the same templates in all frames, observer variations in the manual procedure of the semi-automatic approach appear as baseline deviations in each absolute area measurement, which may not affect the accuracy in measurement of the changes between frames.

The animal study demonstrated the ability of IVUS to serially measure arterial compliance *in vivo* and to determine the resting tone of the artery by its response to vasodilating and vasoconstricting pharmacologic agents. Arterial compliance of the iliac artery was not significantly altered by the infusion of adenosine but was significantly decreased by norepinephrine. Thus, it appears that resting large artery tone in this experimental preparation is low.

The preliminary patient study has established baseline values on vessel wall distensibility in diseased iliac and superficial femoral arteries. Arterial distensibility was determined by the nature of the lesion; hard lesions had reduced distensibility. Lesion volume influenced distensibility only when there was a significant reduction in luminal area. Vascular intervention increased the distensibility in iliac arteries, whereas no change was found in femoral arteries after intervention. Albeit the clinical value of IVUS for assessment of vascular distensibility needs to be determined, the data presented here may provide a basis for future studies.

There are several potential limitations in the application of IVUS imaging techniques for vessel wall compliance studies. The invasive nature of the methodology raises the possibility that the presence of the ultrasound catheter may affect the accuracy of the measurement of compliance. The distribution of the internal pressure gradient may be altered, inducing changes in the compliance of the arterial wall. When the catheter is attached to the arterial wall, no cardiac contraction can be observed from the wall behind the catheter because the pressure is blocked. Interference of the catheter may be negligible in measurements of a relatively larger artery, but may be significant for the artery with a diameter comparable to the size of the catheter; when smaller ultrasound catheters become available, this limitation will decrease.

In the present study, the relatively low temporal resolution of the IVUS system may limit the accuracy in assessing the rapid change in lumen dimensions. The maximum frame rate of the system was limited to 16 frames per second. This may not be sufficient to reproduce the rising edge of the lumen area curve during the systolic period. Therefore, the maximum value of the lumen area may be underestimated, resulting in underestimation of the wall compliance/distensibility. To reduce this error, measurement of lumen change was performed in more than one cardiac cycle.

## 5 CONCLUSION

A method for frame-to-frame tracking of the luminal border from sequential IVUS images has been developed by combining the cross-correlation and minimum-cost methods for the template-matching, which enables to extract border information from IVUS images containing strong disturbances. Validation data have demonstrated that the accuracy and reproducibility of the method are high for quantifying the frame-to-frame changes in the luminal area. Results from both the animal and clinical studies have shown that this method provides a useful clinical tool for wall compliance/distensibility studies with intravascular ultrasound.

## 6 REFERENCES

1. Barneet GO, Mallos AJ, Shapiro A. Relationship of aortic pressure and diameter in the dog. *J Appl Physiol* 1961;16:545-548.
2. Linker DT, Kleven A, Grønningsæther Å, Yock PG, Angelsen AJB. Tissue characterization with intra-arterial ultrasound: special promise and problems. *Int J Cardiac Imag* 1991; 6: 255-263.
3. Nissen SE, Gurley JC. Application of intravascular ultrasound for detection and quantitation of coronary atherosclerosis. *Int J Cardiac Imag* 1991; 6: 221-230.
4. Reddy KG, Suneja R, Nair RN, Sheenhan HM, Lesnefsky EJ, Hodgson JMcB. In vivo evidence for plaque fracture following PTCA: intracoronary ultrasound imaging of arterial distensibility. *J Am Coll Cardiol* 1992; 19 Suppl A:301A (Abstract).
5. Alfonso F, Macaya C, Goicolea J, Hernandez R, Segovia J, Zamorano J, Banuelos C, Zarco P. Determinants of coronary compliance in patients with coronary artery disease: An intravascular ultrasound study. *J Am Col Cardiol* 1994;23:879-884.
6. Li W, Gussenhoven WJ, Zhong Y, The SHK, Di Mario C, Madretsma S, Van Egmond FC, De Feyter P, Pieterman H, Van Urk H, Rijsterborgh H, Bom N. Validation of quantitative analysis of intravascular ultrasound images. *Int J Cardiac Imag* 1991;6: 47-253.
7. Pasterkamp G, van der Heiden MS, Post MJ, Ter Haar Romeny B, Mali WPTM, Borst, C. Discrimination of intravascular lumen and dissections in a single 30 MHz ultrasound image: use of 'confounding' blood backscatter to advantage. *Radiology* 11993;87:871-872.
8. Bosch JG, Reiber JHC, Burken G van, Gerbrands JJ, Gussenhoven WJ, Bom N, Roelandt JRTC. Automated endocardial contour detection in short-axis 2-D echocardiograms: methodology and assessment of variability. in *Proc. Comput. Cardiol. Conf.*, 1988: 137-140.

9. Gerbrands JJ, Hoek C, Reiber JHC, Lie SP, Simoons ML. Minimum cost contour detection in technetium-99m gated cardiac blood pool scintigrams. in Proc. Comput. Cardiol. Conf., 1982: 253-256.
10. Peterson LH, Jensen RE, Parnell J. Mechanical properties of arteries in vivo. *Circ Res* 1960;8:622-639.
11. Stone DN, DuJardin J-PL. Changes in smooth muscle tone influence characteristic impedance of the aorta. *Am J Physiol* 1984;246:H1-H7.
12. Alicandri CL, Fariello R, Agabiti-Rosei E. Influence of the sympathetic nervous system on aortic compliance. *Clin Sci* 1980;59:279s-282s.
13. Pagani M, Schwartz PJ, Bishop VS. Reflex sympathetic changes on aortic diastolic pressure-diameter relationship. *Am J Physiol* 1975;229:286-290.
14. Pagani M, Mirsky I, Baig H. Effects of age on aortic pressure-diameter and elastic stiffness-stress relationship in unanesthetized sheep. *Circ Res* 1979;44:420-429.
15. van Boretl LM, Hoeks APG, Kool MJF, Struijker-Boudier HA. Introduction to large artery properties as a target for risk reduction by antihypertensive therapy. *J Hypertens* 1992;10:S123-S126.
16. Isnard RN, Pannier BM, Laurent S, London GM, Diebold B. Pulsatile diameter and elastic modulus of the aortic arch in essential hypertension: A noninvasive study. *J Am Coll Cardiol* 1989;399-405.
17. Park JC, Siegel RJ, Demer LL. Effect of calcification and formalin fixation on in vitro distensibility of human femoral arteries. *Am Heart J* 1993;125:344-349.
18. The SHK, Gussenhoven WJ, Zhong Y, Li W, Van Egmond FC, Pieterman H, Van Urk H, Gerritsen P, Borst C, Wilson R, Bom N. Effect of balloon angioplasty on femoral artery evaluated with intravascular ultrasound imaging. *Circulation* 1992;86:483-493.



**THREE-DIMENSIONAL RECONSTRUCTION  
AND VOLUMETRIC QUANTIFICATION  
OF INTRAVASCULAR ULTRASOUND**

W. Li, C. von Birgelen, A. Hartlooper, A. van der Lugt,  
F.C. van Egmond, C. Di Mario, E. Boersma, N. van der Putten,  
J. G. Bosch, E.J. Gussenhoven, J.H.C. Reiber, N. Bom, J.R.T.C. Roelandt.

Based on the publications:

Semi-automatic contour detection for volumetric quantification of intracoronary ultrasound. In: *Computers in Cardiology 1994. IEEE Computer Society Press 1994: 277-280.*

Three-dimensional quantification of intravascular ultrasound images. *Journal of Vascular Investigation 1995(1): 57-61*





**ABSTRACT**

The tomographic nature of intravascular ultrasound imaging techniques allows three-dimensional reconstruction of a vessel of an entire vascular segment. Volumetric quantification of the vessel lumen and plaque can be derived from a sequence of echographic slices. This chapter introduces various techniques to obtain an optimal reconstruction and display of the three-dimensional intravascular ultrasound data. A semi-automatic approach for detection of the lumen and plaque contours on a slice sequence has been developed that optimizes the contour detection algorithm by combining information from two perpendicular longitudinal views. This method is able to provide accurate and reproducible measurements of lumen and vessel volumes.

**1 INTRODUCTION**

Intravascular ultrasound (IVUS) is a real-time tomographic imaging technique that displays the cross-sectional arterial lumen and wall components of different vessel positions in a sequential fashion. Although the experienced medical mind is capable of three-dimensional (3D) conceptualization of complex structural morphology and pathology from the sequential display, a thorough understanding of the spatial relations of this information requires repeated review of the IVUS images recorded at different vessel positions. Computerized 3D reconstruction allows visualization of these tomographic data in their longitudinal relation to the proximal and distal segments and provides a more objective spatial picture and a potential gateway to quantification [1-15]. By performing a slow pull-back of the echo-catheter, a series of longitudinally stacked IVUS slices can be acquired to reconstruct the vessel over the entire narrowed segment in a 3D space. Volumetric measurements of the lumen and plaque can be obtained by means of image segmentation procedure whereby the contours of the structure such as the intima and media are identified on a cross-sectional image [16-18]. A typical IVUS 3D processing consists of a number of steps as illustrated in Fig. 1. Among the 3D processing steps, video data acquisition and image segmentation are the most critical [6,7,19-21].

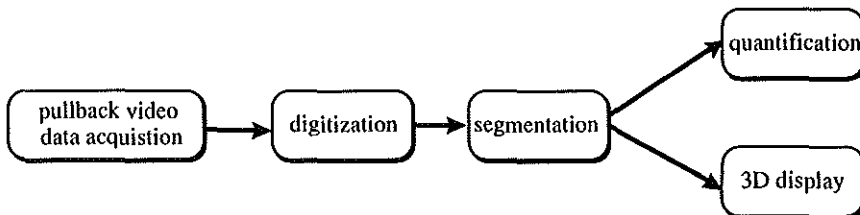


*Fig. 1. Basic steps in IVUS 3D reconstruction.*



real-time video display, it can be used for other purposes, for example, finding two corresponding cross-sections before and after intervention. Validation results of this device have been reported [23].

## **2.2 Registration technique II: Motorized pull-back**

The pull-back can also be performed using a motorized device specially designed for a 2.9F (diameter: 1 mm) imaging echo-catheter with mechanical flex shaft rotation method [24]. In this approach, the transducer is withdrawn inside the catheter by the motor at a constant speed (Typically: 1 mm/s). Since the pull-back speed is known, the longitudinal position of the transducer is merely determined by the time. The longitudinal resolution of this method depends on the pull-back speed as well as the frame rate of the imaging system. For the speed of 1 mm/s, a scan rate of 10 frames per second is required in order to obtain a resolution of 0.1 mm.

## **2.3 ECG-gated data acquisition**

To remove the artifacts caused by the cardiac motion, electrocardiograph (ECG) gating techniques can be incorporated using a dedicated device. The device detects the QRS peak of the ECG signal and marks the corresponding ultrasound image with a white box on the video. The superimposed video marker is then detected by the off-line system to acquire images from the same phase, i.e., the peak QRS or any related delay timing in the cardiac cycle. Because the data acquisition is synchronized with ECG timing, the thickness of slice is no longer uniform due to the variations in the patient heart rate. Therefore, the slice thickness of each cross-section needs to be calculated for volumetric quantification.

A more accurate approach is the use of a stepwise pull-back device in combination with ECG-gating techniques [25,26]. In this approach echographic slices are acquired at a fixed spatial interval (Typically: 0.2 mm) using a dedicated 3D work station (Echoscan, TomTec, Munich, Germany). The advantage of the ECG-gated pull-back procedure is its capability to skip abnormal heart beats, which ensures that the 3D data set only contains images with a normal and reproducible cardiac motion.

## **2.4 Image digitization**

The pull-back IVUS image sequence recorded in video formats needs to be digitized and stored in the computer memory for the subsequent 3D processing. In order to analyze the complete diseased vessel segment with a sufficient longitudinal resolution, a powerful computer with sufficient internal memory is mandatory for storing and processing a large amount of image data. The computer system used in this study is a Pentium (60 MHz) system with 16 MB of internal RAM. The IVUS images recorded on S-VHS/VHS videotape are digitized at a resolution of 800 x 600 x 8 Bits by a framegrabber (DT-3852).

To limit the amount of digital data, a region of interest is selected on the video screen. A total of up to 200 slices can be acquired at a maximum frame rate of 20 f/s and stored in the computer memory. Separate software interfaces have been integrated in the system to support different video acquisition techniques plus ECG gating.

### 3 IMAGE SEGMENTATION

The purpose of the image segmentation procedure is to define the regions of the vessel lumen and lesion on each ultrasound cross-section. The luminal area is defined by the leading edge of the arterial wall. To estimate the size of the total cross-sectional area of the vessel, the interface between intima-media complex and adventitia is identified. Several techniques have been developed to detect these boundaries automatically. A simple approach is the gray-scale threshold method that separates the lumen and tissue based on gray intensity [5,27]. A more elaborate solution is the blood speckle identification algorithm that detects the blood scattering echoes by means of statistical pattern recognition [7,11,28]. An alternative approach is the sequential contour detection based on dynamic programming techniques [29-33]. This technique makes use of a global optimization rule to find the boundary and can be used to detect the lumen and media contours. Since the optimization technique is robust to image noise, it has been widely used in the fields of medial image processing, particularly in contour detection on ultrasound images. Application of the above-mentioned techniques, however, is often hampered by the lack of sharpness of the lumen-wall interface, the similar acoustic properties of the plaque and adventitia and the interference from blood scattering. To provide an efficient method that is able to deal with images of various quality, a semi-automatic approach based on the minimum cost algorithm has been developed.

#### 3.1 Minimum cost algorithm

The minimum cost algorithm is an efficient method developed from dynamic programming techniques. Detailed description of this technique is presented in Appendix I. In brief, the digitized ultrasound data are resampled into a rectangle format using a circular model (Fig. 3a and 3b). A cost matrix is yielded from the resampled data, in which each element represents the edge strength or the possibility to be an edge point (Fig. 3c). For detection of the luminal boundary, the cost value is defined by the spatial first-derivative method; large changes in the echo intensity will produce low cost values in the matrix. This method permits detection of the luminal edge that contains a significant contrast in gray levels. The media interface, however, is usually recognized by its black-ring appearance rather than by the changes in image intensity. Edge enhancement based on the gradient of gray levels is unable to produce sufficient

contrast for discrimination of the media boundary. To detect this interface, a pattern matching processing by cross-correlation is adopted for the cost calculations. The value of the cost element is defined by the normalized cross-correlation coefficient between a line pattern and the resampled data. Low cost values will be assigned to the points with high similarity levels. Next, through the cost matrix a path with the smallest accumulated cost is determined by the minimum cost algorithm (Fig. 3d). This path is globally optimized in terms of connectivity and smoothness. Finally, the points in the path are transformed back to the image coordinates, and interpolated to generate a circumferential outline (Fig. 3e).

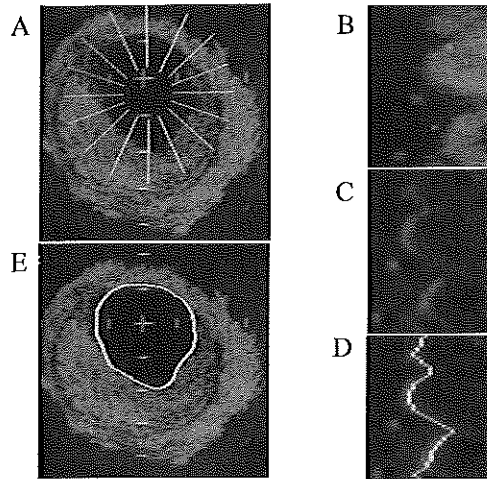


*Fig. 3. (A) Image resampled along the scan lines for the lumen detection. (B) Resampled data shown in the polar format. (C) Cost matrix displaying low cost values with high gray levels. (D) Path determined by the minimal cost algorithm. (E) Luminal contour derived by transferring the path back to the image*

### 3.2 Semi-automatic contour detection

The semi-automatic contour detection procedure consists of three steps. First, the IVUS image sequence is modeled in a voxel space. Two perpendicular cut planes that are parallel to the longitudinal axis are interactively selected. Data located at the interception of the cut planes and the voxel volume are derived to reconstruct two longitudinal images (Fig. 4). Each row of the longitudinal views represents the image data resampled along the cut line from one slice. Linear interpolation is applied during the longitudinal reconstruction. The angle and location of the cut planes can be interactively changed by the user to obtain an optimal quality of the longitudinal images.

The second step is an interactive tracing procedure that defines the contours of the lumen and plaque on the longitudinal images. The program starts with an automatically detected contour by the minimum cost algorithm. To modify the detected contour, points can be manually added to force the contour passing through the desired position. This is implemented by setting the cost matrix at the manually defined position with a

very low value. The optimal path is then redefined from the modified cost matrix using the minimum cost algorithm. The corresponding XY coordinates of the longitudinal contour are calculated and displayed on the transverse image for visual checking (Fig. 5). For each longitudinal image, two lumen contours and two media contours are traced. Since the cost matrix has been pre-calculated and stored in the memory, the longitudinal contour can be interactively retraced and updated on both the longitudinal and transverse displays.

The third step is the contour detection on each cross-sectional image with information from the longitudinal contours. By transforming the contours from the two longitudinal planes to the transverse plane, four pre-defined points are available for each cross-section. These points indicate the edge positions where the contour should pass through. Using the four edge points, the range and center for boundary searching are determined. The cross-sectional images are then transformed to a polar format. A cost matrix having a very low value at the four pre-defined positions is yielded from the resampled data. Finally, an optimal contour passing through the four edge points is obtained by applying the minimum cost algorithm.

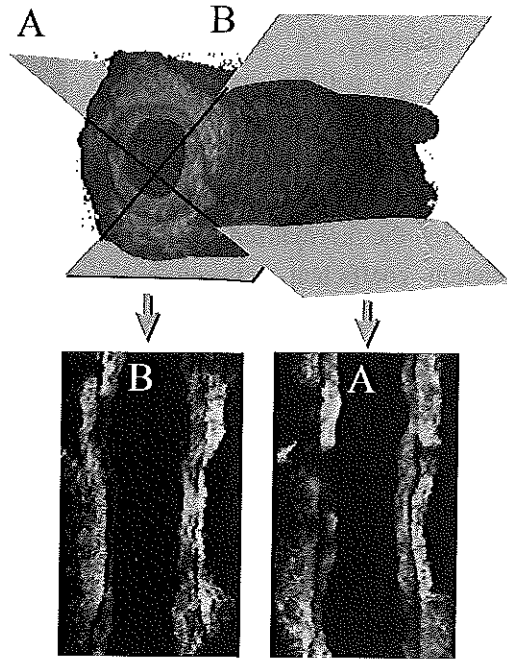


*Fig. 4. Image volume (upper) is intercepted by two perpendicular plane A and B to generate longitudinal display (lower).*

### 3.3 Validation study

A comparison study was designed to validate the semi-automatic method. In this study, contours traced separately with a manual system were used as a gold standard to evaluate the accuracy of the computer derived contours.

**IVUS imaging:** The validation studies were performed using a mechanical IVUS imaging system based on a single ultrasound element (30 MHz); the tomographic image is scanned by rotating the transducer mounted on a guidewire-tipped 4.3F catheter (Du-MED, Rotterdam, The Netherlands, 0.018" or 0.035"). The 3D IVUS data

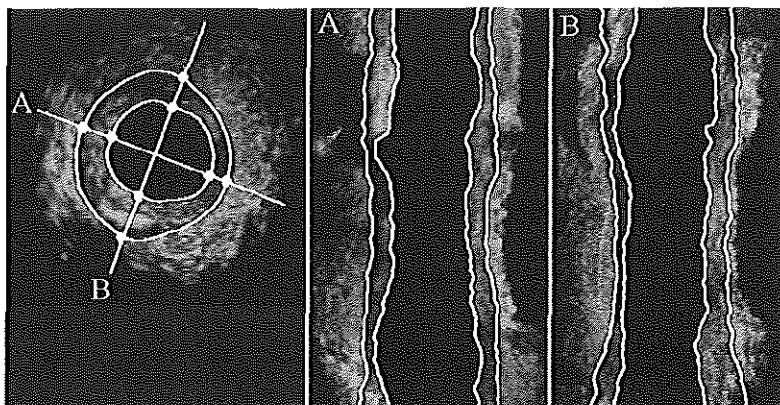


*Fig. 5. Contour detection of the 3D IVUS data set. The left panel shows the first cross-section of the 200 slices. Lines A and B define the two longitudinal views shown on the right panels. The detected contours of the lumen and media are superimposed on both the transverse and longitudinal images. The corresponding positions of the longitudinal contours on the transverse plane are marked by the circles.*

were acquired before angioplasty. The pull-back of the echo catheter was performed manually and registered with the displacement sensing device.

**Data analysis:** Quantitative measurements were performed in steps of 0.1 mm with the semi-automatic contour detection method and in steps of 2.5 mm by manual contour tracings. A total of 221 cross-sectional images obtained from 10 patients were analyzed. Measurements of lumen and vessel areas obtained with the two methods were compared at the corresponding position. To describe the agreement between the two systems, mean and standard deviation of the paired differences were calculated. Systematic differences between automated and manual measurements were analyzed with the Student's t-test for paired observations. The degree of variation between the two systems was presented as a coefficient of variation, defined as the standard deviation of the paired difference divided by the mean of the absolute value. A p-value  $< 0.05$  was considered statistically significant.

#### 4 VOLUMETRIC QUANTIFICATION

Volumetric measurements of IVUS images can be derived from the detected contours of the lumen and media. The cross-sectional area of the lumen and media are calculated on each echographic slice. The plaque area is calculated by subtracting the free lumen area from the total area of the vessel. The volumes of the lumen and plaque are then calculated with the Simpson's rule:

$$V = \sum_{i=0}^N A_i * H_i$$

where  $A_i$  is the cross-sectional area,  $H_i$  is the thickness of the slice and  $N$  is the number of slices. Resulting quantitative data of the lumen area, plaque area and % area stenosis can be plotted as a function of vessel position to provide immediate assessment of the lesion distribution along the length of the vessel (Fig. 6). Measurements of maximum and minimum diameter, lesion thickness, eccentricity of the vessel lumen and lesion on each IVUS cross-section are provided by the 3D system.

Quantitative measurements can also be performed along the longitudinal direction to derive parameters such as the length of the calcified lesion and the length of the lesion dissection rupture from the 3D data set.

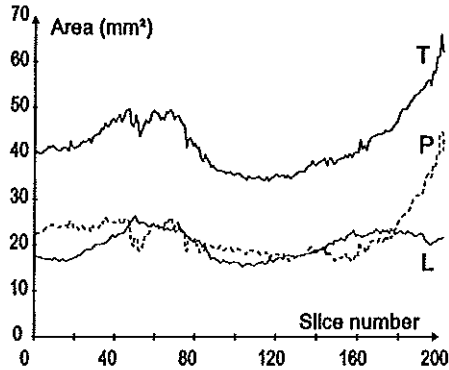


*Fig. 6. Cross-sectional area measurements of the lumen (L), total vessel area (T) and plaque (P) plotted as a function of the vessel position. The volumes of the lumen and plaque measured over a vessel length of 4 cm are 815.9 mm<sup>3</sup> and 1715.5 mm<sup>3</sup>, respectively*

## 5 THREE-DIMENSIONAL RECONSTRUCTION

### 5.1 Voxel modeling

Once the image segmentation has been performed, the 3D arterial objects can be reconstructed using a 3D model. Two computer models, wire mesh and voxel modeling, are most commonly used to describe a 3D object. The wire mesh model represents the surface of an object by a set of connected curves. Each curve can be simply defined by the 3D coordinates  $(x, y, z)$ , which requires only small amount of computer memory. The method is suitable for reconstruction of a 3D object with smooth surfaces, particularly an artificially created object, but may fail to depict structures with a complex geometry like a diseased vessel. The voxel model is a volume-based modeling method that divides the 3D space into many small volume elements or so-called "voxel" arranged side by side [34]. An important feature of this modeling method is that it always represents volumes, thus independent of the complexity of the object surface. In this modeling approach, a pixel on the 2D echo image is extended to a 3D voxel element defined by the coordinates of its center  $(x, y, z)$ . Each voxel is classified as a member of either the lumen or the wall structures by the detected contours. The longitudinal resolution (along  $z$  plane) of a 3D IVUS data set is usually lower than the cross-sectional (along  $x, y$  planes) resolution due



to a limited slice number; data interpolation between two consecutive slices is often performed to obtain a cubic voxel.

## 5.2 Rendering methods

A 3D object reconstructed by the computer cannot be directly visualized on a 2D display device such as a monitor screen; the reconstructed data usually requires to be projected back on a 2D space with a rendering procedure. Various rendering techniques can be applied to archive effects like object transparency or mimic certain types of materials. Additionally, the reconstructed object can be displayed in perspective to enhance the depth perception. For visualization of 3D IVUS data, a rendering procedure based on the depth-gradient shading method is used. The brightness of the projected image is determined by the weighted sum of three components: 1) the depth of a voxel to provide distance perception; 2) the gradient vector of a voxel to describe the orientation of the voxel surface; 3) the gray scale value of a voxel to display the original echo information of the wall structures. The value of the depth-gradient shading is related to the position of the defined light source. When the source is placed in front of the volume, the voxel that is closer to the view point has a brighter gray intensity. Analogously, the voxel with a surface normal to the light source is displayed with a high intensity. An example of the three rendering components is shown in Fig. 7. The final 3D display is obtained with weighting factors of 0.2, 0.4, 0.4 for distance shading, gradient shading and voxel gray value, respectively. The weighting factors of the three components can be adjusted interactively to obtain an optimal display of the reconstructed vessel. Alternatively, the lesion volume can be encoded with a different color to provide a higher contrast to the normal wall tissue.

## 5.3 Display formats

Various display formats are used to emphasize the different structures of interest [6,7]. The most common used modalities include three display formats: 1) longitudinal display reconstructed from an arbitrary angle of the cutting plane; 2) "clam-shell" view that cuts and opens up the 3D volume longitudinally; 3) lumen cast that displays only the lumen volume as a 3D solid object.

# 6 RESULTS

## 6.1 Validation results

Comparison of the semi-automated contour detection and manual contour tracing is summarized in Table 1. A small but statistically significant difference in vessel area

measurements was found between the two approaches ( $-0.46 \pm 2.60 \text{ mm}^2$ ,  $p = 0.02$ ). No significant difference between the two methods was found for the lumen area ( $0.20 \pm 2.52 \text{ mm}^2$ ,  $p = 0.23$ ). The coefficient of variation for lumen area and vessel area was 16.8% and 8.0%, respectively.

Table I: Data represent mean and standard deviation

|                          | LUMEN AREA ( $\text{mm}^2$ ) | VESSEL AREA ( $\text{mm}^2$ ) |
|--------------------------|------------------------------|-------------------------------|
| Manual                   | $14.90 \pm 8.22$             | $32.69 \pm 12.04$             |
| Automated                | $15.11 \pm 7.73$             | $32.23 \pm 11.52$             |
| Paired difference        | $0.20 \pm 2.52$ (NS)         | $-0.46 \pm 2.60$ (S)          |
| Coefficient of variation | 16.8%                        | 8.0%                          |

NS: Not significant; S: Significant.

In average, the required analysis time was 0.15 min/frame with the semi-automatic method and 2~6 min/frame with the manual tracing system. During the tracing of the longitudinal contour, approximately 3~5 markers were manually added. The total time to acquire and analyze a 3D IVUS recording with 200 cross-sections was in the range of 25~30 minutes.

## 6.2 Three-dimensional reconstruction

The longitudinal display is a built-in function in the semi-automatic detection system. The simultaneous display of the original cross-section with the derived longitudinal view offers an oriented mapping of quantitative/qualitative analysis on each slice to the entire vessel segment. This display format is considered to be a standard display in clinics. Fig. 8 shows visualization of a set of original IVUS cross-sections (left panel)

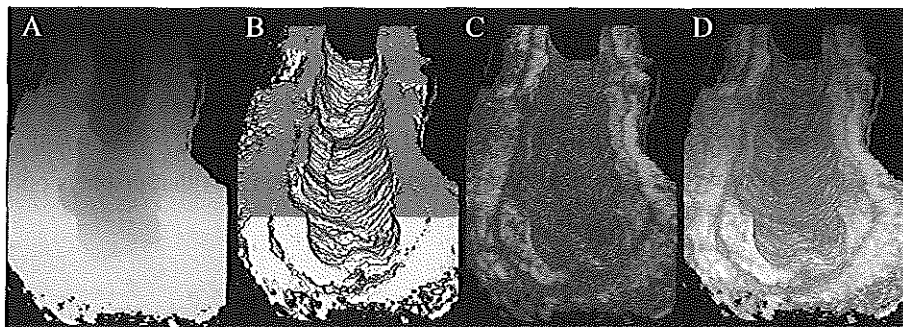
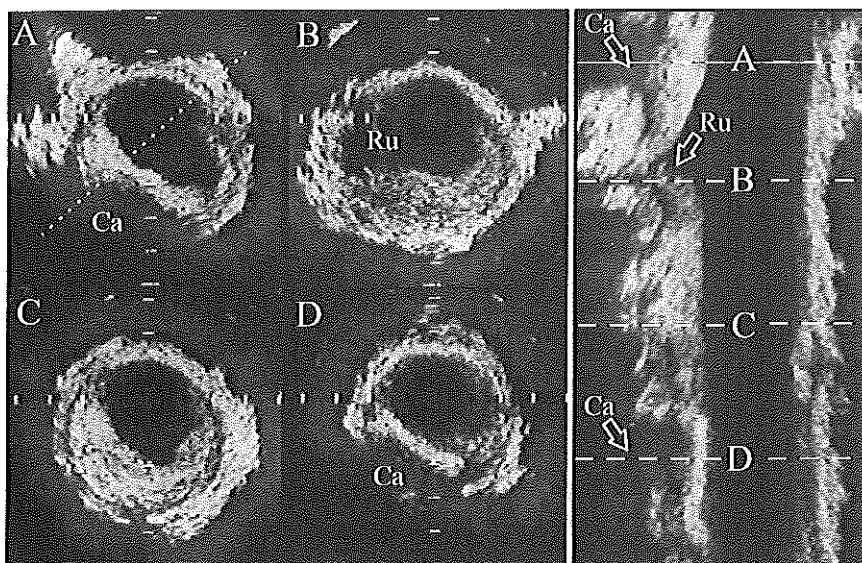


Fig. 7. A) Component of the depth shading. B) Component of the gradient shading. C) Component of the original echo intensity. D) 3D display by combining the three components with weighing factors of 0.2, 0.4 and 0.4 for the depth, gradient and echo intensity, respectively.



*Fig. 8. Left: Four IVUS cross-sections of a coronary artery showing eccentric lesion distributions on (A, B, C, D), calcified lesion (A, D) and wall rupture (B). Right: The longitudinal display with four horizontal lines indicating the corresponding vessel positions of the IVUS cross-sections. Calcified lesion and rupture are indicated by Ca and Ru, respectively. Note dramatic changes in the lumen shapes, which may not be easy to interpret without the help of the longitudinal views.*

and the longitudinal reconstruction (right panel). The longitudinal view depicts clearly the 3D geometric relationship of the different morphologic features such as plaque calcification and rupture, thus allowing easier interpretation of the significant changes of the lumen and lesion on individual echographic slices. The longitudinal images may also be used to overcome the problem of echo drop-outs by connecting information from different slices.

Fig. 9 shows a "clam-shell" display of a diseased coronary artery reconstructed from 200 slices. This display format allows inspection of the interior lumen structure and the distribution of the lesion along the vessel segment. The roughness of the lumen surface is well appreciated from the 3D display. An example of the lumen cast display format is illustrated in Fig. 10. The solid 3D lumen can be rotated and visualized from different angles to appreciate the change in the lumen shape that varies significantly from a concentric to an eccentric geometry.

## 7 SUMMARY OF THE SEMI-AUTOMATIC APPROACH

Image segmentation is a key step for an accurate 3D quantification of IVUS images. At the current stage of the ultrasound imaging technique, application of a fully automatic segmentation approach is still limited by the image quality. The proposed semi-automatic method has two advantages:

First, it makes use of information from the longitudinal reconstruction to guide contour detection on the transverse images. The four pre-defined longitudinal points provide important prior knowledge about the position and shape of the boundaries, which allows generation of a precise model to limit the edge searching in a small region. Moreover, since the program only searches the contours constrained by the four points, the chance of picking up a wrong contour due to strong noises is reduced.

Secondly, user interaction is incorporated in the minimum cost algorithm, providing possibilities to handle images of various quality. The amount of required manual definition depends mainly on the image quality; for high quality images, such as those obtained in vitro or with ECG-gated acquisition in vivo, the contour detection can run almost automatically.

One limitation of the current semi-automatic approach is that it is based on a predefined geometric model, which allows detection of only one contour point along the resampled line. This approach may fail to detect the luminal contour in the case of very irregular luminal shapes. In particular, manual correction of the luminal contour is necessary for the vessel with dissections or flaps where more than one contour point are needed to define the luminal boundary.

## 8 LIMITATIONS IN 3D IVUS

The 2D echo data are the basis of the 3D reconstruction. Therefore, the IVUS image quality is essential for 3D reconstruction and volumetric quantification. The IVUS



*Fig. 9. Three-dimensional visualization by opening up the IVUS volume along the sagittal plane*

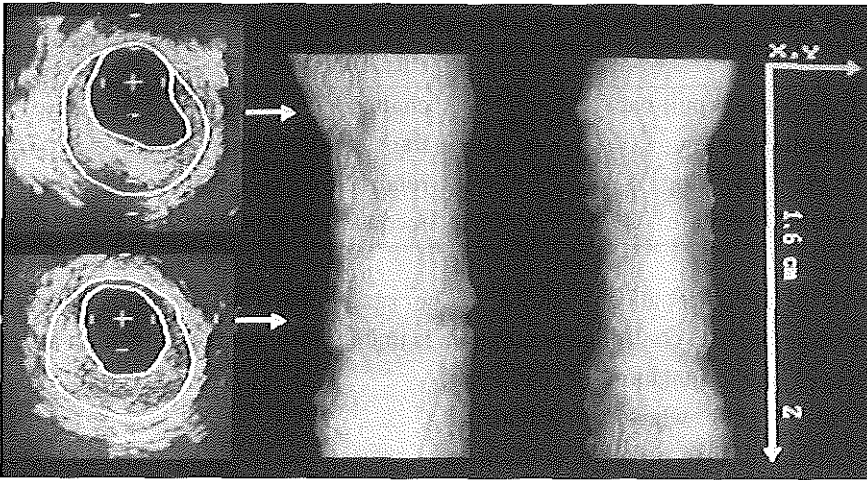


*Fig. 10. 3D display of the lumen reconstructed as a solid model and viewed from the X (left) and Y (right) directions. The change of the luminal geometry along the Z axis is clearly delineated by the two different cast views.*

image quality is limited by a number of factors such as a poor definition of the boundaries of the lumen and plaque due to high blood echogenicity, calcium shadowing and image artifacts [35-37]. A poor image quality may reduce the accuracy of the contour detection algorithm on echographic slices and require more user interaction for contour correction. When a poor boundary exists in only a small portion of a 3D data set, the volumetric data might not be affected significantly because the volume calculation averages out the variations in individual measurements. Furthermore, information available from adjacent slices on the longitudinal display can help to estimate the boundary on the 'problematic' cross-section. For example, the problem of the acoustic shadowing in a calcified lesion could be simply solved by connecting the beginning and ending point of the lesion on the longitudinal image. Thus, processing 3D data has an advantage of dealing with a poor image quality as compared to tracing contour on one cross-section.

The possible errors associated with the 3D pull-back acquisition are listed in Table II. The speed of a motorized pull-back may vary with the changes in the mechanical resistance. The displacement sensing device can be used to solve this problem by providing a feedback of motor speed, which allows a direct measure of the slice thickness.

The relative movement between transducer and wall due to cardiac pulsation induces a translation in slice position, causing discontinuity of the echo data along the longitudinal axis. This image artifact can be minimized using the described ECG-gated

Table II: Limitations on acquisition of 3D IVUS data

| CAUSES                       | PROBLEMS                          |
|------------------------------|-----------------------------------|
| inconsistent pull-back speed | change in slice thickness         |
| cardiac motion               | translation in slice position     |
| catheter twisting            | rotation in slice orientation     |
| vessel curvature             | reconstruction as a straight tube |

methods that acquire all the slices at the same phase of a cardiac cycle. One complication of ECG controlled acquisition is that it prolongs the acquisition time.

Changes in the orientation of the echo image may occur when a mechanical IVUS is twisted. One possible solution to this problem is an image processing method that matches the vessel orientation based on the shape of the cross-sectional data [38].

Since the 3D vessel is reconstructed by stacking the slices along the center of the catheter, a curved vessel is always represented as a straight tube. As a result, the lesion volume may be compressed (underestimate) in the convexity or expanded (overestimate) in the concavity of the vessel [6]. To improve the reconstruction accuracy of a curved vessel, biplane fluoroscopy or angiography can be applied to spatially correct the 3D IVUS data set [39,40]. A new method based on combined use of biplane angiography and 3D intracoronary ultrasound (ANGUS) may in the future help to analyze the true geometry of the vessel lumen and plaque, taking vessel curvatures and catheter bends into account [41]. In Fig. 11, a clinical example of a spatial reconstruction by ANGUS is given, showing a diseased right coronary

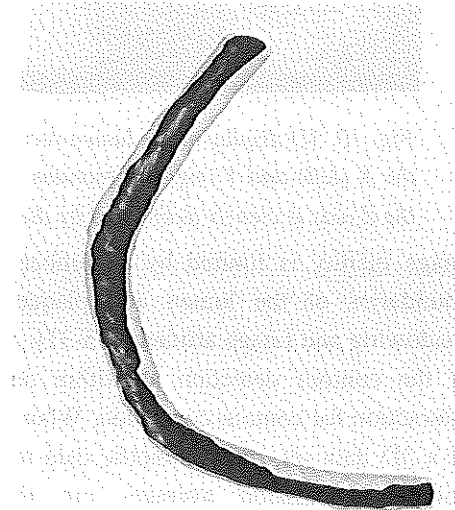


*Fig. 11. Combined use of biplane angiography and three-dimensional intracoronary ultrasound by ANGUS, a new method that allows the analysis of the true geometry of the vessel lumen and plaque, taking vessel curvatures and catheter bends into account. A reconstruction of a diseased right coronary artery is displayed in a frontal projection. Ultrasound data provided by the contour detection method were spatially arranged and interpolated, using biplane data on both the pull-back trajectory and the angiogram.*

artery in frontal projection. Ultrasound data on the intimal leading edge and the external boundary of the total vessel, provided by the contour detection method, were spatially arranged and interpolated, using biplane data on pull-back trajectory and on the contrast angiogram. The example demonstrates that the external contour of the vessel provides additional information which is not available from a silhouette of the lumen provided by the angiogram. This approach may permit a more distinct assessment of the progression or regression of atherosclerosis, an issue that is interesting as plaque progression or regression of the outer and inner curve of a bended coronary segment may differ significantly.

## 9 CONCLUSIONS

Intravascular ultrasonic imaging allows detailed studies of luminal morphology and mural pathology in a vessel cross-sections. 3D reconstruction of these cross-sectional images serves as an important adjunct to obtain comprehensive assessment of the complex spatial distribution of a lesion. Volumetric quantification obtained over an entire vascular segment will provide a more complete evaluation of the atherosclerotic disease. The proposed semi-automatic contour detection method reduces the need for extensive user-interaction during quantitative analysis and offers a practical tool to obtain volumetric measurements from a sequence of IVUS images. Results from the validation study indicate a good agreement between the semi-automatic method and manual contour tracings for measurements of both lumen and vessel areas. Further improvement on this method will permit on-line application during a catheterization procedure, for example, in the guidance and evaluation of the catheter-based intervention.

## 10 REFERENCES

1. Rosenfield K, Losordo DW, Ramaswamy K, Pastore JO, Langevin RE, Razvi S, Kosowsky BD, Isner JM. Three-dimensional reconstruction of human coronary and peripheral arteries from images recorded during two-dimensional intravascular ultrasound examination. *Circulation* 1991; 84: 1938-1956.
2. Coy KM, Park JC, Fishbein MC, Laas T, Diamond GA, Adler L. In vitro validation of three-dimensional intravascular ultrasound for the evaluation of arterial injury after balloon angioplasty. *J Am Coll Cardiol.* 1992;20:692-700.
3. Rosenfield K, Kaufman J, Pieczek A, Langevin RE, Razvi S, Isner JM. Real-time three-dimensional reconstruction of intravascular ultrasound images of iliac arteries. *Am J Cardiol.* 1992;70:412-415.

4. Ennis BM, Zientek DM, Ruggie NT, Billhardt RA, Klein LW. Characterization of a saphenous vein graft aneurysm by intravascular ultrasound and computerized three-dimensional reconstruction. *Cathet Cardiovasc Diagn.* 1993;25:328-331.
5. Mintz GS, Pichard AD, Satler LF, Popma JJ, Kent KM, Leon MB. Three-dimensional intravascular ultrasonography: reconstruction of endovascular stents in vitro and in vivo. *Clin Ultrasound* 1993;21:609-615.
6. Roelandt JRTC, Di Mario C, Pandian NG, et al. Three-dimensional reconstruction of intracoronary ultrasound images: Rationale, approaches, problems and directions. *Circulation* 1994;90:1044-55.
7. von Birgelen C, Di Mario C, Prati F, Bruining N, Li W, de Feyter PJ, Roelandt JRTC. Intravascular ultrasound: three-dimensional reconstruction techniques. In: de Feyter PJ, Di Mario C, Serruys PW (eds). *Quantitative Coronary Imaging*. Rotterdam, The Netherlands: Barjesteh, Meeuwes & Co, 1995: 181-197.
8. Di Mario C, von Birgelen C, Prati F, Soni B, Li W, Bruining N, de Feyter PJ, Serruys PW, Roelandt JRTC. Three-dimensional reconstruction of two-dimensional intracoronary ultrasound: clinical or research tool? *Br Heart J* 1995; 73(Suppl. 2):26-32.
9. von Birgelen C, Slager CJ, Di Mario C, de Feyter PJ, Serruys PW. Volumetric intracoronary ultrasound: a new maximum confidence approach for the quantitative assessment of progression/regression of atherosclerosis? *Atherosclerosis* 1995;118 (Suppl.):S103-S113.
10. von Birgelen C, Di Mario C, Li W, Schuurbijs JCH, Slager CJ, de Feyter PJ, Roelandt JRTC, Serruys PW. Morphometric analysis in three-dimensional intracoronary ultrasound: an in-vitro and in-vivo study using a novel system for the contour detection of lumen and plaque. *Am Heart J* 1996; 132:516-527.
11. von Birgelen C, Gil R, Ruygrok P, Prati F, Di Mario C, van der Giessen WJ, de Feyter PJ, Serruys PW. Optimized expansion of the Wallstent compared with the Palmaz-Schatz stent: online observations with two- and three-dimensional intracoronary ultrasound after angiographic guidance. *Am Heart J* 1996;131:1067-1075.
12. von Birgelen C, Kutryk MJB, Gil R, Ozaki Y, Di Mario C, Roelandt JRTC, de Feyter PJ, Serruys PW. Quantification of the minimal luminal cross-sectional area after coronary stenting: two- and three-dimensional intravascular ultrasound versus edge detection and video-densitometry. *Am J Cardiol* 1996; 78:520-525.
13. von Birgelen C, Di Mario C, Serruys PW. Structural and functional characterization of an intermediate stenosis with intracoronary ultrasound and Doppler: A case of "reverse Glagovian modeling". *Am Heart J* 1996;132:694-696.
14. Gil R, von Birgelen C, Prati F, Di Mario C, Ligthart J, Serruys PW. Usefulness of three-dimensional reconstruction for interpretation and quantitative analysis of intracoronary ultrasound during stent deployment. *Am J Cardiol* 1996;77:761-764.



15. von Birgelen C, van der Lugt A, Nicosia A, Mintz GS, Gussenhoven EJ, de Vrey E, Mallus MT, Roelandt JRTC, Serruys PW, de Feyter PJ. Computerized assessment of coronary lumen and atherosclerotic plaque dimensions in three-dimensional intravascular ultrasound correlated with histomorphometry. *Am J Cardiol* 1996; in press (December 1996).
16. Li W, Gussenhoven WJ, Zhong Y, The SHK, Di Mario C, Madretsma S, Van Egmond FC, De Feyter P, Pieterman H, Van Urk H, Rijsterborgh H, Bom N. Validation of quantitative analysis of intravascular ultrasound images. *Int J Cardiac Imag* 6: 247-253, 1991.
17. Pandian NG, Kreis A, Weintraub A, Motarjeme A, Desnoyers M, Isner JM, Konstam M, Salem DN. Real-time intravascular ultrasound imaging in humans. *Am J Cardiol* 1990; 65: 1392-1396.
18. The SHK, Gussenhoven EJ, Zhong Y, Li W, van Egmond F, Pieterman H, van Urk H, Gerritsen GP, Borst C, Wilson RA, Bom N. The effect of balloon angioplasty on the femoral artery evaluated with intravascular ultrasound imaging. *Circulation* 1992; 86: 483-493.
19. Di Mario C, Li W, Linker DT, De Feyter PJ, Bom N, Serruys PW, Roelandt JRTC. Three-dimensional intracoronary ultrasound. Goals and practical problems. In: *Intravascular Ultrasound 1993* (J. Roelandt, E.J. Gussenhoven, N. Bom, eds.) Kluwer Academic Publishers, Dordrecht 1993: 63-77.
20. Dhawale PJ, Wilson DL, Hodgson JM. Optimal data acquisition for volumetric intracoronary ultrasound. *Catheterization and Cardiovascular Diagnosis* 1994; 32: 288-299.
21. von Birgelen C, Di Mario C, Van der Putten N, Li W, Gil R, Prati F, Ligthart J, Camenzind E, Ozaki Y, Serruys PW, Roelandt JRTC. Quantification in three-dimensional intracoronary ultrasound; importance of image acquisition and segmentation. *Cardiologie* 1995;2:67-72.
22. Egmond FC van, Li W, Gussenhoven EJ, Lancee CT. Catheter displacement sensing device: A new tool for standardization of examinations and three-dimensional image reconstruction. *Thoraxcenter J* 1994;6:9-12.
23. Gussenhoven EJ, van der Lugt A, van Strijen M, Li W, Kroeze H, The SHK, van Egmond FC, Honkoop J, Peters RJG, de Feyter PJ, van Urk H, Pieterman H. Displacement sensing device enabling accurate documentation of catheter tip position. *Intravascular Ultrasound* (J. Roelandt, E.J. Gussenhoven, N. Bom, eds.) Kluwer Academic Publishers, Dordrecht, 1993: 157-166.
24. Mintz GS, Keller MB, Fay FG. Motorized IVUS transducer pull-back permits accurate quantitative axial measurements. *Circulation* 1992;86:1-323.

25. Bruining N, von Birgelen C, Di Mario C, Prati F, Li W, Den Hood W, Patijn M, de Fyter PJ, Serruys PW, Roelandt JRTC. Dynamic three-dimensional reconstruction of ICUS images based on an ECG-gated pull-back device. In: *Computers in Cardiology 1995*. Los Alamitos: IEEE Computer Society Press, 1995: 633-636.
26. Bruining N, Mallus MT, von Birgelen C, Prati F, den Hood W, Patijn M, de Feyter P, Serruys P, Roelandt J. ECG-gated ICUS image acquisition combined with a semi-automated contour detection provides accurate analysis of vessel measurements *Circulation* 1996; 94:L79 (abstract).
27. Matar FA, Mintz GS, Douek P, et al. Coronary artery lumen volume measurement using three-dimensional intravascular ultrasound: Validation of a new technique. *Catheterization and Cardiovascular Diagnosis* 1994; 32: 214-220.
28. Hausmann D, Friedrich G, Sudhir K, Mullen KL, Soni B, Fitzgerald PJ, Yock PG. 3D intravascular ultrasound imaging with automated border detection using 2.9 F Catheters. *J Am Coll Cardiol* 23 (1994), 174A.
29. Bosch JG, Reiber JHC, Burken G van, Gerbrands JJ, Gussenhoven WJ, Bom N, Roelandt JRTC. Automated endocardial contour detection in short-axis 2-D echocardiograms: methodology and assessment of variability. In: *Computers in Cardiology 1988*. Los Alamitos: IEEE Computer Society Press, 1988: 137-140.
30. Li W, Bosch JG, Zhong Y, Gussenhoven WJ, Rijsterborgh H, Reiber JHC, Bom N. Semiautomatic frame-to-frame tracking of the luminal border from intravascular ultrasound. In: *Computers in Cardiology 1991*. Los Alamitos: IEEE Computer Society Press, 1991: 353-356.
31. Li W, Bosch JG, Zhong Y, The SHk, Gussenhoven, Mastik F, Van Egmond FC, Rijsterborgh H, Reiber JHC, Bom N. Image segmentation and 3D reconstruction of intravascular ultrasound images. In: *Acoustical Imaging 1993*; Plenum Press (Y. Wei & B. Gu, eds.), New York 1993 (20): 489-496.
32. Sonka M, Zhang X, Siebes M, et al. Automated segmentation of coronary wall and plaque from intravascular ultrasound image sequences. In: *Computers in Cardiology 1994*. Los Alamitos: IEEE Computer Society Press, 1994: 281-284.
33. Zhu Y, Snyder EW, Braden GA, Herrington DM. A gradient field metric for quality control of automated intracoronary ultrasound boundaries. In: *Computers in Cardiology 1994*. Los Alamitos: IEEE Computer Society Press, 1994: 285-288.
34. Kitney R, Moura L, Straughan K. 3-D visualization of arterial structures using ultrasound and voxel modelling. *Int J Cardiac Imag* 1989; 4: 135-143.
35. Finet G, Maurincomme E, Tabib A, Growley RJ, Magnin I, Roriz R, Beaune J, Amiel M. Artifacts in intravascular ultrasound imaging: analyses and implications. *Ultrasound Med Biol* 1993; 19: 553-547.

36. Benkeser PJ, Churchwell AL, Lee C, Abouelnasr DM. Resolution limitations in intravascular ultrasound imaging. *J Am Soc Echocardiogr* 1993;6:158-165.
37. ten Hoff H, Gussenhoven EJ, Korbijn A, Mastik F, Lancee CT, Bom N. Mechanical scanning in intravascular ultrasound imaging: artifacts and driving mechanisms. *Eur J Ultrasound* 1995;2:227-237.
38. Van Horn MH, Snyder WE, Braden GA, Herrington DM, Intracoronary ultrasound catheter motion compensation using the generalized hough transform. In: *Computers in Cardiology 1994*. Los Alamitos: IEEE Computer Society Press, 1994: 293-297.
39. Evans JL, Kok-Hwee NG, Vonesh MJ, Cursick DA, Morales RE, Tommasso CL, Meyers SN, Roth SI, Kramer BL, Mc Phearson D. Spatially correct three-dimensional reconstruction of intracoronary ultrasound: further validation and initial patient studies. *J. Am Coll Cardiol*. 1993;21:2:181A (abstract).
40. Koch L, Kearney P, Erbel R, Roth T, Ge J, Brennecke R, Meyer J. Three dimensional reconstruction of intracoronary ultrasound images: roadmapping with simultaneously digitised coronary angiograms. In: *Computers in Cardiology 1993*, Los Alamitos: IEEE Computer Society Press, 1993:89-91.
41. Laban M, Oomen JA, Slager CJ, WentzelJJ, Krams R, Schuurbiers JCH, den Boer A, von Birgelen C, Serruys PW, de Feyter PJ. ANGUS: a new approach to three-dimensional reconstruction of coronary vessels by combined use of angiography and intravascular ultrasound. In: *Computers in Cardiology 1995*, Los Alamitos, CA: IEEE Computer Society Press, 1995:325-328.



## CHAPTER 5

---

# **MORPHOMETRIC ANALYSIS IN THREE-DIMENSIONAL INTRACORONARY ULTRASOUND:**

## **An In vitro and In vivo Study Using a Novel System for the Contour Detection of Lumen and Plaque**

**C. von Birgelen, C. Di Mario, W. Li, J.C.H. Schuurbiers,  
C.J. Slager, P.J. de Feyter, P.W. Serruys, J.R.T.C. Roelandt.**



**ABSTRACT**

Current automated systems for quantitative analysis by intracoronary ultrasound (ICUS) are restricted to the detection of the lumen. The aim of this study was to determine the accuracy and reproducibility of a new semi-automated contour detection method, providing off-line identification of the intimal leading edge and external contour of the vessel in three-dimensional ICUS. The system allows cross-sectional and volumetric quantification of both lumen and plaque. It is based on the application of a minimum-cost algorithm and the concept that edge points derived from previously detected longitudinal contours guide and facilitate the contour detection in the cross-sectional images. A tubular phantom with segments of different luminal dimensions was examined *in vitro* during 5 catheter pull-backs (1mm/s) and subsequently 20 diseased human coronary arteries were studied *in vivo*, using 2.9F, 30MHz mechanical ultrasound catheters (200 images/20-mm-segment). The ICUS measurements of phantom lumen area and volume revealed a high correlation with the true phantom areas and volumes ( $r=0.99$ ); relative mean differences were -0.65% to 3.86% for the areas and 0.25% to 1.72% for the volumes of the various segments. Intra- and interobserver comparison showed high correlations ( $r=0.95$  to  $0.98$  for area and  $0.99$  for volume) and small mean relative differences (-0.87% to 1.08%), with SD of lumen, plaque, and total vessel measurements not exceeding 7.28%, 10.81%, and 4.44% (area) and 2.66%, 2.81%, and 0.67% (volume) respectively. Thus, the proposed analysis system provided accurate measurements of phantom dimensions and can be used to perform highly reproducible area and volume measurements in three-dimensional ICUS *in vivo*.

**1 INTRODUCTION**

Intracoronary ultrasound (ICUS) provides arterial cross-sectional images and allows diameter and area measurements of coronary lumen and plaque [1, 2]. These measurements have usually been limited to manual contour tracing of cross-sectional images at the site of the reference segment and the target stenosis. In parallel with the progress in quantitative angiography techniques that started with manual caliper assessment and finally reached computer-assisted methods [3, 4], fully automated methods of quantitative analysis of ICUS have been developed in order to reduce the time of analysis and the subjectivity of manual tracing [5]. These automated systems can be rapidly applied on-line and provide a survey of the vascular geometry for clinical decision-making [6-8]. Because the automated quantitative analysis of these programs is restricted to the detection of the lumen and their success rate frequently is limited [9], a semi-automated system for off-line ICUS analysis of atherosclerotic

coronary segments was developed which detects the intimal leading edge and the external vessel contour on all the individual cross-sectional images, with use of the complete three-dimensional data set obtained during a motorized pull-back of the ICUS transducer [10]. This method permits a volumetric quantification of vessel dimensions by compiling information obtained from the individual cross-sectional images.

The present study was performed to determine the accuracy of this semi-automated contour detection method in tubular phantoms of known dimensions *in vitro* and to evaluate intra- and interobserver variability of area and volume measurements in diseased human coronary arteries *in vivo*.

## 2 METHOD

### 2.1 Phantom study *in vitro*

A tubular paraffin-phantom was constructed and fixed inside a tube of acrylate. The phantom has a circular lumen with a stepwise increase in diameter (2, 3, 4, and 5 mm) thus defining four segments (S2, S3, S4, and S5 respectively) each of 5 mm length (Fig. 1). A paraffin phantom was used as its properties concerning reflection and absorption of ultrasound are similar to those of vessel tissue.

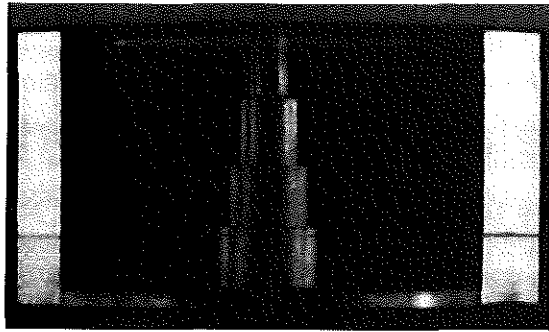


*Fig. 1. Model of the paraffin phantom used in the *in vitro* study. Phantom has a circular lumen and consists of four segments with a stepwise increase in diameter (2, 3, 4, and 5 mm).*

An optical calibration was performed using a calibrated stereo-microscope with forty-fold magnification for the 2-mm-segment and sixteen-fold magnification for all the remaining segments. The mean difference between measurements and the true lumen diameter was  $-15 \pm 41 \mu\text{m}$  at 20°C, the temperature at which the experiments were performed. Temperature dependency of the paraffin phantom was assessed by comparing measurements obtained at 2°C and 37°C (range: 35°C). This resulted in an increase of luminal dimensions of 2%.

Five motorized uniform pull-backs (1 mm/s) of the ultrasound imaging transducer through the paraffin phantom were performed in water (temperature: 20°C) and recorded on video tape. A mechanical rotating ICUS catheter (Microview™, CVIS, Sunnyvale, CA) with a distal external diameter of 2.9F was used. This ICUS imaging



system is equipped with a transparent distal sleeve, covering the rotating imaging core. Using a motorized pull-back system the imaging core is withdrawn inside this sleeve. The design of the catheter and pull-back system minimizes the risk of catheter rotation and facilitates several pull-backs of the echo-transducer without increasing the risk of vessel damage, as the echo-transparent distal sleeve prevents the ICUS-transducer from coming into direct contact with the vessel wall.

## 2.2 Study in vivo

Intraobserver and interobserver variability of the quantification method were studied in 20 ICUS examinations of diseased, non-wedged human coronary segments in vivo. Segments with short calcifications or single major side-branches were included in the study, while an ICUS study with excessive systolic-diastolic movement was not considered for analysis. The maximum and the average cross-sectional area obstruction were  $65.6 \pm 8.8\%$  (range: 83% - 49%) and  $49.2 \pm 6.6\%$  (range: 83% - 17%) respectively. The composition of the study population reflects the current clinical application of ICUS imaging in our center. The characteristics of the patients and the analyzed coronary artery segments are displayed in Table I.

ICUS imaging was performed during motorized pull-backs (1 mm/s) of a 2.9F ICUS catheter. Since the imaging core is straightened during the first seconds of withdrawal, care was taken to start the pull-back 1 cm distal to the segment analyzed. The ICUS examinations were recorded on video-tape and analysis was performed off-line by the new quantitative ultrasound analysis system, using a digitization frame rate of 10 images/s. Thus, 20-mm long coronary artery segments were

**Table I.** Characteristics of patients and coronary artery segments

| Patient (n)             | 20       |
|-------------------------|----------|
| Age (yr)                | 52 ± 9.4 |
| Men (n)                 | 16 (80%) |
| Vessels (n)             |          |
| LAD                     | 15 (75%) |
| LCX                     | 1 (5%)   |
| RCA                     | 4 (20%)  |
| Segments (n)            |          |
| Proximal                | 11 (55%) |
| Middle                  | 8 (40%)  |
| Distal                  | 1 (5%)   |
| Intervention status (n) |          |
| Before intervention     | 3 (15%)  |
| Control after HTX       | 1 (5%)   |
| After PTCA              | 2 (10%)  |
| Follow-up PTCA          | 3 (15%)  |
| After DCA               | 3 (15%)  |
| Follow-up DCA           | 5 (25%)  |
| After stenting          | 3 (15%)  |

*DCA, Directional coronary atherectomy; HTX, heart transplantation; LAD, Left anterior descending coronary artery; LCX, Left circumflex coronary artery; PTCA, Percutaneous transluminal coronary angioplasty; RCA, Right coronary artery.*

recorded on video-tape and analysis was performed off-line by the new quantitative ultrasound analysis system, using a digitization frame rate of 10 images/s. Thus, 20-mm long coronary artery segments were

reconstructed and measured, utilizing the maximum memory capacity of the system, which is currently 200 images.

### 2.3 The quantitative intracoronary ultrasound analysis system

The analysis program utilizes the Microsoft Windows™ operating system on a Pentium (60 MHz) personal computer with 16 Mbytes of internal RAM. A framegrabber is installed (DT-3852; resolution: 800 x 600 x 8 bits), digitizing a user-defined region of interest from the video images. A maximum of 200 ICUS images can be digitized at a user-defined digitization frame rate (maximum: 20/s). The reconstructed segment length is thus defined by the speed of the motorized pull-back during the basic image acquisition and by the digitization frame rate. In the present study a pull-back speed of 1.0-mm/s and a digitization frame rate of 8 images/s (in vitro) and 10 images/s (in vivo) were used, resulting in a reconstructed segment length of 25 and 20 mm respectively. The pixel size, which depends on the magnification applied by the basic ICUS imaging system, ranged from 26  $\mu\text{m}$  to 36  $\mu\text{m}$ .

Minimum cost algorithm: The semi-automated contour detection of the intimal leading edge and the external boundary of the total vessel is based on the application of a minimum cost algorithm, previously applied [11] and described [12] in cross-sectional ICUS images. By this approach the digitized ICUS images are resampled according to a radial image reconstruction (64 radii in the cross-sectional images; 200 rows in the longitudinal sections). A cost matrix that represents the edge strength is calculated from the image data. For the detection of the boundary between lumen and plaque the cost value is defined by the spatial first-derivative. In order to detect the external boundary of the total vessel a pattern matching process by cross-correlation is adopted for the cost calculations. Through the cost matrices a path with the smallest accumulated value is determined by dynamic programming techniques [11].

Semi-automated contour detection: In order to obtain the contour detection of the intimal leading edge and the external boundary of the total vessel three sequential steps have to be performed, since the system is based on the concept that edge points, derived from previously detected longitudinal contours, guide and facilitate the final contour detection in the cross-sectional ICUS images.

First, a sequence of digitized ICUS images obtained from the motorized pull-back of the ultrasound transducer is stored in a voxel space [13]. Ring-down artifacts around the ICUS catheter, potentially interfering with the contour detection step, can be removed from all the ICUS images using an automated function. Two perpendicular cut planes running longitudinally along the long axis of the artery are used to reconstruct two longitudinal sections (Fig. 2). This longitudinal reconstruction step utilizes the ICUS

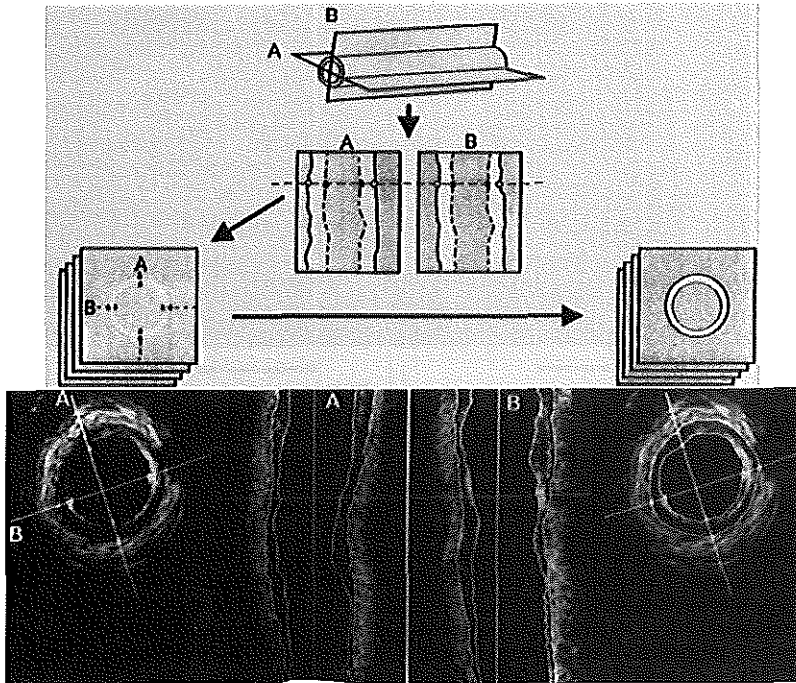


*Fig. 2. Morphometric analysis by contour detection in three-dimensional intracoronary ultrasound. With this method, edge points derived from longitudinal contours previously detected on two longitudinally reconstructed images guide and facilitate the final contour detection on the transverse ICUS images. ICUS images, obtained during a motorized pull-back, are stored in a voxel space. Two perpendicular cut planes (A and B) that are interactively placed are used to reconstruct two longitudinal sections from ICUS image data located at the intersections. Automated contour detection is performed in these longitudinal sections on the basis of application of minimum-cost algorithm. User then is free to set some markers on the longitudinal images to force the contours to pass through these sites, and optimal path is redefined by dynamic programming techniques. Longitudinal contours are updated during the entire interactive procedure and represented as individual edge points in the transverse images; these points guide the contour detection on the basis of application of minimum cost algorithm. Position of an individual transverse plane in the longitudinal sections is indicated by a horizontal cursor line, which can be used to scroll through the whole series of transverse images. The detected contours are finally checked in all the transverse images and manual correction of the contours can be performed.*

image data, located at the intersection of the cut planes with the voxel space. The position and the rotation angle of the two cut planes can be interactively changed by the user in order to obtain an optimal representation of the reconstructed coronary segment

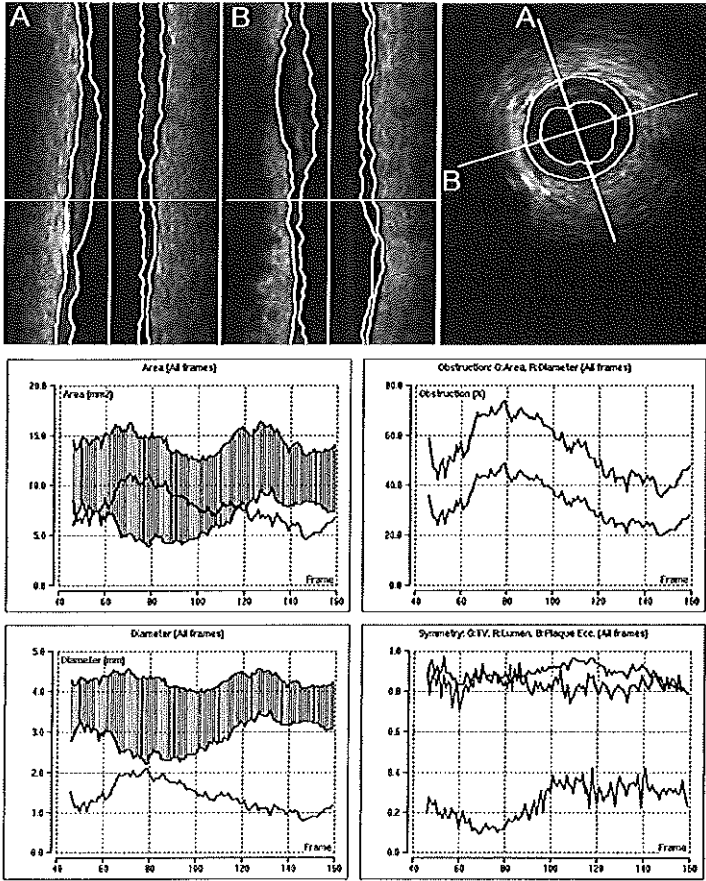


*Fig. 3. Standard display of the results. This clinical example shows the results of a quantitative analysis performed at 6-month follow-up after directional coronary atherectomy performed in a proximal left anterior descending coronary artery. The intimal leading edge and external vessel contours are shown in two longitudinally reconstructed sections (A and B, left and mid top), which stand perpendicular to each other as demonstrated in the transverse image (right top). Left middle and left bottom, Area and mean diameter measurements of lumen, total vessel, and plaque. Gray areas represent coronary plaque, and site of maximal plaque burden can thus be easily identified. Absolute value of plaque dimension is given as single function in display of area and in diameter measurements. Right middle, Functions of relative diameter obstruction and area obstruction. Right bottom, Symmetric ratios of both lumen and plaque.*

in the longitudinal sections. Secondly, the longitudinal contours are detected in these two longitudinal images. A first boundary detection is performed automatically, based on the application of the minimum cost algorithm. Then the user is free to set some

markers in the longitudinal images that force the contours to pass through these sites. This is achieved by setting the cost matrix of the manually defined sites at a very low value. Using dynamic programming techniques, the optimal path is then redefined for the modified cost matrix. During the entire user interactive procedure the longitudinal contours are visible and updated in the longitudinal sections. In the transverse images the longitudinal contours intersecting this plane are represented as points. These individual edge points guide the final contour detection in the transverse images by defining center and range of the boundary searching process, based on the application of the minimum cost algorithm. The position of an individual transverse plane in the longitudinal sections is indicated by a horizontal cursor line which can be used to scroll through the whole series of transverse images. The detected contours are checked by the analyst in all the transverse images and manual correction of the contours can be performed.

Calculation and display of results: The quantitative results including diameter and area measurements of lumen, total vessel and plaque as well as %-diameter-obstruction and %-area-obstruction are displayed (Fig. 3). Plaque area is calculated by subtracting the lumen area from the total vessel area, thus representing the plaque-media complex. Volumes of lumen, total vessel or plaque are calculated as:

$$V = \sum_{i=1}^n A_i * H$$

with V = volume, A = area of lumen, total vessel or plaque in a certain digitized cross-sectional ultrasound image; H = thickness of the coronary artery slice, which is represented by this digital cross-sectional ICUS image, n = number of digitized cross-sectional images encompassing the volume to be measured.

Mean values, standard deviations, minimum and maximum values of area and volume measurements are presented. The data of the current transverse image are constantly displayed and serially updated if manual corrections of the contours are performed. The analyzed artery segment can be three-dimensionally displayed using a cylindrical format; this is, however, not required for the quantification process utilizing the three-dimensional data set (Fig. 8).

## 2.4 Data analysis

At the transition between two phantom segments the circular contours of both adjacent segments are simultaneously visualized by ICUS, due to the limited out-of-plane resolution of the current ultrasound transducers [14]. Withdrawing the ultrasound transducer from the segment with the smaller dimension to the segment with the larger

dimension, the transition to the latter segment was defined as the first image in which the contour of the larger segment expressed a higher intensity than the contour of the smaller segment. This definition was used in order to calculate the volumes of the phantom segments. For the validation of the area measurements images from the mid-portion of each segment were used.

The in vitro experiments of the present study were performed in water, while ICUS imaging systems are calibrated for application in blood. Accordingly, a correction factor (0.953) based on the different velocities of ultrasound in blood (1570 m/s) and water (1497 m/s) [15] was applied.

The same digitized in vivo ICUS images were analyzed off-line by two independent observers who previously had common training in using the semi-automated contour detection system. After 2-3 weeks the analysis was repeated by the blinded first observer. Repeated measurements by the same observer (Ia and Ib) and measurements of two independent observers (Ia and II) were studied in order to obtain information on the intraobserver and interobserver variability of the new semi-automated analysis method.

## 2.5 Statistical analysis

Results are given as mean  $\pm$  SD. Mean difference and SD of the differences were calculated for each phantom segment (ICUS measurements – true phantom dimensions) and for repeated measurements by the same observer as well as by two different observers [16]. Analysis of variance and linear regression analysis were performed in order to compare the measurements of the intraobserver as well as the results of the interobserver study.

## 3 RESULTS

### 3.1 Phantom study in vitro

The lumen area measurements were compared with the true values using linear regression analysis. The measurements ( $n = 600$ ) and true phantom values showed a high correlation ( $r = 0.99$ ;  $y = 0.99x + 0.11$ ;  $SEE = 0.12 \text{ mm}^2$ ). The mean difference between measurements and true phantom areas ranged from -0.65 to 1.24% with the exception of the smallest segment, in which a small overestimation (3.86%) was found. Correlation between the volume measurements ( $n = 20$ ) and the true phantom volumes was high ( $r = 0.99$ ;  $y = 1.02x - 0.42$ ;  $SEE = 1.17 \text{ mm}^3$ ). The measured volumes showed a slight overestimation with a mean difference ranging from 0.25% to 1.72%. A decrease in phantom dimensions was associated with a slight increase in the relative SD

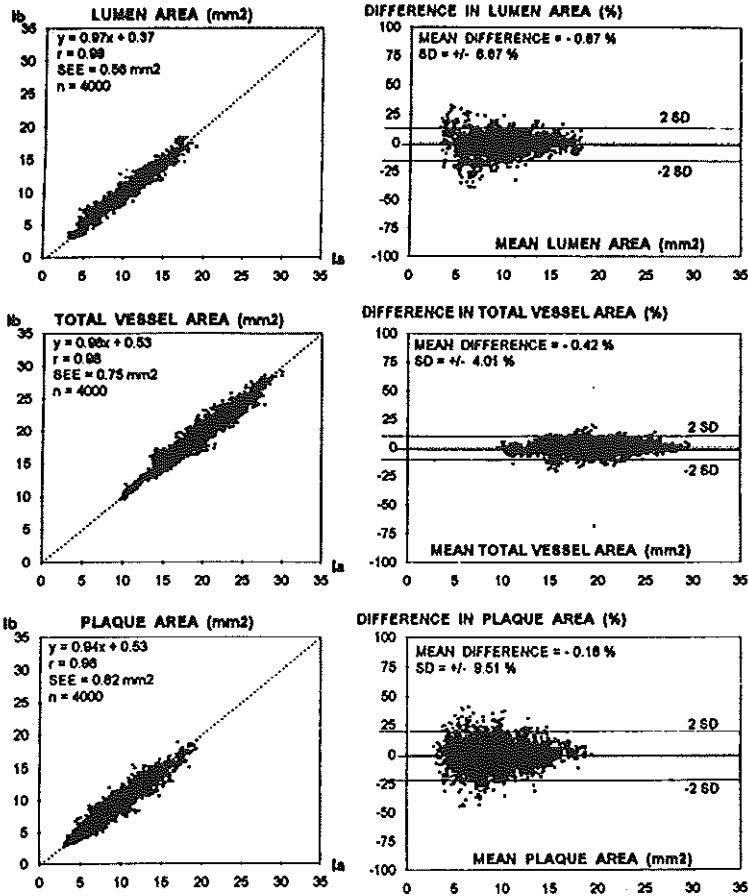


Fig. 4. Intraobserver variability of area measurements *in vivo*. Left, Results of the linear regression analyses comparing lumen, total vessel and plaque measurements of the first (Ia) and the second (Ib) observations. Right, Relative intraobserver differences plotted against the mean of two measurements. Continuous lines, Relative mean signed difference and 2 SD; dotted line, line of identity.

of the difference of area and volume measurements (0.56, 0.95, 0.95 and 2.55% for area and 1.40, 2.69, 2.78, and 3.75% for volume measurements in the segments with lumen diameters of 5, 4, 3, and 2 mm respectively).

### 3.2 Area measurement *in vivo*

The time required for the complete analysis was  $1.15 \pm 0.31$  hours. The correlation of repeated area measurements of coronary lumen, total vessel, and plaque was high with correlation coefficients of 0.98, 0.98, and 0.96 respectively (Fig. 4, left panels). The

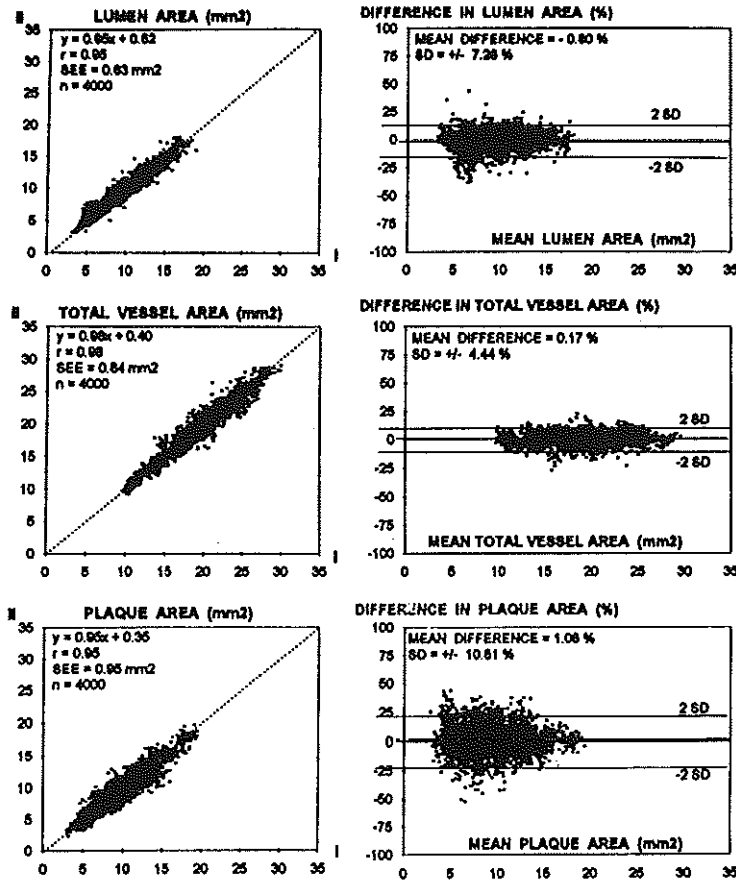


Fig. 5. Interobserver variability of area measurements in vivo. Left, Results of the linear regression analyses comparing lumen, total vessel and plaque measurements of the first (Ia) and the second (II) observers. Right, Relative interobserver differences plotted against the mean of two measurements. Continuous lines, Relative mean signed difference and 2 SD; dotted line, line of identity.

mean relative differences between repeated area measurements by the same observer were < 1% for lumen, total vessel and plaque area (Fig. 4, right panels). The SD of the differences was higher for the plaque area than for lumen and total vessel area (9.51% vs. 6.67% and 4.01%, respectively). The interobserver correlation coefficients were high (0.95, 0.98, 0.95 for lumen, total vessel, and plaque) (Fig. 5, left panels), but for lumen and plaque area measurements they were slightly lower than the corresponding intraobserver correlation coefficients. The interobserver SEEs of lumen, total vessel, and plaque areas (0.63, 0.84, and 0.95 mm<sup>2</sup> respectively) were also higher than the corresponding intraobserver SEE. The SD of the relative differences was slightly higher



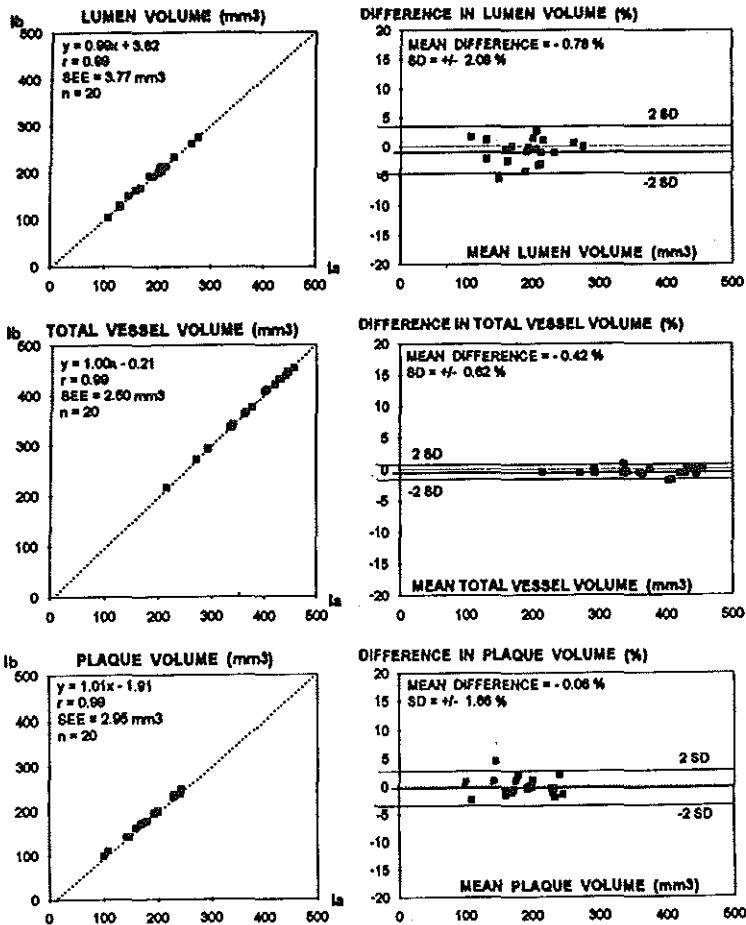


Fig. 6. Intraobserver variability of volume measurements in vivo. Left, Results of the linear regression analyses comparing lumen, total vessel and plaque measurements of the first (Ia) and the second (Ib) observations. Right, Relative intraobserver differences plotted against the mean of two measurements. Continuous lines, Relative mean signed difference and 2 SD; dotted line, line of identity.

for interobserver differences (Fig. 5, right panels) than intraobserver differences. The data-points for smaller dimensions of lumen and plaque areas showed a larger relative dispersion.

### 3.3 Volume measurement in vivo

The results of the lumen, total vessel, and plaque volume measurements are shown in Table II. A high correlation between the intraobserver measurements was found with a correlation coefficient of 0.99 for coronary lumen, total vessel, and plaque (Fig. 6, left

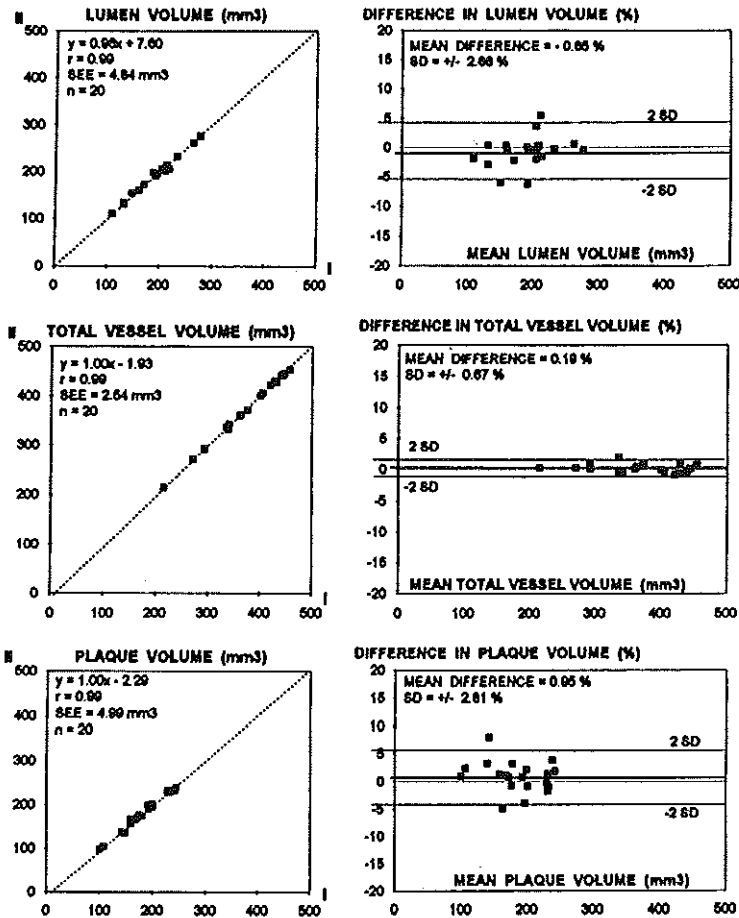


Fig. 7. Interobserver variability of volume measurements in vivo. Left, Results of the linear regression analyses comparing lumen, total vessel and plaque measurements of the first (Ia) and the second (Ib) observers. Right, Relative interobserver differences plotted against the mean of two measurements. Continuous lines, Relative mean signed difference and 2 SD; dotted line, line of identity.

panels). The correlation coefficients were also high for the comparison of the measurements of two independent observers (0.99 for lumen, total vessel, and plaque volumes) (Fig. 7, left panels). The SEE and the SD of the differences were higher for the interobserver than the intraobserver comparison (Fig. 6 and 7, right panels).

#### 4 DISCUSSION

The application of high-frequency ICUS permits the visualization (Fig. 8) and quantification of coronary artery atherosclerosis [21-24] and the assessment of catheter-

**Table II.** Coronary artery lumen, total vessel, and plaque volume in vivo: Results of the intraobserver and interobserver studies

| Patient | Lumen (mm <sup>3</sup> ) |       |       | Total vessel (mm <sup>3</sup> ) |       |       | Plaque (mm <sup>3</sup> ) |       |       |
|---------|--------------------------|-------|-------|---------------------------------|-------|-------|---------------------------|-------|-------|
|         | Ia                       | Ib    | II    | La                              | Ib    | II    | Ia                        | Ib    | II    |
| 1       | 158.8                    | 159.0 | 157.8 | 338.9                           | 336.0 | 832.6 | 180.6                     | 177.0 | 174.8 |
| 2       | 185.5                    | 193.4 | 197.6 | 427.9                           | 480.7 | 430.6 | 242.4                     | 237.3 | 288.0 |
| 3       | 159.5                    | 168.4 | 160.1 | 385.8                           | 387.4 | 337.1 | 175.8                     | 174.0 | 177.0 |
| 4       | 208.4                    | 203.0 | 207.7 | 439.9                           | 439.0 | 441.3 | 231.5                     | 236.0 | 288.6 |
| 5       | 207.8                    | 214.1 | 200.8 | 400.5                           | 407.9 | 400.6 | 192.7                     | 198.8 | 200.3 |
| 6       | 202.0                    | 199.2 | 206.0 | 446.2                           | 447.2 | 445.4 | 244.2                     | 248.0 | 289.4 |
| 7       | 204.8                    | 211.3 | 204.3 | 404.9                           | 411.8 | 406.1 | 200.1                     | 200.5 | 201.8 |
| 8       | 216.6                    | 214.2 | 204.9 | 375.8                           | 376.0 | 372.1 | 159.2                     | 161.8 | 167.2 |
| 9       | 231.1                    | 238.5 | 281.7 | 431.6                           | 431.8 | 427.7 | 200.5                     | 198.2 | 196.0 |
| 10      | 262.7                    | 261.0 | 261.0 | 456.3                           | 454.8 | 452.9 | 193.6                     | 193.7 | 191.9 |
| 11      | 145.2                    | 158.5 | 154.1 | 292.8                           | 294.6 | 290.8 | 147.6                     | 141.2 | 136.2 |
| 12      | 168.7                    | 168.6 | 172.4 | 341.0                           | 342.2 | 348.2 | 172.3                     | 173.6 | 170.8 |
| 13      | 129.0                    | 131.8 | 182.9 | 271.1                           | 272.6 | 270.4 | 142.1                     | 140.8 | 137.5 |
| 14      | 130.8                    | 129.3 | 180.8 | 360.5                           | 362.3 | 360.5 | 229.7                     | 238.0 | 230.2 |
| 15      | 107.6                    | 105.8 | 109.6 | 215.4                           | 216.2 | 214.8 | 107.8                     | 110.4 | 105.2 |
| 16      | 211.2                    | 213.4 | 214.4 | 444.0                           | 447.2 | 443.8 | 282.8                     | 233.8 | 229.4 |
| 17      | 190.2                    | 191.8 | 190.4 | 419.2                           | 421.8 | 422.8 | 229.0                     | 230.0 | 282.8 |
| 18      | 204.4                    | 205.2 | 205.0 | 368.8                           | 366.6 | 362.2 | 159.4                     | 161.4 | 157.2 |
| 19      | 193.0                    | 193.4 | 193.6 | 298.2                           | 292.8 | 292.8 | 100.2                     | 99.4  | 99.2  |
| 20      | 275.2                    | 275.2 | 276.2 | 448.6                           | 445.6 | 442.6 | 168.4                     | 170.4 | 166.4 |
| Mean    | 189.6                    | 191.0 | 190.5 | 375.1                           | 376.7 | 374.5 | 185.5                     | 185.7 | 184.0 |
| SD      | 42.9                     | 42.6  | 41.7  | 68.4                            | 68.8  | 68.7  | 42.3                      | 42.9  | 42.8  |

I, First observer (a, first observation; b, second observation); II, second observer.

based interventions [17-20]. Serial ICUS studies also permit the assessment of progression/regression of atherosclerosis as well as the mechanisms of coronary restenosis [25].

The main limitation in the comparison of serial ultrasound studies is the virtual impossibility of examining exactly the same ultrasonic cross-section. In previous studies, anatomic landmarks such as side-branches or deep calcifications were used to define corresponding images in serial studies. The application of the proposed analysis system offers a more reliable solution to this problem, as a long arterial segment can be examined. Minimal differences in the start- and end-point of repeated studies are unlikely to impair the accuracy of the changes in lumen and plaque volume measurements, assessed for an entire arterial segment. Since the aim of this study was to determine the accuracy and reproducibility of the analysis method, the same set of digitized images from a single pull-back per patient was used for repeated analysis.

The results of the in vitro study suggest that the semi-automated analysis system operates accurately and a high reproducibility in vivo was demonstrated. The SDs of the

intra- and interobserver differences in detecting the total vessel contours were particularly low, reflecting the regular shape of the external boundary of the total vessel. The lumen contours, however, demonstrated a slightly higher variability which can be explained by irregularities of the shape of the luminal area, especially after coronary interventions. The larger variability of plaque area measurements, derived from measurements of both lumen and total vessel contours, reflects the combined variability of these two contours. The volumetric measurements in vivo showed a lower SD of the differences compared to the area measurements, reflecting an averaging of the differences of the area measurements.

The ability to display the cross-sectional plus two longitudinal views simultaneously facilitates the detection of the boundary of the vessel. The reason for first performing a contour detection step on the longitudinal images is that the edge information obtained from this is subsequently used to guide the final contour detection on the transverse images.

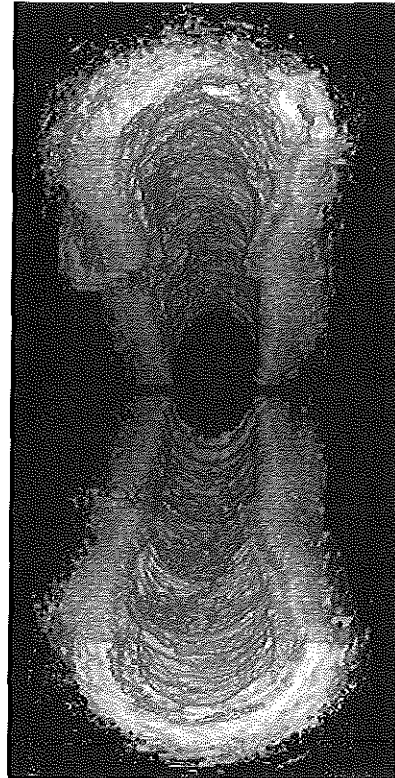


*Fig. 8. Three-dimensional display of a coronary segment at follow-up after directional coronary atherectomy. This display uses a cylindrical format; it is not required for the quantification based on the three-dimensional data set. Nevertheless, it may provide additional insight into plaque geometric features.*

#### 4.1 Previous studies

A different approach of contour detection, providing (semi-) automated tracking of coronary wall and lumen in ICUS image sequences, has been developed by Sonka et al. [26]. The border tracking is performed only in the cross-sectional images without the assistance of an additional contour detection step in longitudinally reconstructed images. The feasibility of this system in analyzing in vivo examinations remains to be confirmed since the movement of the ICUS catheter or the poor depiction of the plaque

in single ICUS images may impair the application of this algorithm, but the first results in vascular specimen *in vitro* are promising.

Data on variability and reproducibility of ICUS measurements are limited to the assessment of selected individual cross-sections in both *in vitro* and *in vivo* studies, generally addressing different questions. A systematic study [5] on the variability of measurements in 120 cross-sectional ICUS images *in vivo* has recently been published, demonstrating a relatively high variability of the manual contour tracing [27]. In agreement with the present study the SD of the differences was higher for plaque than for vessel lumen or total area measurement, but the variability of repeated manual contour tracing [5] was indeed higher than the variability of the proposed analysis system in the present study. This may be partially explained by the use of larger ultrasound catheters that show strut artifacts, obscuring a portion of the vessel wall, and the use of single digitized frames without the option of scrolling the video tape back or forth.

Limited information about the reproducibility of volumetric measurements is available and it is difficult to compare results provided by different quantitative analysis systems. Matar and colleagues recently reported an intraobserver study with a correlation coefficient of 0.98 for automated threshold-based measurement of lumen volume *in vivo* [28] confirming the high reproducibility of volumetric measurement observed in the present study.

#### **4.2 Approaches towards volumetric quantification**

Three-dimensional ICUS was first used clinically to visually assess the spatial configuration of plaques [29]. The morphology of dissections [30, 31] and stents [32, 33] was examined and their length or diameter was measured. However, the three-dimensional data set can also be processed to quantify lumen and/or plaque volumes which can be achieved by different technical approaches. These systems differ in terms of image segmentation, the algorithm for identification of the structures of interest in the digitized ICUS images. Distinction between vessel lumen and wall can be achieved by different (semi-)automated systems on-line with binary threshold-based algorithms [28, 29], voxel-based segmentation algorithms [34], or algorithms for statistical pattern recognition [6]. The applicability of these approaches depends considerably on the image quality and is restricted to the automated detection of the intimal leading edge. The proposed quantitative analysis system, however, combines automated contour detection and user interaction and is therefore able to partly compensate for limitations of the ICUS image quality. The system is qualified to identify not only the intimal

leading edge, but also the external contour of the vessel, thus permitting the semi-automated quantification of plaque volume.

The possibility to examine the vascular segment at the same time in a transverse and two longitudinal views and the concept of applying a semi-automated contour detection in the cross-sectional ICUS images, guided by edge points derived from previously detected longitudinal contours, are the key factors explaining the high reproducibility of this ICUS analysis method *in vivo*.

Contradictory results have been observed in previous progression/regression trials using quantitative coronary angiography. ICUS directly visualizes the vessel wall and may therefore better reflect the changes of the plaque, but in progression/regression studies small changes can be expected despite the long study period and a high reproducibility of measurements is important. On the Basis of the results of the present study, which demonstrates a high reproducibility of the volumetric ICUS measurement, volumetric ICUS measures may be considered [35].

### **4.3 Limitations**

Behind deposits of calcium the external vessel boundary cannot be traced and, depending on the type of stent, the metallic struts may occasionally render the external contour detection difficult. The proposed analysis system, however, allows reliable interpolation between preceding and following images on the longitudinal sections. The edge information finally permits a reproducible interpolated contour tracing on the cross-sectional ICUS images. Artifacts in the longitudinally reconstructed views, caused by the movement of the ultrasound catheter during the cardiac cycle and the systolic-diastolic changes in vessel dimensions [6, 8], may in the future be avoided by an ECG-gated [36, 37] ICUS image acquisition or even the combination of ECG-gated ICUS and angiographic data [38, 39]. Application of these combined approaches is still restricted, but the analysis system used in the present study is now used clinically for on-line and off-line analysis, and evaluation of tape-recorded ultrasound studies from multi-center trials has recently been started.

## **5 CONCLUSION**

The proposed analysis system provided accurate measurements of phantom dimensions and can be used to perform highly reproducible area and volume measurements in three-dimensional ICUS *in vivo*.

## 6 REFERENCES

1. Yock PG, Linker DT. Intravascular ultrasound. Looking below the surface of vascular disease. *Circulation* 1990;81:1715-1718.
2. Nissen SE, Gurley JC, Grines CL, Booth DC, McClure R, Berk M, Fischer C, DeMaria AN. Intravascular ultrasound assessment of lumen size and wall morphology in normal subjects and patients with coronary artery disease. *Circulation* 1991;84:1087-1099.
3. Keane D, Serruys PW. Quantitative coronary angiography: an integral component of interventional cardiology. In: Topol EJ, Serruys PW, eds. *Current Review of Interventional Cardiology* (2. ed). Philadelphia: Current Medicine, 1995;205-233.
4. von Birgelen C, Umans V, Di Mario C, Keane D, Gil R, Prati F, de Feyter PJ, Serruys PW. Mechanism of high-speed rotational atherectomy and adjunctive balloon angioplasty revisited by quantitative coronary angiography: edge detection versus videodensitometry. *Am Heart J* 1995; 130:405-12.
5. Hausmann D, Lundkvist AJS, Friedrich GJ, Mullen WL, Fitzgerald PJ, Yock PG. Intracoronary ultrasound imaging: intraobserver and interobserver variability of morphometric measurements. *Am Heart J* 1994;128:674-680.
6. Di Mario C, von Birgelen C, Prati F, Soni B, Li W, Bruining N, de Jagere PJ, de Feyter PJ, Serruys PW, Roelandt JRTC. Three-dimensional reconstruction of two-dimensional intracoronary ultrasound: clinical or research tool? *Br Heart J* 1995;73(Suppl. 2):26-32.
7. von Birgelen C, Gil R, Ruygrok P, Prati F, Di Mario C, van der Giessen WJ, de Feyter PJ, Serruys PW. Optimized expansion of the Wallstent compared to the Palmaz-Schatz stent: On-line observations with intracoronary ultrasound after angiographic guidance. *Am Heart J* 1996; in press.
8. von Birgelen C, Kutryk MJB, Gil R, Ozaki Y, Di Mario C, Roelandt JRTC, et al. Quantification of the minimal luminal cross-sectional area after coronary stenting by two-dimensional and three-dimensional intravascular ultrasound versus edge detection and videodensitometry. *Am Heart J* 1996; in press.
9. Roelandt JRTC, Di Mario C, Pandian NG, Li W, Keane D, Slager CJ, de Feyter PJ, Serruys PW. Three-dimensional reconstruction of intracoronary ultrasound images: Rationale, approaches, problems, and directions. *Circulation* 1994;90:1044-1055.
10. Li W, von Birgelen C, Di Mario C, Boersma E, Gussenhoven EJ, van der Putten N, Bom N. Semi-automatic contour detection for volumetric quantification of intracoronary ultrasound. In: *Computers in Cardiology 1994*. Los Alamitos: IEEE Computer Society Press, 1994:277-280.
11. Di Mario C, The SHK, Madretsma S, van Suylen RJ, Wilson RA, Bom N, Serruys PW, Gussenhoven EJ, Roelandt JRTC. Detection and characterization of vascular lesions by

- intravascular ultrasound: an in vitro study correlated with histology. *J Am Soc Echocardiogr* 1992;5:135-146.
12. Li W, Bosch JG, Zhong Y, van Urk H, Gussenhoven EJ, Mastik F, van Egmond F, Rijsterborgh H, Reiber JHC, Bom N. Image segmentation and 3D reconstruction of intravascular ultrasound images. In: Wei Y, Gu B eds. *Acoustical Imaging Vol.20*. New York: Plenum Press, 1993:489-496.
  13. Kitney RI, Moura L, Straughan K. 3-D visualization of arterial structures using ultrasound and voxel modelling. *Int J Cardiac Imag* 1989;4:135-143.
  14. Benkeser PJ, Churchwell AL, Lee C, Abouelnasr DM. Resolution limitations in intravascular ultrasound imaging. *J Am Soc Echocardiogr* 1993;6:158-165.
  15. Hertz H. Principles of ultrasound in medical diagnosis. In: Bom N, ed. *Echocardiography with Doppler applications and real time imaging*. The Hague: Martinus Nijhoff Medical Division, 1977:7-14.
  16. Bland JM, Altman DG. Statistical methods for assessing agreement between two methods of clinical measurement. *Lancet* 1986; 2:307-310.
  17. Ge J, Erbel R, Gerber T, Gorge G, Koch L, Haude M, Meyer J. Intravascular ultrasound imaging in angiographically normal coronary arteries: a prospective study in vivo. *Br Heart J* 1994;71:572-578.
  18. Hodgson JMcB, Reddy KG, Suneja R, Nair RN, Lesnefsky EJ, Sheehan HM. Intracoronary ultrasound imaging: correlation of plaque morphology with angiography, clinical syndrome and procedural results in patients undergoing coronary angioplasty. *J Am Coll Cardiol* 1993;21:35-44.
  19. Losordo DW, Rosenfield K, Kaufman J, Pieczek A, Isner JM. Focal compensatory enlargement of human arteries in response to progressive atherosclerosis. In vivo documentation using intravascular ultrasound. *Circulation* 1994;89:2570-2577.
  20. St Goar FG, Pinto FJ, Alderman EL, Valentine HA, Schroeder JS, Gao SZ, Stinson EB, Popp RL. Intracoronary ultrasound in cardiac transplant recipients: in vivo evidence of "angiographically silent" intimal thickening. *Circulation* 1992;85:979-987.
  21. Mintz GS, Potkin BN, Keren G, Satler LF, Pichard AD, Kent KM, Popma JJ, Leon MB. Intravascular ultrasound evaluation of the effect of rotational atherectomy in obstructive atherosclerotic coronary artery disease. *Circulation* 1992;86:1383-1393.
  22. Nakamura S, Colombo A, Gaglione A, Almagor Y, Goldberg SL, Maiello L, Finci L, Tobis JM. Intracoronary ultrasound observations during stent implantation. *Circulation* 1994;89:2026-2034.
  23. Tenaglia AN, Buller CE, Kisslo KB, Stack RS, Davidson CJ. Mechanisms of balloon angioplasty and directional coronary atherectomy as assessed by intracoronary ultrasound. *J Am Coll Cardiol* 1992;20:685-691.



24. Tobis JM, Mallery JA, Gessert J, Griffith J, Mahon D, Bessen M, Moriuchi M, McLeay L, McRae M, Henry WL. Intravascular ultrasound cross-sectional arterial imaging before and after balloon angioplasty in vitro. *Circulation* 1989;80:873-882.
25. Di Mario C, Gil R, Camenzind E, Ozaki Y, von Birgelen C, Umans V, de Jagere P, de Feyter PJ, Roelandt JRTC, Serruys PW. Quantitative assessment with intracoronary ultrasound of the mechanisms of restenosis after percutaneous transluminal coronary angioplasty and directional coronary atherectomy. *Am J Cardiol* 1995;75:772-777.
26. Sonka M, Zhang X, Siebes M, DeJong S, McKay CR, Collins SM. Automated segmentation of coronary wall and plaque from intravascular ultrasound image sequences. In: *Computers in Cardiology 1994*. Los Alamitos: IEEE Computer Society Press, 1994:281-284.
27. Haase J, Ozaki Y, Di Mario C, Escaned J, De Feyter PJ, Roelandt JRTC, Serruys PW. Can intracoronary ultrasound correctly assess the luminal dimensions of coronary artery lesions? A comparison with quantitative angiography. *Eur Heart J* 1995;16:112-119.
28. Matar FA, Mintz GS, Douek P, Farb A, Virmani R, Saturnino PJ, Popma JJ, Pichard AD, Kent KM, Satler LF, Keller M, Leon MB. Coronary artery lumen volume measurement using three-dimensional intravascular ultrasound: validation of a new technique. *Cathet Cardiovasc Diagn* 1994;33:214-220.
29. Rosenfield K, Losordo DW, Ramaswamy K, Pastore JO, Langevin RE, Razvi S, Kosowsky BD, Isner JM. Three-dimensional reconstruction of human coronary and peripheral arteries from images recorded during two-dimensional intravascular ultrasound examination. *Circulation* 1991;84:1938-1956.
30. Cavaye DM, White RA, Lerman RD, Kopchok GE, Tabbara MR, Cormier F, French WJ. Usefulness of intravascular ultrasound imaging for detecting experimentally induced aortic dissection in dogs and for determining the effectiveness of endoluminal stenting. *Am J Cardiol* 1992;69:705-707.
31. Coy KM, Park JC, Fishbein MC, Laas T, Dianond GA, Adler L, Maurer G, Siegel RJ. In vitro validation of three-dimensional intravascular ultrasound for the evaluation of arterial injury after balloon angioplasty. *J Am Coll Cardiol* 1992;20:692-700.
32. Mintz GS, Pichard AD, Satler LF, Popma JJ, Kent KM, Leon MB. Three-dimensional intravascular ultrasonography: reconstruction of endovascular stents in vitro and in vivo. *J Clin Ultrasound* 1993;21:609-615.
33. Schryver TE, Popma JJ, Kent KM, Leon MB, Eldredge S, Mintz GS. Use of intracoronary ultrasound to identify the "true" coronary lumen in chronic coronary dissection treated with intracoronary stenting. *Am J Cardiol* 1992;69:1107-8.
34. Chandrasekaran K, Sehgal CM, Hsu TL, Young NA, D'Adamo AJ, Robb RA, Pandian NG. Three-dimensional volumetric ultrasound imaging of arterial pathology from two-dimensional intravascular ultrasound: an in vitro study. *Angiology* 1994;45:253-264.

35. von Birgelen C, Slager CJ, Di Mario C, de Feyter PJ, Serruys PW. Volumetric intracoronary ultrasound: a new maximum confidence approach for the quantitative assessment of progression-regression of atherosclerosis? *Atherosclerosis* 1996; in press.
36. Dhawale PJ, Wilson DL, Hodgson J McB. Optimal data acquisition for volumetric intracoronary ultrasound. *Cathet Cardiovasc Diagn* 1994;32:288-299.
37. Bruining N, von Birgelen C, Di Mario C, Prati F, Li W, Den Hood W, Patijn M, de Feyter PJ, Serruys PW, Roelandt JRTC. Dynamic three-dimensional reconstruction of ICUS images based on an ECG-gated pull-back device. In: *Computers in Cardiology 1995*. Los Alamitos: IEEE Computer Society Press, 1995:633-636.
38. Slager CJ, Laban M, von Birgelen C, Krams R, Oomen JAF, den Boer A, Li W, de Feyter PJ, Serruys PW, Roelandt JRTC. ANGUS: a new approach to three-dimensional reconstruction of geometry and orientation of coronary lumen and plaque by combined use of coronary angiography and IVUS (abstr). *J Am Coll Cardiol* 1995;25(Suppl.):144A.
39. Koch L, Kearney P, Erbel R, Roth T, Ge J, Brennecke R, et. al. Three dimensional reconstruction of intracoronary ultrasound images: roadmapping with simultaneous digitised coronary angiograms. In: *Computers in Cardiology 1993*. Los Alamitos: IEEE Computer Society Press, 1993:89-91.

## CHAPTER 6

---

# TEMPORAL AVERAGING FOR QUANTIFICATION OF LUMEN DIMENSIONS IN INTRAVASCULAR ULTRASOUND IMAGES

W. Li, E.J. Gussenhoven, Y. Zhong, S.H.K. The,  
H. Pieterman, H. van Urk, N. Bom.



## **ABSTRACT**

Quantitative analysis of arterial dimensions from high frequency intravascular ultrasound images (30 MHz) may be hampered by strong blood scattering. Replacement of blood by saline is one method to provide a clear view of the arterial lumen; another method is that of temporal averaging of successive ultrasound images. The accuracy of this latter method was tested by comparing the lumen area measurements on the temporal-averaged image with the data of the same cross-section obtained from the single-frame and saline-filled images. The mean lumen area measured on the temporal-averaged images was similar to that measured on the single-frame images (mean difference:  $-0.02 \pm 1.16 \text{ mm}^2$ ;  $p=\text{ns}$ ). The mean lumen area of the saline-filled images was 8% larger than the values obtained from the temporal-averaged and single-frame images (mean difference:  $-1.14 \pm 0.85 \text{ mm}^2$ ,  $p<0.05$ ), probably due to the difference in sound velocity between saline and blood. Intraobserver variations in the averaging method were 2.4 times smaller than the measurements of the single-frame images and close to the data obtained by saline injection (variation coefficient: single-frame: 8.8%; temporal-averaged: 3.6%; saline-filled: 2.9%). It is concluded that analysis from temporal-averaged images is more efficient, enabling accurate and reproducible measurement of the luminal dimensions from images containing blood scattering echoes. This technique is suitable to replace the laborious saline injection method that facilitates off-line quantitative analysis.

## **1 INTRODUCTION**

Intravascular ultrasonic imaging provides a direct and dynamic view of arterial vessels in the assessment of atherosclerotic diseases. The use of high frequency ultrasound is essential to achieve high resolution imaging of the arterial structures (Bom et al. 1989, Gussenhoven et al. 1989, Potkin et al. 1990). At high frequency, the echogenicity of blood increases rapidly due to the frequency dependency of blood scatters, reaching a similar level to that of the arterial tissues (Linker et al. 1991, Lockwood et al. 1991, Shung et al. 1988). The presence of strong blood scattering may mask the leading echoes from the arterial tissues, causing difficulty in discrimination of the luminal boundary. To solve this problem, saline may be injected during clinical examination in order to replace echogenic blood. Injection of saline is, however, time-consuming and generally considered as disadvantageous (Gussenhoven et al. 1991, The et al. 1992a, van Urk et al. 1991). Therefore, we developed a temporal averaging technique to facilitate quantitative off-line analysis of the free lumen area of those ultrasonic images containing blood scattering echoes inside the arterial lumen.

This study was designed to investigate the utility of the temporal averaging method for quantification of the luminal area by comparing measurements on the temporal-averaged

image with data from the single-frame image and saline-filled image of the same arterial site.

## **2 METHOD**

### **2.1 Intravascular ultrasound**

The intravascular ultrasound imaging system (Du-MED, Rotterdam, The Netherlands) used has a 30 MHz single-element transducer mounted on the tip of a 5F catheter. Cross-sectional images were scanned at a rate of 16 frames per second by fast rotation of the transducer with a drive shaft (1000 rpm). The system has a bandwidth of 20-40 MHz. Axial resolution of the system is 75  $\mu\text{m}$  and lateral resolution is better than 225  $\mu\text{m}$  at a depth of 2-4 mm. The ultrasonic scan was stored in a 512 x 512 x 8 bits digital memory and displayed with a standard video output via a real-time digital scan converter. Physiological signals such as electrocardiogram and blood pressure were simultaneously acquired and superimposed on the video output as a time reference for off-line analysis.

### **2.2 Patient study**

The intravascular ultrasound study was approved by the local committee on Human Research and informed consent was obtained from each patient. Intravascular ultrasound data were acquired from 18 patients (male/female:14/4, age:52-83 year) who underwent vascular intervention of the superficial femoral artery for disabling claudication. The echo catheter was advanced via a 7F sheath into the superficial femoral artery. A series of cross-sections was recorded during pull-back of the catheter. At each level of interest the catheter was kept in position for a period of time sufficient for recording (Gussenhoven et al. 1991, van Urk et al. 1991). If necessary, 5 cc of heparinized saline solution was injected manually through the introducer sheath to flush out the echogenic blood. The ultrasonic images were recorded on a standard VHS videotape for off-line analysis.

### **2.3 Temporal averaging**

Using real-time intravascular ultrasound it can be seen that the backscatter pattern of flowing blood varies over time, whereas echoes of arterial tissues present a more static pattern. This phenomenon facilitates differentiation of blood scattering from the echoes of the arterial wall on real-time intravascular ultrasound. The difference can be demonstrated by plotting the intensity profile at one angular position for all the images of one cardiac cycle (Fig. 1). Since the blood scattering changes with time, averaging a number of consecutive images over time may smooth out the scattering from blood while preserving the relatively stable structure of the arterial wall, and thus enhance the contrast at the

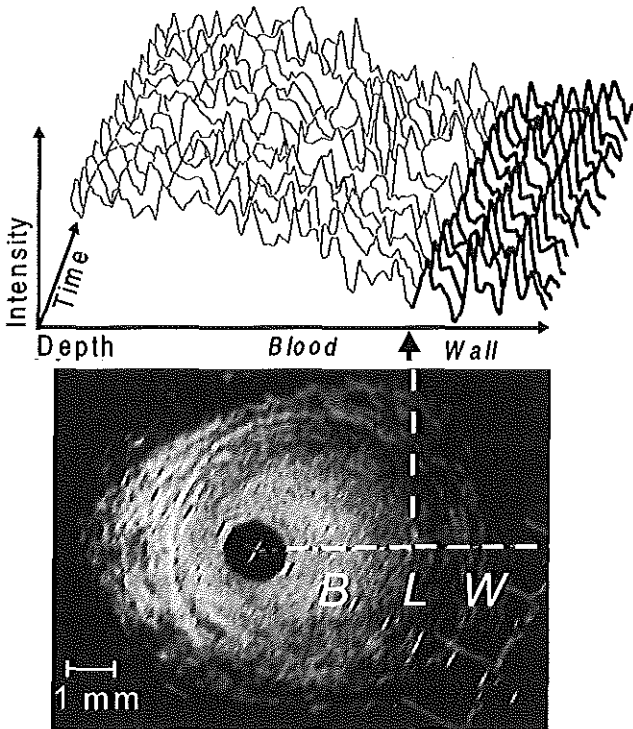


*Fig. 1. Plot of intensity profile during one cardiac cycle showing the random changes in backscatter pattern of blood echoes (B; thin line), while the profile of the arterial wall (W) presents a similar pattern during the cardiac cycle (thick line). Shown on the bottom image are the corresponding positions. The dotted horizontal line indicates the angular position at which the plot of the intensity profiles of blood and arterial wall is made. Note that on this intravascular ultrasound cross-section from the superficial femoral artery the presence of blood hampered visibility of the luminal interface (L).*

luminal interface on a still-frame image. Averaging is performed using the following formula:

$$I_{avg}(x,y) = (I_1(x,y) + I_2(x,y) + \dots + I_n(x,y))/n, \quad (1)$$

here  $I$  presents image intensity,  $n$  is the number of consecutive frames at the same cardiac cycle and  $x, y$  are image coordinates. This processing is able to cancel out the time-varying signals of blood scatterers and produce a homogeneous luminal region in the image.

Of major concern for this algorithm is the possible blurring effect caused by the motion of the wall or the catheter tip. During imaging of peripheral arteries the relative movement between the catheter and the wall is mainly produced by the wall compliance due to

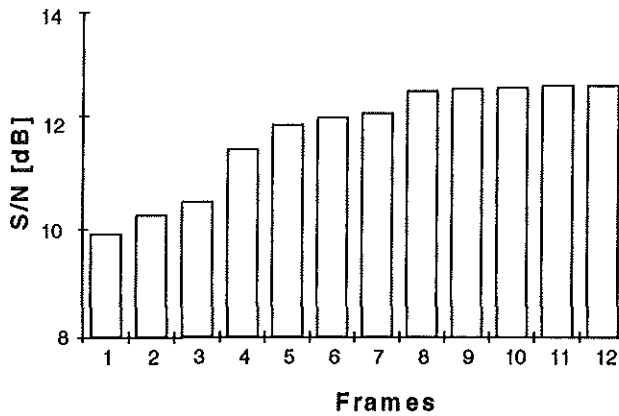


*Fig. 2. Values of signal-to-noise (S/N) ratio as a function of the number of the averaged frames calculated from the data shown in Fig. 1. Note the increase in the S/N ratio from frames 2 up to 8, and no change in the S/N ratio from frames 8 up to 12.*

pressure changes. As this wall motion is shown to be minimal in the diastolic period of the cardiac cycle, the blurring effect on the arterial structure can be minimized by selecting the diastolic frames for the averaging procedure (The et al. 1992b).

Theoretically, an averaging processing reduces the noise level of a signal by the square root of the times of average. Fig. 2 demonstrates the relationship between the improvement of the signal-to-noise (S/N) ratio and the number of frames to be averaged. The signal level is calculated by the mean intensity of the blood scattering; the noise level is defined as the standard deviation of the signal. It has been shown that the S/N ratio is improved with increase of the frame number. After averaging 8 frames there is no significant improvement observed. This is in agreement with our experience that averaging 4 to 8 diastolic frames (mean:  $N = 6$ ) produces satisfactory enhancement of the luminal boundary for the subsequent manual tracing (Fig. 3).

#### 2.4 Quantitative measurement

A computer analysis system based on an IBM compatible PC/AT was used for off-line analysis (Li et al. 1991, *Chapter 2*). The system was equipped with a DT 2851 framegrabber to convert video images into 512 X 512 X 8 bits digital format. The luminal contour was traced manually with a PC mouse. The absolute measure of the cross-sectional lumen area was calculated by converting the pixels into square millimetres with system calibration based on the sound velocity of blood.

Quantitative measurements were made from the intravascular images derived from 18 patients studied prior to or following vascular intervention. At each of 78 arterial sites selected, the free luminal area was measured on: the single-frame, the temporal-averaged



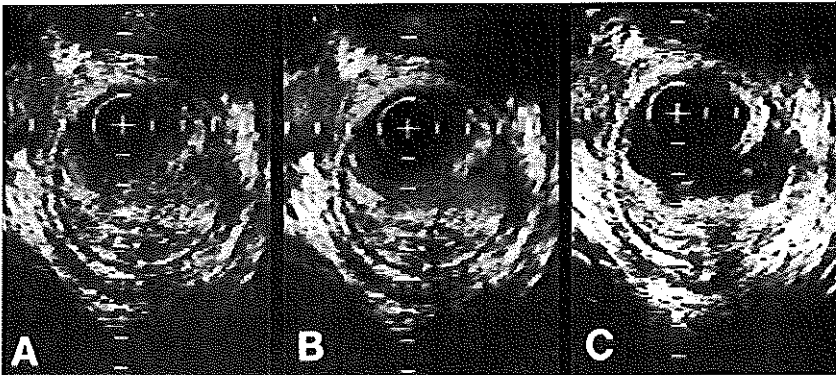


*Fig. 3. Three different presentations of an ultrasound cross-section from a superficial femoral artery (scale mark: 1 mm). A, the single-frame image containing the blood scattering; B, the temporal-averaged image and C, the image after saline injection. The visibility of the luminal structure is significantly improved on the temporal-averaged image and the saline-filled image, particularly the edge of the ruptured lesion that is difficult to recognize on the single-frame image.*

and the saline-filled images, respectively (Fig. 4). The single-frame image was selected from the first frame of the image sequence to be averaged. Real-time video images were reviewed to facilitate discrimination of the luminal interface from blood. To test the reproducibility of the three methods, measurements were repeated by the same observer two weeks later.

## 2.5 Data analysis

The three series of measurements are presented with the mean values and standard deviations (SD). Comparison of two measurements in each cross-section was performed by calculating the mean and SD of the paired differences. The significance of the difference of the mean values was determined by a paired t-test. A probability value of  $<0.05$  was considered statistically significant.

The degree of intra-observer variation is presented with a coefficient of variation defined as: (SD of the paired differences/mean value of the measurements) x 100 %.

## 3 RESULTS

The mean luminal areas measured on single-frame, temporal-averaged and saline-filled images were  $13.86 \pm 6.30 \text{ mm}^2$ ,  $13.88 \pm 6.15 \text{ mm}^2$  and  $15.00 \pm 6.76 \text{ mm}^2$ , respectively (Fig. 5). The mean difference between the temporal-averaged and single-frame images was minimal (paired difference:  $-0.02 \pm 1.16 \text{ mm}^2$ ,  $p=\text{ns}$ ). Comparing measurements from

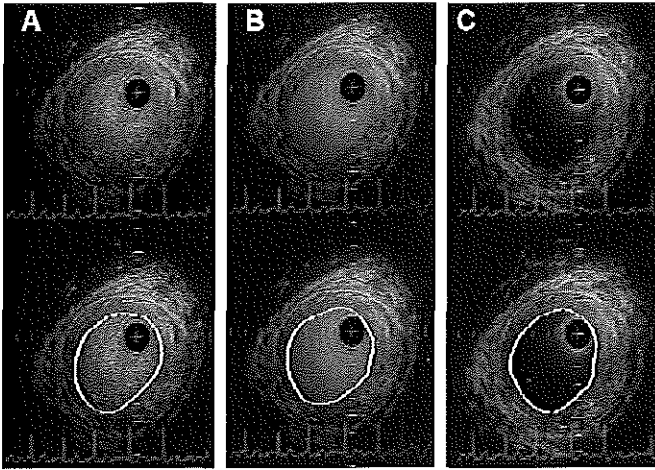


Fig. 4. Contour tracing of the free lumen area on the single-frame image (A), the temporal-averaged image (B) and the image with saline solution (C) (scale mark: 1 mm). A, the luminal contour has to be estimated by reviewing the real-time images. B, the temporal-averaging method allows direct tracing of the luminal contour. C, the use of saline solution enables a clear definition of the free lumen but introduces deviations in measurements due to the differences in sound velocity between blood and saline.

the temporal-averaged images with saline-filled images showed the mean value of the latter method to be 8% larger (paired difference:  $-1.14 \pm 0.85 \text{ mm}^2$ ,  $p < 0.05$ ).

The coefficient of intra-observer variation was 8.8% for data from single-frame images, 3.6% for data from temporal-averaged images and 2.9% for measurements on saline-filled images (Fig. 6).

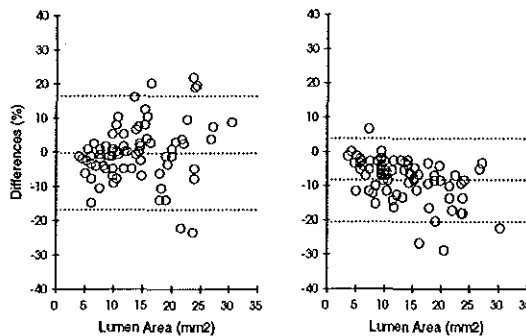


Fig. 5. The differences in the lumen area measurements obtained by the temporal averaging method and the single-frame images (left), and the saline-filled images (right). The 95% confidence interval is indicated by the upper and lower horizontal lines (mean  $\pm$  2SD).

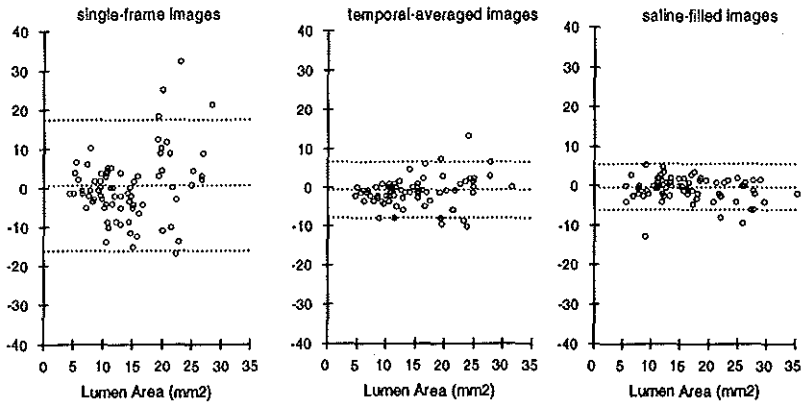


Fig. 6. Intra-observer variations for free lumen area ( $\text{mm}^2$ ) using three different methods. The 95% confidence interval is indicated by the upper and lower horizontal lines ( $\text{mean} \pm 2SD$ ).

#### 4 DISCUSSION

Intravascular ultrasound has shown promise as a safe and accurate imaging modality for detection of atherosclerosis as well as for the assessment of the outcome of vascular intervention (Gussenhoven et al. 1991, Nissen et al. 1990, Tobis et al. 1991, van Urk et al. 1991). The limitation encountered using high frequency ultrasound during off-line quantitative analysis of the free luminal area is the echogenicity of blood. In contrast, off-line quantitative analysis using the temporal averaging method permits a significant improvement in visualization of the luminal boundary on a still-frame image. Although the averaging procedure does not remove the echoes of blood scatterers, it generates a homogeneous luminal region by smoothing out the time-varying signals.

The results of this study show no differences in the mean measurements between the single-frame images and the data obtained by the averaging method. The mean lumen area measured on the saline-filled images was 8% larger than that of both the single-frame and the averaged images. One reason for this discrepancy may be the difference in ultrasound velocity between blood and saline. Saline solution has a lower ultrasound velocity than blood (saline: 1540 m/s versus blood: 1580 m/s at 37°C; a difference of 2.6%). Theoretically, a 2.6% change in sound velocity may produce an approximately 5.2% difference in area measurement of a circular lumen. In an in vitro setting, Moriuchi and coworkers (1990) found that the mean lumen area in saline increased 6%, compared with that in blood-filled images. Assuming that most of the intravascular ultrasound imaging systems are calibrated with the sound velocity in blood, the measurement of an image filled with saline solution will result in an overestimation of the vessel dimension.

The second factor that may lead to an increase of the luminal area during saline injection is the initial increase in the internal vascular pressure due to the injection.

In this study, the data obtained from a well-defined lumen during saline injection were used as a reference to test the reproducibility of the temporal averaging method. The measurement reproducibility using the averaging method was improved 2.4 times compared to that of single-frame images, and was similar to the results obtained from the saline-filled images (variation coefficient: single-frame: 8.8%, temporal-averaged image: 3.6%, saline-filled image: 2.9%). The higher intra-observer variation for measurements of single-frame images is due to the lack of a luminal contrast with the presence of blood scattering. One has to estimate the location of the contour by memorizing information from real-time video images; this procedure is time-consuming as the operator needs to review the video tape frequently.

Since the averaging procedure improves the signal-to-noise ratio, one may expect that measuring the averaged image would have a similar effect as the averaging of several individual measurements from the single-frame images. This means the variation coefficient will be reduced by the square root of the number of the measurements. Our results indicate that the improvement in measurement reproducibility by the averaging method is comparable to that of approximately six measurements of single-frame images. The temporal averaging method, however, is more efficient. The technique is easy to implement in an off-line system and requires a few seconds for the selection of frames to be processed.

Although the visibility of blood is considered as disadvantageous for off-line analysis, it should be emphasized that during real-time imaging, the arterial lumen can be differentiated by the characteristic changes in the blood scattering pattern. Particularly in the case of complex arterial dissections following balloon angioplasty, the visibility of blood may be helpful in assessing the anatomic substrate. The use of saline injection is mainly to facilitate off-line quantitative analysis.

## 5 CONCLUSION

This study has demonstrated the feasibility of using the temporal averaging method to enhance the luminal boundary of intravascular ultrasound images in the presence of strong interference of blood scatterers. The technique is able to reduce observer variation in single-frame images and produce a comparable performance as the saline flush method. Hence, the temporal averaging method, which provides an accurate and reproducible measure of the luminal dimensions in the presence of blood, may obviate the need of laborious saline injections during the catheterization procedure.

## 6 ACKNOWLEDGEMENT

The authors are indebted to H. Rijsterborgh for his comments.

## 7 REFERENCES

1. Bom N, ten Hoff H, Lancée CT, Gussenhoven EJ, Bosch JG. Early and recent intraluminal ultrasound devices. *Int J Cardiac Imag* 4:79-88; 1989.
2. Gussenhoven EJ, Essed CE, Lancée CT, Mastik F, Frietman P. Arterial wall characteristics determined by intravascular ultrasound imaging: An in-vitro study. *Am Coll Cardiol* 14:947-52; 1989.
3. Gussenhoven EJ, Frietman PAV, The SHK, van Suylen RJ, van Egmond FC. Assessment of medial thinning in atherosclerosis by intravascular ultrasound. *Am J Cardiol* 68: 1625-1632; 1991.
4. Li W, Gussenhoven WJ, Zhong Y, The SHK, Di Mario C. Validation of quantitative analysis of intravascular ultrasound images. *Int J Cardiac Imag* 6:247-253; 1991.
5. Linker DT, Kleven A, Grønningsæther Å, Yock PG, Angelsen A Bj. Tissue characterization with intra-arterial ultrasound: special promise and problems. *Int J Cardiac Imag* 6:255-263; 1991.
6. Lockwood GR, Ryan LK, Hunt JW, Foster FS. Measurement of the ultrasonic properties of vascular tissues and blood from 35-65 MHz. *Ultrasound in Med & Biol* 1:653-666; 1991.
7. Moriuchi M, Tobis JM, Mahon D, Gessert J, Griffith J. The reproducibility of intravascular ultrasound imaging in-vitro. *J Am Soc Echo* 3:444-50; 1990.
8. Nissen SE, Grines CL, Gurley JC. Application of a new phased-array ultrasound imaging catheter in the assessment of vascular dimensions. In-vivo comparison to cineangiography. *Circulation* 81:660; 1990.
9. Potkin BN, Bartorelli AL, Gessert JM, Neville RF, Almagor Y. Coronary artery imaging with intravascular ultrasound. *Circulation* 81:1575-85; 1990.
10. Shung KK, Yuan YW. Ultrasonic backscatter from flowing whole blood. II: Dependence on frequency and fibrinogen concentration. *J Acoust Soc Am* 84:1195-1200; 1988.
11. The SHK, Gussenhoven EJ, Zhong Y, Li W, van Egmond F. The effect of balloon angioplasty on the femoral artery evaluated with intravascular ultrasound imaging. *Circulation* 86:483-493; 1992a.
12. The SHK, Gussenhoven EJ, Li W, de Feyter P, Serruys PW. Intravascular ultrasonic assessment of lumen geometry and distensibility of the angiographically normal artery: A correlation with quantitative angiography. *Echocardiography* 9:133-139; 1992b.

13. Tobis JM, Mallery J, Mahon D, Lehmann K, Zaleski P. Intravascular ultrasound imaging of human coronary arteries in vivo. Analysis of tissue characterizations with comparison to in vitro histological specimens. *Circulation* 83:913-926; 1991.
14. Van Urk H, Gussenhoven EJ, Gerritsen GP, The SHK, van Egmond F. Assessment of arterial disease reconstructions by intravascular ultrasound. *Int J Cardiac Imag* 6:157-164; 1991.

## CHAPTER 7

---

# TEMPORAL CORRELATION OF BLOOD SCATTERING SIGNALS IN VIVO FROM RADIO FREQUENCY INTRAVASCULAR ULTRASOUND

W. Li, A.F.W. van der Steen, C.T. Lancee, J. Honkoop,  
E. J. Gussenhoven, N. Bom.





**ABSTRACT**

One limitation encountered using high frequency intravascular ultrasound (IVUS) is the echogenicity of blood which increases dramatically at frequencies of 20-40 MHz. Because of the higher velocity of moving blood particles, the echo pattern of flowing blood shows more variations in time than that of the wall. To investigate the time-varying characteristics of the blood scattering, measurements were performed on the RF data collected *in vivo* from 5 pig experiments. After positioning the echo catheter inside the iliac artery, an M-mode sequence of 30 RF traces was acquired at a high pulse repetition rate (5 kHz). The RF *correlation time* was measured on the regions of blood and the arterial wall. Two processing techniques, temporal averaging and correlation, were tested for suppression of the blood echo intensity.

The *correlation time*  $T_c$  measured in the blood region was approximately 1 ms which was shorter than that measured in the wall region ( $T_c \gg 6$  ms). The correlation values calculated in a small window showed a large variation in the blood region while the wall region produced a constant high output. After processing 8 consecutive RF traces ( $\Delta T = 200 \mu s$ ), the temporal averaging method results in a 50% intensity reduction in the blood region. Using the correlation output as a weighting function, the blood echo intensity can be further reduced to only 10% of its original value. Application of the RF correlation processing to a cross-sectional image data demonstrates the feasibility of this technique to remove most of the blood echoes and enhance the image contrast of the luminal interface.

**1 INTRODUCTION**

Intravascular Ultrasound (IVUS) is a real-time tomographic imaging modality which is being widely used in combination with various types of vascular intervention techniques (Bom et al. 1989; Nissen et al. 1991; Yock et al. 1993). The use of high frequency ultrasound (20-40 MHz) is a key element to achieve high resolution imaging of the arterial anatomy. One implication of using high ultrasonic frequencies is an increase of the blood echogenicity. The intensity of blood scattering may reach a level similar to that of the arterial tissue, leaving little contrast at the luminal interface. With real-time IVUS imaging, it can be seen that the scattering pattern of flowing blood varies over time, whereas echoes of the arterial tissue present themselves as a fixed pattern. This phenomenon allows identification of the blood echoes in real-time IVUS. Based on the changing characteristics of the blood scattering, we have demonstrated a temporal video averaging method to improve the image quality for off-line quantitative analysis (Li et al. 1992&1994, *Chapter 3&6*). A similar approach was also reported by Pasterkamp et al. (1993), whereby an image subtraction technique was applied for

enhancement the of the luminal contrast. These video processing techniques, although easy to implement, have two drawbacks. First, since the processing needs at least two video frames with a time interval of 20 ms, rapid wall motion may introduce blurring on the real-time image. Secondly, the image enhancement obtained by video processing is limited by the lack of phase information in the demodulated signals. As the phase shift in the radio-frequency (RF) signals is a sensitive index for motion detection (Bohs et al. 1991; de Jong et al. 1991; Hein et al. 1993; Ferrara et al. 1994), development of improved image processing methods is therefore directed towards processing of the original RF echo data. To evaluate the feasibility of RF signal processing techniques, the temporal characteristics of the blood scattering during IVUS imaging needs to be investigated. Gronningsaeter et al. (1995) have studied the effects of Doppler shift and frequency broadening respectively caused by the axial and lateral movements of blood particles in simulated data. An RF correlation detector for blood echo rejection was evaluated in vitro using water mixed with Sephadex particles in a tissue-like phantom (Gronningsaeter et al. 1994). The cyclic changes of blood echogenicity in IVUS video signals were reported by De Kroon et al. (1991). Several acoustic properties of blood and wall tissue were measured in vitro by Lockwood et al. (1991) at frequencies of 25-65 MHz. The backscatter level of flowing blood as a function of shear rate has been investigated at different frequency ranges by several groups (Yuan et al. 1988; De Kroon et al. 1993; Shung et al. 1993; Foster et al. 1994). Little information about the temporal properties of the RF blood scattering signals is available from an in vivo IVUS set-up, in which the ultrasound beam is always perpendicular to the direction of blood flow.

The purpose of this study was to investigate the temporal characteristics of the blood scattering in vivo. The measurements were made in animal experiments under normal flow conditions. Two processing techniques, temporal averaging and correlation, were tested on the collected RF data.

## **2 MATERIALS AND METHODS**

### **2.1 Experimental set-up**

This study was performed in vivo in the iliac artery of Yorkshire pigs. Ultrasonic data were acquired using a 30 MHz IVUS imaging system (Du-MED, Rotterdam, The Netherlands) with a single-element transducer mounted on the tip of a 5F catheter. Cross-sectional images were scanned by means of a flexible drive shaft rotation. The bandwidth of the system was 20-40 MHz, yielding an axial resolution of approximately 75  $\mu\text{m}$ . During the experiments, the echo catheter was advanced through a 7F sheath

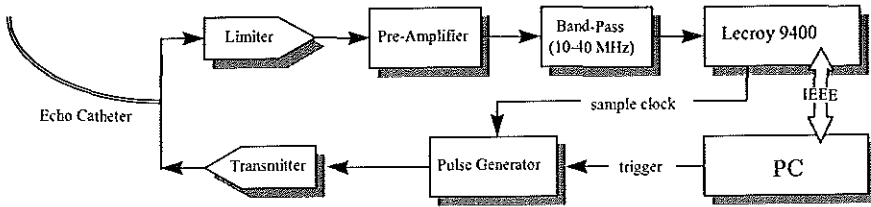


Fig. 1. Block diagram of the RF data acquisition set-up.

into the iliac artery. At the site of interest, a few seconds of cross-sectional IVUS images were first recorded on the video-tape as a reference. Keeping the catheter at the same position, the imaging system was then switched to M-mode. The orientation of the transducer was manipulated manually to select an angular position at which the scan line contained the echoes from both blood and the arterial wall.

## 2.2 Data acquisition

The RF data acquisition set-up is illustrated in Fig. 1. At each selected angular position, a burst of 30 ultrasound beams was transmitted. The pulse repetition rate was 5 kHz. Data acquisition was manually initialized at an arbitrary moment of the cardiac cycle. The received RF signal was amplified 40 dB by the amplifier of the imaging system and digitized by a dual channel digital oscilloscope (LeCroy 9400, Chestnut Ridge, NY, USA). The sampling was performed at a frequency of 200 MHz with 8 bits resolution. The sample duration of RF traces was 10 ms, yielding a scan depth of approximately 8 mm. To avoid jitter between RF traces, the pulse generator was synchronized with the internal sampling clock of the oscilloscope. The digital data were transferred to the host computer via an IEEE connection. The data acquisition procedure was controlled by a PC-486 with in-house developed software.

Measurements were performed in 5 pig experiments. In each experiment, three different angular positions were selected. RF signals were acquired 3 times at the same angle to obtain data from different phases of a cardiac cycle. A total of 45 measurements containing 1350 RF traces became available for further analysis.

## 2.3 Temporal correlation

A temporal correlation method was used to evaluate the changes in the RF trace sequence acquired from the same angle with a time interval of 200 ms. The correlation coefficient  $R(n)$  between the first RF trace  $S_1$  and the subsequent  $n$ th trace  $S_n$  was determined by the following formula:

$$R(n) = \frac{\sum_{i=1}^K [S_1(i) - \bar{S}_1][S_n(i) - \bar{S}_n]}{\sqrt{\sum_{i=1}^K [S_1(i) - \bar{S}_1]^2 \sum_{i=1}^K [S_n(i) - \bar{S}_n]^2}}, \quad n=2,3 \dots 30 \quad (1)$$

where  $n$  is the index of the RF trace,  $K$  is the number of data points in a correlation window and  $i$  is the index of the data points.  $\overline{S}_i$  and  $\overline{S}_n$  are the means of the RF data in the window. This procedure yielded a series of  $R$  values ranging from -1 to 1, representing the similarity between the RF trace arriving at  $T_i$  and that arriving at  $T_n = (n-1) * 200 \mu s$ .

**2.4 Data processing I: RF correlation measurements**

**Correlation curve in a region:** The 30 RF traces acquired at one angular position (indicated by a white line in Fig. 2, panel A) were peak-detected and displayed as an M-mode image. The motion of the blood particles was identified on the M-mode display (Fig. 2, panel C). The luminal region showed a random pattern plus some diagonal streaks produced by motion components parallel to the ultrasound beam. The echoes from the arterial tissue presented as a stationary pattern throughout the acquisition period (Fig. 2, panel B). Using this as a visual criterion, the RF traces were manually divided into two regions: blood and wall. The B-mode images recorded at the same catheter position were reviewed during the data processing. Anatomic structures such as the adjacent vein were identified to avoid improper selection of the region of interest. The time-varying characteristics of the RF signals were evaluated using the correlation method from these selected blood and vessel wall regions. For each region, the correlation coefficient was calculated using expression (1) where the parameter  $K$

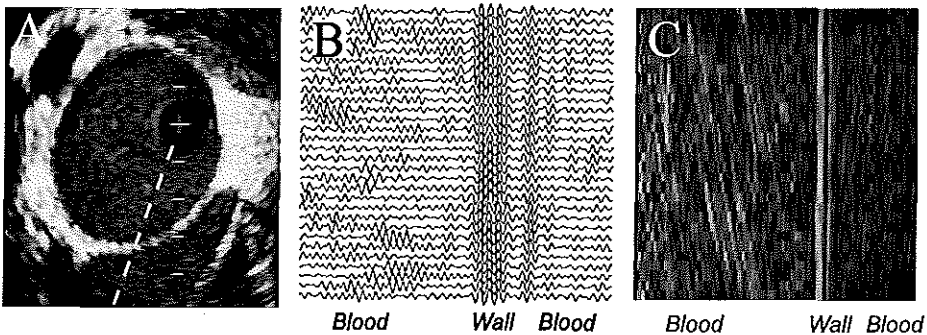


*Fig. 2. Illustration of RF data acquisition. A: an iliac cross-section obtained by the IVUS imaging system. B: RF sequence acquired at one angle. The angular position of the transducer is indicated by the white line in (A). C: corresponding M-mode display. The gray-scale on the M-mode image was log compressed. Note the changing structure of the blood region in contrast to a fixed pattern in the wall. The random and diagonal patterns were caused by the transverse and axial movements of blood particles, respectively.*

was set to the size of the region. The number of available data points ranged from 200 to 1000, depending on the lumen dimension for the blood region and the wall thickness for the tissue region. The correlation curves of the blood and wall regions were obtained from the mean values of the 45 regional measurements at each delay time. The point at which the correlation coefficient dropped to a value  $\leq 0.1$  in the curve was defined as the correlation time  $T_c$ .

**Correlation distribution in a window:** To investigate the possibilities of using correlation techniques for image enhancement, the behavior of the correlation procedure was studied in a small window. When formula (1) is applied to suppress the blood signals, the correlation output needed to have a time resolution comparable to that of the B-mode image. The window size  $K$  for the correlation calculation was set to 7 points to provide a sufficient resolution. The time period of the window was 35 ns and the length was 28  $\mu\text{m}$ . This window length was approximately one acoustic wavelength of the imaging system, which ensured no smearing of the image was introduced by the correlation procedure. After the region separation, the data were subdivided into a sequence of non-overlapping windows. A similar correlation process as described above was performed in the window data. The correlation output range (-1 ~ 1) was divided into 20 bin ranges with intervals of 0.1. For both the blood and tissue regions, distribution histograms at each delay time were calculated from the whole data set.

## 2.5 Data processing II: RF image processing

**Methods for image enhancement:** Two processing methods, temporal averaging and correlation, were tested on experimental data. The first method was to average a number of RF traces. Because of the randomness in the blood scattering signals, the averaging procedure was expected to reduce the signal amplitude. The second method was to use the correlation output as a weighting function to modulate the RF signals. Fig. 3 illustrates the correlation method by an example with a sequence of 8 RF traces. First, a number of RF traces was selected from the original RF traces (Panel A) and a temporal averaged RF trace was obtained (Panel B). Secondly, a moving window with a length of 7 points was defined along the depth axis of an RF trace. The interval between two adjacent windows was 3 points yielding 50% overlap. Third, a sequence of correlation values  $R$  was obtained at each window position using formula (1). From this sequence, the minimum value was selected as the weighting factor for that particular window position. A weighting curve was generated from all available window positions (Panel C); a high value in the weighting curve indicates no motion

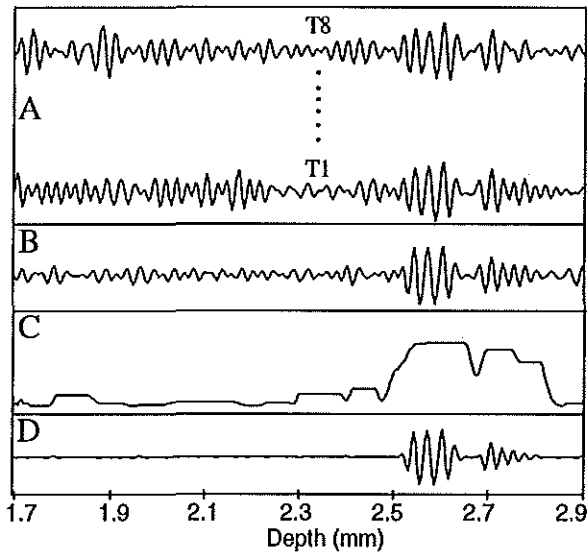


*Fig. 3. Example of RF processing from data obtained at one angle. A: an original RF sequence with 8 traces. B: averaged output of the RF sequence. C: weighting function derived by the correlation method. D: processed trace obtained by multiplying B and C.*

was detected, whereas a low value indicates changes had occurred within the acquisition time. Finally, the output signal was obtained by multiplying the averaged signal with its corresponding weighting factor (Panel D).

**Quantitative evaluation of the RF methods:** The effect of these methods was quantitatively evaluated by comparing the echo intensity in the blood region before and after processing. The echo intensity of the blood region was defined as the mean value of the envelope signal obtained by the Hilbert transform. The echo intensity derived from the first RF trace was used as a reference to estimate the original intensity before processing. The relative intensity changes after processing a number of subsequent RF traces were measured with the ratio between the processed intensity and the intensity of the first RF trace.

**Qualitative evaluation of the RF methods:** To verify the visual improvement by the RF techniques, another experiment was performed to obtain a complete cross-sectional scan. Because of the limitation in data storage capability, the current set-up was not able to acquire cross-sectional RF data in real-time. A stepper-motor device was used to rotate the transducer at a slow speed in synchronism with the blood pressure. The pressure gating ensured that RF data were acquired from the same phase of the cardiac

cycle, and thus minimize the motion artifact for off-line image reconstruction. The cross-sectional scan was obtained in 200 angular steps. At each angle, ultrasonic data were acquired in a similar way as above-described. The averaging and correlation processing were performed on the first 8 RF traces at each step. The resulting data were scan-converted and displayed as a gray-scale image. Logarithmic compression was applied to the image data allowing the resulting display to be comparable to that from a conventional IVUS imaging system.

### 3 RESULTS

#### 3.1 Correlation Curve

The mean correlation values of the regional measurements are plotted as a function of the delay in Fig. 4. The correlation curve in the wall region declines slowly as the delay increases and maintains a high value ( $>0.8$ ) till the end of the data acquisition period. The correlation output of the blood region, in contrast, drops rapidly as the delay increases. The mean correlation value is less than 0.4 between the first and second RF traces. The correlation time of the blood region is approximately 1 ms. Although it is not possible to measure the correlation time of the wall region due to the short data acquisition period, one may predict that  $T_c$  will be  $\gg 6$  ms from the trend of the curve.

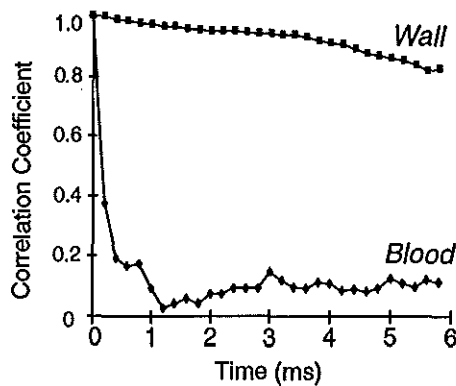


Fig. 4. Mean correlation values determined in the two regions. Note a steep drop in the correlation curve of the blood region as compared to a slow decrease in the correlation curve of the wall region.

#### 3.2 Correlation Distribution

The distribution of the correlation values calculated in the small window is shown in Fig. 5. In the wall region, the outputs are mostly concentrated around the high correlation values and spread slowly as the delay increased. The values from the blood region show an almost random distribution in the whole correlation range. The high variability in the correlation output suggests that correlating only two RF traces may still produce a high value at some locations of the blood region. Therefore, more traces are needed for a reliable rejection of the blood echoes.

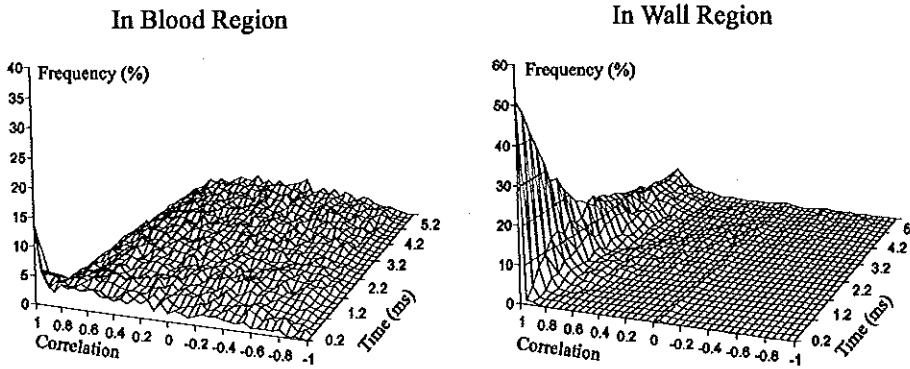


Fig. 5. Distribution of the correlation values calculated in a non-overlapping window of 7 points. Note the randomness of the correlation outputs in the blood region for all delay time.

### 3.3 Intensity Changes by RF Processing

Fig. 6 illustrates the intensity decrease in the blood region resulting from the temporal averaging and correlation processing. The results show averaging a number of RF traces is able to reduce the intensity of the blood echoes. Averaging 8 sequential RF traces results in approximately 50% decrease of the echo intensity. Only a small improvement can be gained by averaging more than 8 traces. By applying the correlation procedure in 8 RF traces, the signal intensity of blood was reduced to less than 10% of its original intensity by correlating 8 RF traces.

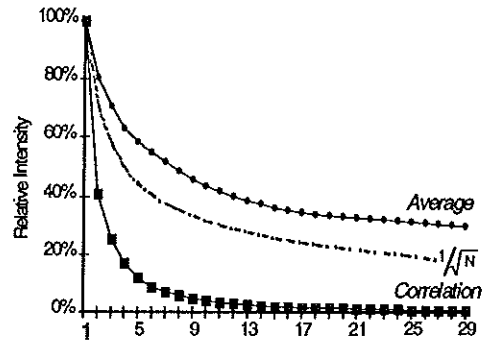
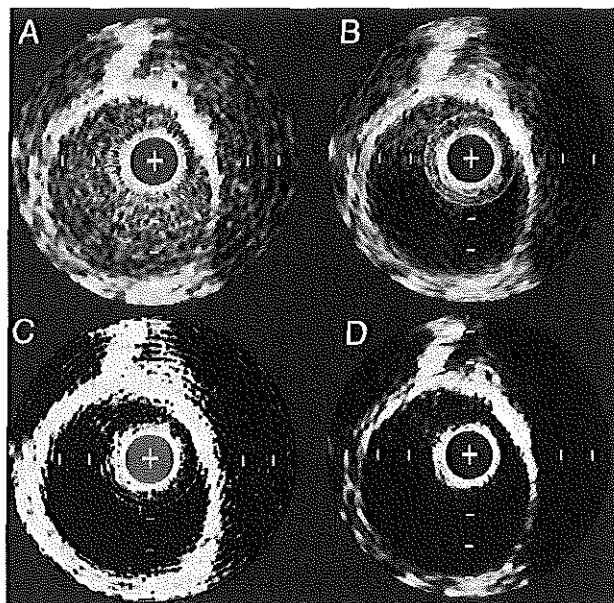


Fig. 6. Intensity decrease resulting from the averaging and correlation methods. The theoretical reduction curve ( $1/\sqrt{N}$ ) of averaging completely uncorrelated RF sequences plotted as dotted line for comparison.

### 3.4 Image Enhancement by RF Processing

The results of the image enhancement by processing 8 RF traces from the cross-sectional image data are illustrated in Fig. 7. The unprocessed image was constructed from the first trace of each RF sequence (panel A). As can be seen, strong blood scattering echoes obscure the visibility of the luminal boundary. The luminal intensity was reduced slightly by averaging 8 sequential RF traces (Panel B). The actual visual





*Fig. 7. Example of RF processing from the cross-sectional image data. A: image constructed from the first RF trace of each angle. B: result after averaging of 8 RF traces per angle. C: image constructed from the correlation weighting function obtained from 8 RF traces per angle. D: image processed by multiplying B and C.*

enhancement was partly reduced by the use of logarithmic compression during video display. Panel C displays the weighting function derived by the correlation method. The image shows a binary structure with white (1) for tissue and value black (0) for blood. The image processed by multiplying (B) and (C) shows a significant improvement in the image contrast between the lumen and wall (D). The blood scattering echoes were mostly removed while the details in the arterial wall were preserved.

#### 4 DISCUSSION

Results of this study show the differences in the correlation properties between blood and vessel wall. The movement of blood particles can be separated into two velocity components, the transverse and axial flows, in relation to the ultrasound beam direction. The transverse flow causes blood particles to move in and out of the ultrasound beam while the axial flow moves blood particles along the ultrasound beam. The transverse and axial flows will alter the correlation output of the blood signals in different manners. In the case of the transverse flow, the signals generated by the newly moving-in particles will be uncorrelated with those generated by the particles staying

inside the ultrasound beam because of the random distribution of blood particles. Thus, the *correlation time* can be estimated from the beam width divided by the flow velocity (Bonnetfous 1989). The beam width of the IVUS system used is 1 mm. Assuming the mean blood velocities for the normal peripheral flow are in the range of 40-80 cm/s, the time required by blood particles to travel through the ultrasound beam will be in the order of milliseconds. The measured  $T_c \approx 1$  ms falls within the range of this estimation. As the transducer is placed perpendicular to the vessel wall in the IVUS setting, the transverse velocity is expected to be a main factor for the decrease of the *correlation time*. On the other hand, the presence of the echo catheter may cause the development of the axial velocity in part of blood flow. The axial movement of blood particles can be observed from the diagonal moving structure on the M-mode image in Fig. 2. The axial flow component introduces a phase shift between the two consecutive RF signals. The relation between the correlation output and the phase shift is determined by the autocorrelation curve of the system response. In a typical situation, an axial displacement of 12  $\mu\text{m}$  may yield 180 degree phase shift and a correlation value of -1. For two RF traces separated by 200  $\mu\text{s}$ , the equivalent axial velocity will be 6 cm/s. The negative correlation was not detected in the correlation curve because the influence of the transverse flow was the dominant factor when measuring the mean value in the whole blood region. In the small window, the phase shift effect can be appreciated from Fig. 5, where the correlation values of the blood region scatter randomly over the range from -1 to 1. The slow decrease of the correlation output measured in the wall region was probably caused by the wall pulsation producing motion in line with the ultrasound beam. Measurements on wall distensibility with IVUS have exhibited 5% (The et al. 1992) and 18% (Nissen et al. 1991) luminal area changes during the cardiac cycle for the peripheral and coronary arteries, respectively. When translating this information to wall velocities, the maximum axial velocity of the vessel wall will be lower than 1 mm/s.

Temporal averaging is a simple method to reduce the amplitude of a random signal. Assuming the blood signals as wide-band random noise, the averaged intensity output is expected to be reduced by the square root of the number of the RF traces used. A similar trend as that predicted by the square root reduction can be observed by comparing the two curves in Fig. 6. The averaging effect obtained in our data set, however, is lower than the square root reduction because the RF sequences used for average are still partly correlated. The correlation weighting function, on the other hand, is able to produce a near zero value whenever the signals are uncorrelated. Combination of the averaging and correlation methods has shown to be more efficient; the blood echoes can almost be rejected by processing 8 RF traces. Real-time

implementation of the correlation processing, however, will require sophisticated digital circuits with high processing speed and large storage capacity. Another consideration in real-time application is the timing design for the cross-sectional scan. The correlation procedure requires a prolonged scan time at each beam position in order to collect sufficient changes in the blood scattering signals. This will be at the expense of either a reduce frame-rate or a lower angular resolution. For the example given in Fig. 7, the time required for each beam position is 1.6 ms ( $8 \times 200 \mu\text{s}$ ). In order to achieve 200 angular positions in one cross-sectional image, the frame-rate will be reduced to 2.8 frame/s, which is too low to display rapid motion of the arterial wall or flaps. One method to increase the frame-rate is to reduce the number of scan lines by performing image interpolation between scan lines. Another solution is to extend the correlation procedure by applying a multidimensional correlator on a sequence of RF data blocks. A multidimensional processing may take advantages of the blood scattering properties in both the time and spatial domains to reduce the waiting period at one beam position.

This study was performed in the peripheral artery with normal blood flow. The results may be applicable to intracoronay imaging as the coronary flow has approximately the same velocity ranges as that of the peripheral arteries. The influence of a lesion with a reduced flow velocity was not included in this study. Since the M-mode RF data were collected randomly from different cardiac phases, the measurement results presented an averaged effect of a pulsatile flow. In practice, the effectiveness of the correlation processing depends mainly on the differences between the dynamics of flowing blood and wall motion.

## 5 CONCLUSION

High blood echogenicity in IVUS imaging has been a bottle-neck for accurate determination of the luminal boundary, particularly for computerized quantification. Information about the time-varying characteristics of the blood scattering is essential for improving the IVUS image quality. This study indicates that the RF correlation time is significant shorter in the blood region ( $T_c \approx 1 \text{ ms}$ ) than that measured in the wall region ( $T_c \gg 6 \text{ ms}$ ). The fast de-correlation in the blood scattering signals allows an RF processing to be performed without smearing dynamic wall motion in real-time IVUS imaging. A simple temporal RF averaging is able to reduce 50% of the original blood echo intensity. The proposed correlation technique improves the blood suppression up to a 90% intensity reduction, and thus provides a satisfactory contrast enhancement for the lumen interface. Furthermore, the correlation weighting function

can be incorporated into an automatic contour detection algorithm for real-time extraction of the luminal boundary.

## 6 REFERENCES

1. Bohs L.N.; Trahey G.E. A novel method for angle independent ultrasonic imaging of blood flow and tissue motion. *IEEE Trans. Biomed. Eng.* 3:280-286;1991.
2. Bom, N.; ten Hoff, H.; Lancée, C. T.; Gussenhoven, E. J.; Bosch, J. G. Early and recent intraluminal ultrasound devices. *Int J Cardiac Imag.* 4:79-88; 1989.
3. Bonnefous, O. Statistical analysis and time correlation processes applied to velocity measurement. *IEEE Ultrasonics Symposium Proceedings:* 887-892; 1989.
4. de Jong B.G.M.; Arts T.; Hoeks A.P.G.; Reneman R.S. Experimental evaluation of the correlation interpolation technique to measure regional tissue velocity. *Ultrasonic Imaging* 13:145-161;1991.
5. De Kroon, M. G. M.; Slager, C. J.; Gussenhoven, W. J.; Serruys, P. W.; Roelandt, J. R. T. C.; Bom, N. Cyclic changes of blood echogenicity in high-frequency ultrasound. *Ultrasound Med. Biol.* 17:723-728; 1991.
6. De Kroon, M. G. M. Acoustic backscatter in arteries. Ph.D. Thesis. Erasmus University, Rotterdam; 1993.
7. Ferrara K.W.; Zagar B.; Algazi R.; Silverman R.; Sokil-Melgar J. An experimental evaluation of the received signal from blood at 50 MHz. *IEEE Ultrasonics Symposium Proceedings.* 1603-1607;1994
8. Foster, F. S.; Obara, H.; Bloomfield, T.; Ryan, L. K.; Lockwood, G. R. Ultrasound backscatter from blood in the 30 to 70 MHz frequency range. *IEEE Ultrasonics Symposium Proceedings:* 1599-1602; 1994.
9. Gronningsaeter, A.; Angelsen, B. A. J.; Heimdal, A.; Torp, H. Vessel wall detection and blood noise reduction in intravascular ultrasound imaging. *IEEE Ultrasonics Symposium Proceedings:* 1609-1612; 1994.
10. Gronningsaeter, A.; Angelsen, B. A. J.; Gresli, A.; Torp, H. Blood noise reduction in intravascular ultrasound imaging. *IEEE Trans. Ultrason., Ferroelec., Freq. Contr.* 42:200-208; 1995.
11. Hein A.; O'Brien D. Current time-domain methods for assessing tissue motion by analysis from reflected ultrasound echoes-A review. *IEEE Trans. Ultrason., Ferroelec., Freq. Contr.* 40:84-102; 1993.
12. Li, W.; Bosch J. C.; Gussenhoven, W. J.; Rijsterborgh, H.; Reiber, J. H. C.; Bom, N. Semiautomatic frame-to-frame tracking of the luminal border from intravascular ultrasound. *Proceedings Computers in Cardiology:* 353-356; 1992.

13. Li W.; Gussenhoven, E. J.; Zhong, Y.; The, S. H. K.; Pieterman, H.; van Urk, H.; Bom, N. Temporal averaging for quantification of lumen dimensions in intravascular ultrasound images. *Ultrasound Med. Biol.* 20:117-122, 1994.
14. Lockwood, G. R.; Ryan, L. K.; Hunt, J. W.; Foster, F. S. Measurement of the ultrasonic properties of vascular tissues and blood from 35-65 MHz. *Ultrasound Med. Biol.* 17: 653-666; 1991.
15. Nissen, S. E.; Curley, J. C. Application of intravascular ultrasound for detection and quantitation of coronary atherosclerosis. *Int. J. Card. Imag.* 6:165-177; 1991.
16. Pasterkamp, G.; van der Heiden, M. S.; Post, M. J.; Ter Haar Romeny, B.; Mali, W. P. T. M.; Borst, C. Discrimination of intravascular lumen and dissections in a single 30 MHz ultrasound image: use of 'confounding' blood backscatter to advantage. *Radiology* 187:871-872; 1993.
17. Shung, K. K.; Kuo, I. Y.; Cloutier, G. Ultrasonic scattering properties of blood. *Intravascular Ultrasound* (J. Roelandt, E.J. Gussenhoven, N. Bom, eds.) Kluwer Academic Publishers, Dordrecht: 79-90; 1993.
18. The, S. H. K.; Gussenhoven, E. J.; Li, W.; De Feyter, P.; Serruys, P. W.; Wilson, R. A.; Bom N. Intravascular ultrasonic assessment of lumen geometry and distensibility of the angiographically normal artery: a correlation with quantitative angiography. *Echocardiography* 9: 133-139; 1992.
19. The, S. H. K.; Gussenhoven, E. J.; Zhong, Y.; Li, W.; van Egmond, F. The effect of balloon angioplasty on the femoral artery evaluated with intravascular ultrasound imaging. *Circulation* 86:483-493; 1992.
20. Yock, P. G.; Fitzgerald, P. J.; Sudhir, K. Intracoronary ultrasound scanning - clinical experience and new insights. *Intravascular Ultrasound* (J. Roelandt, E.J. Gussenhoven, N. Bom, eds.) Kluwer Academic Publishers, Dordrecht: 17-32; 1993.
21. Yuan, Y. W.; Shung, K. K. Ultrasonic backscatter from flowing blood. I. Dependency on shear rate and hematocrit. *J. Acoust. Soc. Am.* 84:52-58; 1988.

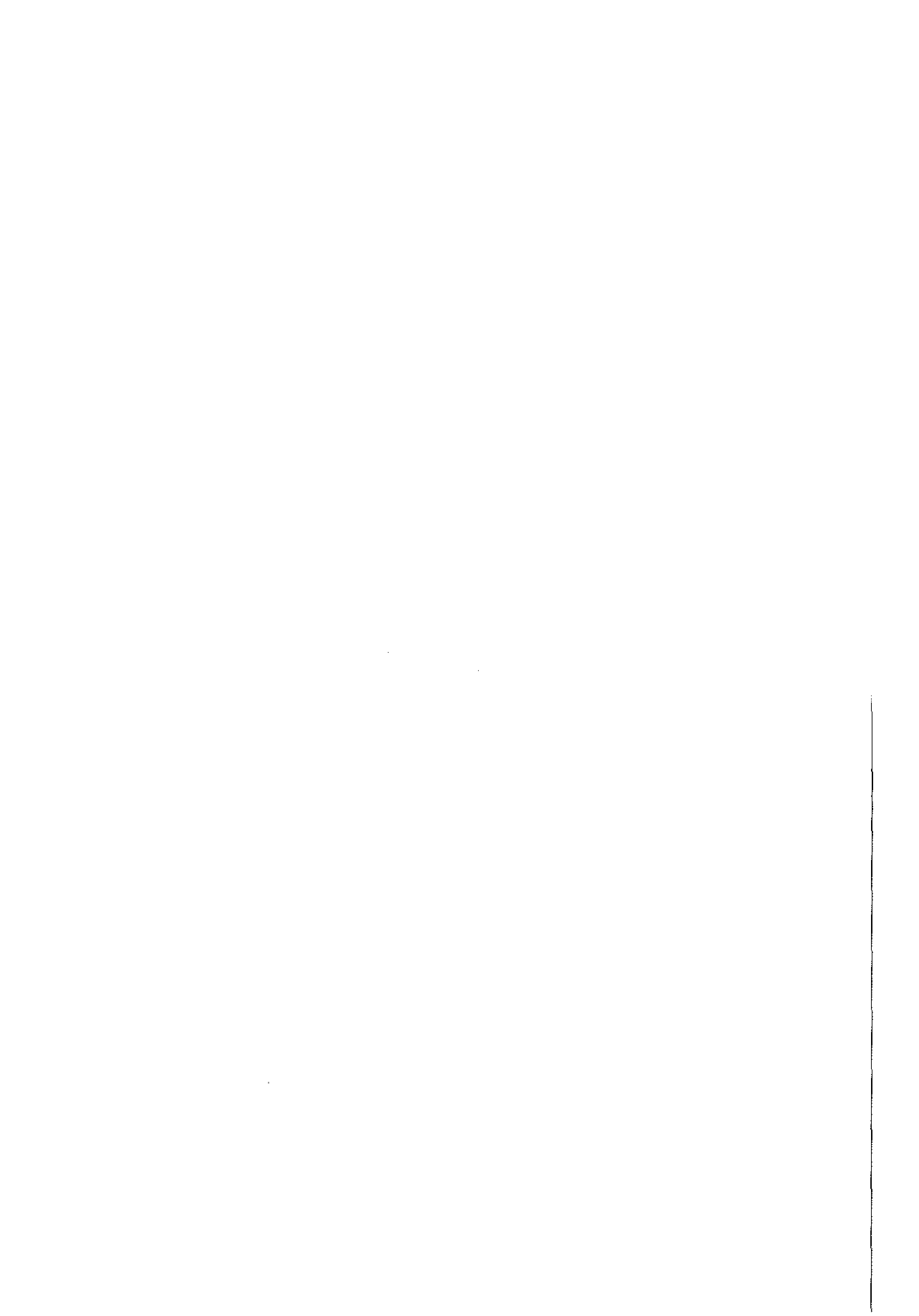


## CHAPTER 8

---

# DECORRELATION PROPERTIES OF INTRAVASCULAR ECHO SIGNALS

W. Li, C.T. Lancée, E.I. Céspedes, A.F.W. van der Steen, N. Bom.





**ABSTRACT**

When a cluster of blood particles travels through an intravascular ultrasound imaging plane, the received echo signals decorrelate at a rate that is related to the flow velocity. In this paper, the feasibility of extracting blood velocity from the decorrelation function of radio frequency signals was investigated through theoretical analysis and computer simulation. A computer model based on the impulse response method was developed to generate the ultrasound field of a 30 MHz intravascular transducer. The decorrelation due to the scatterer displacement as well as other non-motion related decorrelation sources were studied. The computer simulations show that the decorrelation function is linearly related to the lateral displacement. The monotonous relationship between correlation and displacement provides possibilities to estimate flow velocity with decorrelation measurements. Because of the complexity of the beam profile in the near-field, assessment of local velocities requires detailed knowledge of the decorrelation at each axial beam position. Decorrelation Sources other than the lateral displacement may cause a bias in the decorrelation-based velocity measurements. Measurement variations present a major challenge for the decorrelation estimate in small range windows. An approach based on multiple decorrelation measurements should be adopted in order to reduce the variations. In conclusion, results of this study suggest that it is feasible to measure flow velocity by quantifying the decorrelation of intravascular ultrasound signals from blood.

**1 INTRODUCTION**

The displacement of an ultrasound-scattering material such as blood moving through the beam of an ultrasound transducer results in concomitant changes (decorrelation) in the received echo signal. This phenomenon is clearly exhibited by a catheter-based intraluminal imaging technique, intravascular ultrasound (IVUS), in which the ultrasound beam is transmitted almost perpendicular to the arterial tissue and blood flow. With real-time IVUS imaging, it can be seen that the scattering pattern of flowing blood varies rapidly over time. This is caused by the fact that the flow stream drives randomly distributed blood particles through the imaging volume, resulting in decorrelation of the received echo signals as a function of time delay.

Two important characteristics of the decorrelation of intravascular echo signals should be addressed. First, because the flow usually has a higher velocity than wall motion, blood echo signals decorrelate significantly faster than those of tissues. Several groups (Pasterkamp et al. 1993; Li et al. 1994, *Chapter 6*; Li et al. 1996a; Gronningsaeter et al. 1995, 1996) have demonstrated that methods based on either video or radio frequency (RF) processing can take advantages of the time-varying feature of blood echoes to

improve the IVUS image. Li et al. (1996b, *Chapter 7*) have documented a significant difference in the correlation time between blood and tissue through RF analysis of in vivo echo data. Therefore, the contrast in the decorrelation of blood and tissue may be used to enhance the luminal boundary. Secondly, it is a reasonable hypothesis that the speed of the blood decorrelation procedure should be related to the flow velocity. In other words, the faster blood particles move across the ultrasound beam, the higher the decorrelation rate of the received signals will be. The velocity-decorrelation relation may be used to estimate flow velocity by means of quantifying the decorrelation rate from blood scattering signals. For both applications, the decorrelation as a function of scatterer displacements is the most important basis. Several applications of echo signal decorrelation for the assessment of tissue dynamics have been reported. The decorrelation due to lateral beam translation has been studied in detail for compound scanning (Wagner et al. 1983, 1988; Trahey et al. 1986). Decorrelation factors such as transverse velocities and velocity variations/gradients were addressed as error sources in time-domain velocity measurement techniques (Bonnetfous et al. 1989; Foster et al. 1990; Hein et al. 1993). Decorrelation measurements have been proposed for detection of tissue motion and the transverse blood velocity. Dickinson et al. (1982) reported a decorrelation based method for tissue motion estimation. Zhang et al. (1993) and Dotti et al. (1996) applied the decorrelation measurement to estimate the angle between the ultrasound beam and blood flow in order to retrieve the true blood velocity vector.

In all the previous work, however, decorrelation assessment was concentrated on the far field or the focus of a transducer. Conversely, most intravascular imaging is performed within the near field of the transducer. A typical IVUS system employs a circular unfocused transducer with a diameter of approximately 1 mm; the scanning depth starts at the extreme near field ( $\approx 0.1$  mm) and extends up to the far field ( $> 5$  mm) of the ultrasound beam. Another characteristic in IVUS imaging as compared to most of conventional medical ultrasound applications is the use of high ultrasonic frequencies (20-40 MHz) and a wide system bandwidth ( $\approx 20$  MHz). The present study was therefore designed to investigate the decorrelation properties of the near field of a high frequency broadband transducer. The investigation was conducted using theoretical analysis and a computer simulation of an IVUS transducer. The ultimate goal was to study the feasibility of extracting blood velocity from the decorrelation function of RF intravascular echo signals.

## 2 THEORETICAL ANALYSIS

The ultrasound beam considered in this study is generated from a circular transducer, which is symmetric on the cross-sectional plane (x-y plane). Thus, a two-dimensional

(x-z) coordinate system can be used to represent an IVUS imaging configuration (Fig. 1). The x-axis is the typical direction of blood flow and the z-axis is defined by the center of the ultrasound beam. With reference to this coordinate system, the movement of blood particles across and along the ultrasound beam is termed the *lateral* and *axial* displacement, respectively.

The following decorrelation factors are investigated:

1. lateral displacement
2. axial displacement
3. signal to noise ratio
4. velocity gradient
5. correlation variance

### 2.1 Lateral decorrelation

Fig. 1 illustrates a volume of blood scatterers moving across the ultrasound beam. At time  $T_1$  and  $T_2 = T_1 + \Delta T$ , the scatterer volume that generates RF signals  $S_1$  and  $S_2$  can be divided into 3 parts:

**V1:** scatterers inside the beam at  $T_1$  move outside the beam at  $T_2$ .

**V2:** new scatterers move inside the beam at  $T_2$ .

**V3:** scatterers remain inside the beam at  $T_1$  and  $T_2$ .

Denote  $S_{v1}$  and  $S_{v2}$  are signals generated by volume **V1** and **V2**, respectively;  $S_{v3}$  and  $S'_{v3}$  represent the signals before and after the lateral displacement of **V3**. The RF traces  $S_1$  and  $S_2$  can be written as:

$$\begin{cases} S_1 = S_{v1} + S_{v3} \\ S_2 = S_{v2} + S'_{v3} \end{cases} \quad (2.1.1)$$

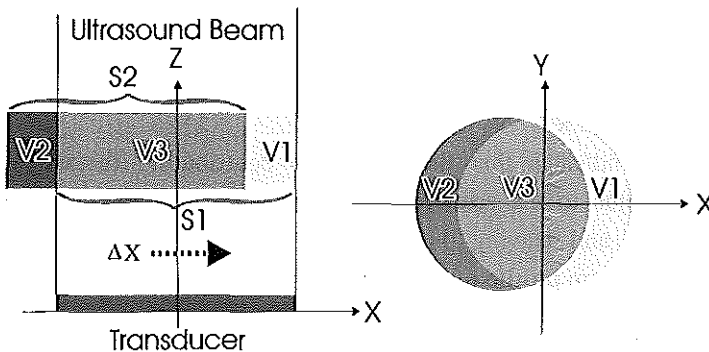


Fig. 1. The coordinates of the IVUS imaging setup with the z-axis representing central axis of the ultrasound beam. Blood scatterers move laterally through the beam along the x-axis. The scatterer volume is represented by  $V1+V3$  at  $T_1$  and  $V2+V3$  at  $T_2$ . The corresponding view on the X-Y plane is shown the right panel.

The correlation coefficient between  $S_1$  and  $S_2$  with zeros mean is calculated by:

$$\begin{aligned} \rho_{12} &= \frac{\int S_1 S_2 dt}{\sqrt{\int [S_1]^2 dt} \sqrt{\int [S_2]^2 dt}} = \frac{\int (S_{v1} + S_{v3})(S_{v2} + S'_{v3}) dt}{\sqrt{\int [(S_{v1} + S_{v3})]^2 dt} \sqrt{\int [(S_{v2} + S'_{v3})]^2 dt}}, \quad (2.1.2) \\ &= \frac{\int (S_{v1} S_{v2} + S_{v1} S'_{v3} + S_{v3} S_{v2} + S_{v3} S'_{v3}) dt}{\sqrt{\int ([S_{v1}]^2 + 2S_{v1} S_{v3} + [S_{v3}]^2) dt} \sqrt{\int ([S_{v2}]^2 + 2S_{v2} S'_{v3} + [S'_{v3}]^2) dt}} \end{aligned}$$

where  $\int S_{v1} S_{v2} dt$ ,  $\int S_{v1} S'_{v3} dt$ ,  $\int S_{v3} S_{v2} dt$ ,  $\int S_{v1} S_{v3} dt$  and  $\int S_{v2} S'_{v3} dt$  are the cross-correlation values of echo signals of **V1**, **V2** and **V3**. Since scatterers are assumed to be randomly distributed, these cross-correlation terms of different volumes in (2.1.2) are close to zero when integrated in a sufficient long period. Removing the cross-correlation terms, expression (2.1.2) is written as:

$$\rho_{12} = \frac{\int S_{v3} S'_{v3} dt}{\sqrt{\int ([S_{v1}]^2 + [S_{v3}]^2) dt} \sqrt{\int ([S_{v2}]^2 + [S'_{v3}]^2) dt}}. \quad (2.1.3)$$

Assuming a homogenous scatterer density, the number of scatterers that enters the beam is identical to that exits the beam. Let  $\kappa$  be the signal power ratio between the scatterers moving in/out and those staying inside the beam:

$$\kappa \approx \frac{\int [S_{v2}]^2 dt}{\int [S'_{v3}]^2 dt} \approx \frac{\int [S_{v1}]^2 dt}{\int [S_{v3}]^2 dt}. \quad (2.1.4)$$

The correlation coefficient for the scatterers remaining in the beam with a lateral displacement is:

$$\rho'_{12} = \frac{\int S_{v3} S'_{v3} dt}{\sqrt{\int [S_{v3}]^2 dt} \sqrt{\int [S'_{v3}]^2 dt}}. \quad (2.1.5)$$

Combining (2.1.4) and (2.1.5),  $\rho_{12}$  can be rewritten as:

$$\rho_{12} = \frac{\rho'_{12}}{\sqrt{1 + 2\kappa + \kappa^2}} = \frac{\rho'_{12}}{(1 + \kappa)}. \quad (2.1.6)$$

Equation (2.1.6) indicates that there are two contributing factors for the lateral decorrelation: 1) due to the scatterers moving laterally inside the beam; 2) due to scatterers entering and leaving the beam. The relative weight of these factors is determined by the beam profile of a transducer.

## 2.2 Axial displacement

The correlation coefficient of the received RF signals decreases quickly when the phase is shifted as a result of the axial displacements of blood scatterers. The decorrelation due to a phase shift is determined by the autocorrelation function of RF signals, mainly

by the central frequency and bandwidth. For example, at a central frequency of 30 MHz, an axial displacement of 12  $\mu\text{m}$  will cause a 180 degree phase shift and produce a negative correlation value. Although the axial velocity in the IVUS setup is typically very small due to the near 90° angle between the beam and flow, the phase decorrelation is still much higher than the decorrelation of a lateral displacement. Thus, differences in the signal phase must be removed by a phase matching procedure. For an ideal beam profile of uniform intensity distribution, the signal generated by a scatterer moving axially is time delayed replica's of its initial position. The two signals will be perfectly correlated after the phase matching procedure. In reality, the beam profile is inhomogenous along the axial direction, particularly in the extreme near field. Therefore, the correlation output is expected to be modulated by the axial beam pattern.

### 2.3 Decorrelation due to noise

Noise is a well-know source for a decrease of the signal correlation. Considering  $S_1$  and  $S_2$  are the true RF signals at  $T_1$  and  $T_2$  and  $n_1$  and  $n_2$  are band-pass white noises added to the signals, the received signals  $S_{n1}$  and  $S_{n2}$  can be written as:

$$\begin{cases} S_{n1} = S_1 + n_1 \\ S_{n2} = S_2 + n_2 \end{cases} \quad (2.3.1)$$

The correlation coefficient of  $S_{n1}$  and  $S_{n2}$  is defined by:

$$\rho_{n12} = \frac{\int S_{n1} S_{n2} dt}{\sqrt{\int [S_{n1}]^2 dt} \sqrt{\int [S_{n2}]^2 dt}} = \frac{\int (S_1 + n_1)(S_2 + n_2) dt}{\sqrt{\int [(S_1 + n_1)]^2 dt} \sqrt{\int [(S_2 + n_2)]^2 dt}} \quad (2.3.2)$$

The noise signals  $n_1$  and  $n_2$  are assumed to have random amplitudes and phases with zero means and are uncorrelated with each other as well as with the true signals  $S_1$  and  $S_2$  at any given  $T_1$  and  $T_2$ . In this case, expression (2.3.2) has the same cross-correlation components with a mean value of zero as discussed in (2.1.2). Thus, a similar analysis of (2.1.6) can be applied to (2.3.2). Let the signal to noise ratio (SNR) be the power ratio between signal and noise:

$$SNR \approx \frac{\int [S_1]^2 dt}{\int [n_1]^2 dt} \approx \frac{\int [S_2]^2 dt}{\int [n_2]^2 dt} \quad (2.3.3)$$

and the correlation coefficient of the signals  $S_1$  and  $S_2$  be:

$$\rho_{12} = \frac{\int S_1 S_2 dt}{\sqrt{\int [S_1]^2 dt} \sqrt{\int [S_2]^2 dt}} \quad (2.3.4)$$

Expression (2.3.2) can be rewritten as:

$$\rho_{m12} = \frac{\rho_{12}}{\sqrt{1 + 2 / SNR + [1 / SNR]^2}} = \frac{\rho_{12}}{\left(1 + \frac{1}{SNR}\right)}. \quad (2.3.5)$$

Equation (2.3.5) indicates that correlation in the received signals decreases as SNR decreases. At a given SNR level, the correlation output is reduced by a constant weighting factor, which can be compensated if the SNR level can be measured.

#### 2.4 Decorrelation associated with velocity gradient

Scatterers may move at different velocities within a range cell due to a non uniform velocity profile along the ultrasound beam. For example, in vascular application the commonly observed parabolic velocity profile has a maximum velocity gradient at the region close to the arterial wall. A velocity gradient causes a range of lateral or axial displacements of scatterers within the correlation window.

The axial velocity gradient may increase the signal decorrelation dramatically since it produces different phase shifts along an RF signal time trace. Thus, phase can be matched within the correlation window only in small parts of the trace; mismatching parts will reduce the correlation output rapidly. Bonnefous et al. (1986) established that correlation reduced by variances in time shifts follows:

$$\rho = \rho_o (1 - 2\pi^2 f_o^2 \sigma^2[\delta T]), \quad (2.4.1)$$

where  $f_o$  is the central frequency and  $\sigma^2[\delta T]$  is the variance in the axial time shift. The term  $\sigma^2[\delta T]$  can be derived from the gradient value of the velocity distribution. Since the term  $\sigma^2[\delta T]$ , caused by an axial velocity gradient, is proportional to the time interval between two RF traces, its contribution soon may become a dominant factor.

The lateral decorrelation can be considered as an averaged effect of the lateral beam modulation in combination with the exchange of many scatterers in a sample volume, which is less dependent on the displacement of each individual scatterer. Hence, the lateral velocity gradient is expected to have a smaller influence on the decorrelation procedure as compared to the axial velocity gradient.

#### 2.5 Variance of correlation estimate

The ideal correlation estimator needs to integrate the RF signals over infinite time. In practice, the correlation value is usually estimated with a limited time window to achieve spatial resolution and may deviate from the true value. For the measurement of local velocities, the size of a correlation window determines the resolution of the measured velocity profile. To obtain a good resolution, a small correlation window is preferred. Furthermore, as discussed above, the presence of an axial velocity gradient limits the use of a large time window. Thus, the accuracy of a decorrelation-based

technique for velocity measurements depends to a large extent upon the degree of variance of correlation estimate in a small window.

Variation in the correlation estimate at a given window length is closely related to the system bandwidth. When an RF signal is modeled as bandwidth limited Gaussian white noise with zero mean, it can be shown that the error in the estimate of the cross-correlation function is given by:

$$\varepsilon \approx \frac{1}{\sqrt{2BT}} [1 + \rho_{12}^{-2}]^{1/2}, \quad (2.5.1)$$

where B is the bandwidth of Gaussian noise, T is the length of a time window and  $\rho_{12}$  is the correlation coefficient (Bendat & Piersol 1983). The product of B and T represents the number of available independent measurements at a given window length. To reduce variation in correlation estimate, one should either increase the system bandwidth or use a longer time window. Equation (2.5.1) also indicates that a low correlation value results in a high degree of measurement variations. Thus, low correlation values should be excluded in the velocity estimation.

### 3 COMPUTER SIMULATION

#### 3.1 Computer modeling method

To investigate the correlation properties of blood scattering, a model using the impulse response method (Stepanishen 1971) was developed to describe the beam profile of a circular transducer from the extreme near field to far field. Details of the impulse response modeling are presented in Appendix II. Briefly, each scatterer is considered as a point source retransmitting a spherical sound field towards the transducer. At the surface of the transducer the pressure distribution can be described as a Rayleigh integral. In the frequency domain this integral can be expressed in discrete form with a desired precession irrespective to near or far field scatterer positions. Thus, there is no theoretical constrains for the geometry of the transducer as well as the position of scatterers in this modeling approach.

#### 3.2 General settings in computer simulation

**Transmission pulse:** the pulse was defined as a 30 MHz central frequency wave with a Gaussian envelope:

$$p(t) = e^{-\frac{t^2}{2\sigma^2}} \sin(2\pi f_c t)$$

with:  $f_c = 30 \text{ MHz}$       Central frequency  
 $\sigma = 20 \text{ ns}$       Pulse length factor

The signal bandwidth was expressed as the equivalent noise bandwidth which is the width of a rectangular spectrum having the same power and peak amplitude as the Gaussian (Céspedes et al. 1995). The bandwidth of the transmission pulse was determined by:

$$B = \frac{1}{2\sqrt{\pi}\sigma}, \quad (3.2.1)$$

which was approximately 14 MHz for  $\sigma = 20$  ns. The RF signals simulated with the impulse response model were sampled at 1 GHz.

**Scatterer volume:** Five scatterer sets were generated over a depth of 0.5 - 4 mm. Each set contains 5000 scatterers randomly distributed in a volume of X=2 mm, Y=1 mm and Z=3.5 mm (at depth of 0.5~4 mm). The scatterer concentration was 700 scatterer per mm<sup>3</sup>. At each moment, the number of active scatterers inside the beam was approximately half of the total scatterer number. Simulations I-V in the next section were performed using exactly the same data sets.

**Scatterer displacement:** Axial and lateral displacements were simulated by moving the whole scattering volume along the corresponding directions. The lateral position of the scatterer volume was shifted from left to right at a displacement of 50  $\mu$ m per step. A total of 20 RF traces with a maximum lateral displacement of 1 mm was generated per simulation.

### 3.3 Correlation procedure

The correlation curve in each simulated RF sequence ( $S_1...S_{20}$ ) was calculated in two steps. First, a phase matching procedure was performed to remove the phase difference induced by the axial displacement. The time shift between two consecutive RF traces was determined by the maximum value of a cross-correlation function. The RF traces ( $S_2...S_{20}$ ) were shifted in time to line up with the first trace  $S_1$ . The second step was to calculate the correlation coefficient  $\rho_{n,m}$  between two traces  $S_n$  and  $S_m$ ,  $n=1,...,19$ ,  $m=2,...,20$ . The correlation curve was obtained by an assemble averaging of the available correlation values:

$$\rho(n) = \frac{\sum_{k=1}^{N-n} \rho_{k,k+n}}{N-n}, \quad n=1...19, N=20 \quad (3.3.1)$$

### 3.4 Simulation methods

The correlation curve as a function of a lateral displacement was first established through computer simulation I whereby only lateral movements were introduced. The



result of simulation I was then used as a reference to evaluate the combined effect of other decorrelation factors with respect to the lateral decorrelation. Mean and standard deviations were obtained for each simulation from the calculations in the 5 scatterer volumes.

**Simulation I: Lateral displacement:** In order to observe the independent effect of  $\kappa$  and  $\rho'_{12}$  in (2.1.6), the responses of a) the scatterers staying inside the beam, b) the scatterers entering and leaving the beam and c) the whole scatterer volume were simulated separately. With the separate responses of (a) and (b), the values of  $\kappa$ ,  $\rho'_{12}$  and  $\rho_{12}$  were computed using (2.14-2.16) and plotted as a function of the lateral displacement for comparison with the complete response (c).

In the subsequent investigations, the correlation function simulated from the whole scatterer volume was used as a reference curve.

**Simulation II: Axial displacement:** An axial displacement of 5  $\mu\text{m}$  per step (10% of the lateral motion corresponding to a beam-to-flow angle of  $84^\circ$ ) was included in this simulation. The maximum axial displacement was 100  $\mu\text{m}$ . The resulting RF traces were aligned in time by the phase matching procedure before the correlation calculation.

**Simulation III: Signal-to-noise ratio:** Band limited white noises with zero mean were added to the RF data in simulation I. The SNR level was changed from 5 to 40 dB at a step of 5 dB. The decorrelation curve was recalculated at each noise level and compared to the reference curve with zero noise level.

**Simulation IV: Velocity gradients:** The velocity gradient was defined as the difference between the maximum and minimum velocities (or displacements at a given time delay) within the correlation window. To study the effect of velocity gradients in the lateral and axial displacement, a linear velocity profile was added in this simulation. The velocity distribution along the beam axis was defined by:

$$v(z) = \alpha z + \beta.$$

Velocity gradients ranging from 25% to 200% of the mean velocity were introduced by changing  $\alpha$ ,  $\beta$  while keeping the mean velocities constant. The mean lateral and axial velocities were the same as simulation I and II (lateral: 50  $\mu\text{m}$ ; axial: 5  $\mu\text{m}$ ). Two separate simulations were performed. In the first simulation, pure lateral displacements with velocity gradients of 100% and 200% were studied (analogous to simulation I). In the second simulation, lateral and axial displacements with 25% to 200% velocity

gradients were combined (analogous to simulation II). Variation terms in (2.4.1) for the linear velocity distribution were derived to compare results obtained with Bonnefous's formula.

**Simulation V: Variance of correlation estimate:** Narrow band signals were generated by reducing the bandwidth of the transmission pulse with  $\sigma = 40$  ns. The equivalent noise bandwidth was 7 MHz. In the first simulation, the correlation curve of the narrow band signals calculated over the complete scatterer volume was compared to that obtained in simulation I. In the second simulation, correlation outputs were computed with different window lengths ranging from 20  $\mu\text{m}$  to 2.5 mm at a step of 20  $\mu\text{m}$ . The standard deviation of the correlation values was measured at the displacement of 0.2 mm ( $\rho \approx 0.6$ ). The degree of variation in correlation estimate was expressed as the ratio between the standard deviation and the mean correlation value.

## 4 RESULTS

### 4.1 Modeled beam profile

The beam profile obtained with the model is displayed in Fig. 2. The sensitivity of the transducer as a function of the scatterer position in the first few millimeters shows a high variation; this is the typical near field situation. Correlation of echo signals within this area is influenced by the complex field distribution in a way that is difficult to be expressed with an analytical method.

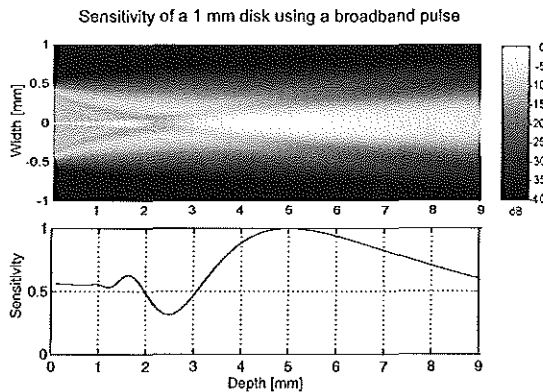


*Fig. 2. The roundtrip sensitivity of a 30 MHz transducer calculated with the computer model in both the near- and far-field (Top) and the sensitivity at the central axis of the transducer (Bottom). The complexity of the near-field profile can be appreciated in the range of 0~3 mm. The beam becomes homogenous at the depth  $\geq 5$  mm, which is the theoretical start point of the far-field.*

4.2 Simulation results

**Simulation I:** Fig. 3 shows the correlation curve as a function of the lateral displacement. The decorrelation curve simulated from the complete response shows a good agreement with the theoretical output predicted by (2.1.6). For a small displacement ( $<0.4$  mm), the decorrelation is mainly caused by the lateral beam modulation in both amplitude and phase. When a scatterer moving across the near field, rapid modulation of signal amplitudes may occur due to its complex intensity pattern. Phase modulation may be easier to interpret using a far-field model, wherein the phase of a scattered signal is simply determined by the distance between the center of the transducer and the scatterer position:  $r = \sqrt{x^2 + y^2 + z^2}$ . Thus, displacement in  $x$  or  $y$  directions will alter the phase response of each scatterer. This effect could be ignored when  $z \gg x, y$ . For IVUS application, it may become an important factor because of the combination of the near field nature and high ultrasonic frequencies. At the stage of a small displacement, the contribution of newly move-in scatterers is minimal since they are located at the edge of the beam profile whereat the ultrasonic intensity is usually much lower than at the center. As the scatterers move closer to the beam axis and their number increases, decorrelation due to the exchange of scatterers overtakes the effect of the lateral beam decorrelation. The product of the two contributions causes the correlation curve decreases approximately linearly with an increase of the lateral displacement.

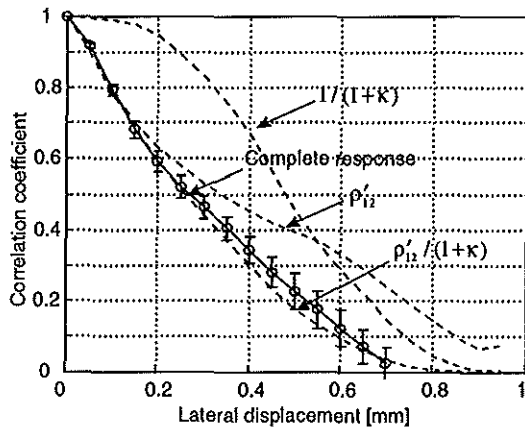


Fig. 3. Correlation curves (dotted line) from three separate responses of V1, V2 and V3 showing the decorrelation effects of the lateral beam modulation ( $\rho'_{12}$ ) and scatterers moving in/out the beam ( $1/(1+k)$ ). The complete response (solid line) simulated from the whole scatterer volume follows the curve calculated with  $\rho'_{12}/(1+k)$ .

**Simulation II:** After the phase matching procedure, the decorrelation curve with axial displacements is almost identical to that obtained in simulation I (Fig. 4). The axial beam modulation in IVUS imaging is minimal because the axial displacement of blood scatterers is in an order of micrometers, which will not produce significant changes in scattering intensity except for the extreme near field.

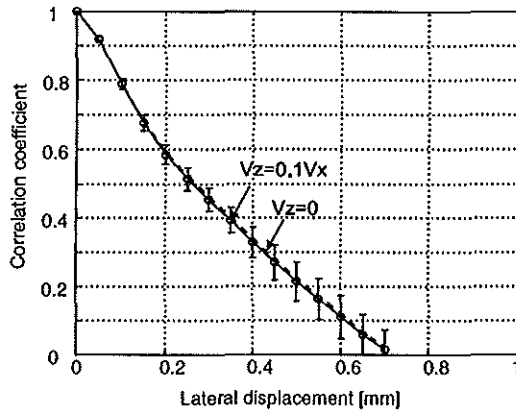


Fig. 4. Comparison of simulation with 10% of axial displacements to the decorrelation curve with pure lateral displacement (dotted line). After the phase matching procedure, the curve with axial displacement shows no noticeable differences as compared to the reference curve.

**Simulation III:** Fig. 5a plots the results of (2.3.5) as a function of SNR. To keep the errors in the correlation estimate less than 10%, the SNR in the measurement system needs to be higher than 20 dB. The correlation curves calculated from the signals with different SNR levels were plotted in Fig. 5b. The simulated curves follow the trend

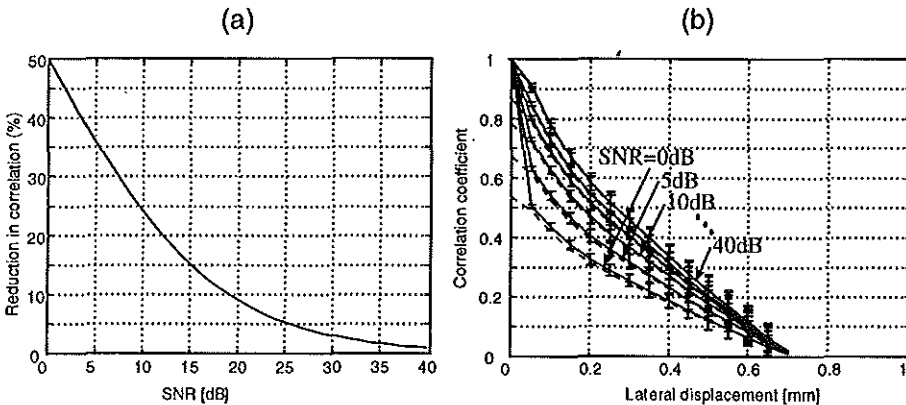


Fig. 5. a) Percent decrease of the signal correlation as a function of SNR. b) Correlation curves obtained after adding different noise levels. The dotted lines plot the results calculated by  $\rho_1/2(1+1/SNR)$ . A high noise level can be recognized from a large offset in decorrelation curve.

predicated by (2.3.5). The main effect of noise signals is an additional offset added to the beginning of the decorrelation curves. Thus, a high noise level could be identified from the discontinuity at the beginning of the correlation output.

**Simulation IV:** The result of the first simulation shows that no difference was observed between the narrow- and broadband signals for the correlation curves of the complete scatterer volume (Fig. 6a). Fig. 6b shows variations of correlation in the narrow band signals were consistently higher than those obtained with broadband signals. Both simulations indicate that variations decrease as the window length increases. The trend of decrease in variations follows the function of  $1/\sqrt{BT}$  with  $B$  defined as the equivalent noise band width. To obtain a reproducible correlation output of  $< 20\%$  variations, the window length should be longer than 0.5 mm for the broadband signal.

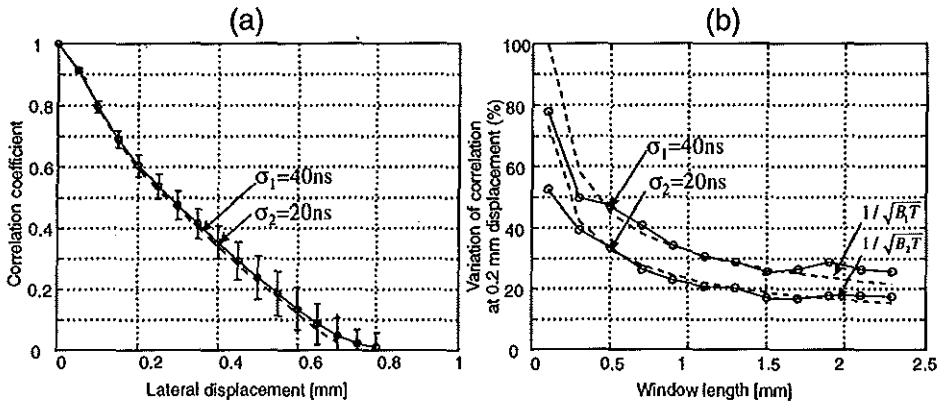


Fig. 6. a) Correlation curve obtained with a narrow band signal ( $\sigma_1=40\text{ ns}$ ) showing no significant differences to the reference curve ( $\sigma_2=20\text{ ns}$ ). b) Variations in correlation estimate as a function of the window length for both narrow band ( $\sigma_1=40\text{ ns}$ ) and broadband ( $\sigma_2=20\text{ ns}$ ) simulations. The narrow band signals show a higher degree of variations than the broadband signals. Both curves follow the theoretical reference of  $1/\sqrt{BT}$  plotted with  $B_2=14\text{ MHz}$  and  $B_1=7\text{ MHz}$  in the dotted lines.

**Simulation V:** Results show that the correlation curves simulated with only lateral gradients were identical to that obtained with a uniform displacement (Fig. 7). This confirms the expectation that a lateral velocity gradient may have a minimal effect on the decorrelation procedure. As shown in Fig. 7, the slope of the correlation curve is progressively modified as the axial velocity gradients increase from 25% to 200%; a larger axial velocity gradient results in a faster decrease in the correlation output. This

may introduce a significant overestimate in the velocity measurement using a decorrelation based method. The simulations show that the axial velocity gradient should be limited to 25% of the mean velocity (a difference of 1.25  $\mu\text{m}$  between the maximum and minimum axial displacements in two consecutive RF traces). For a given velocity distribution, the decorrelation effect of a velocity gradient can be minimized by using a small correlation window.

## 5 DISCUSSION

Using the computer model, we have analyzed the decorrelation properties of the ultrasound

beam from a circular transducer used for IVUS imaging. As main results, correlation of the RF signals from a moving cloud of randomly distributed scatterers decreases monotonously with the lateral displacement. The decrease in a correlation range of 1~0.5 is approximately linearly related to the lateral displacement. The decorrelation-displacement relationship provides the basis for extraction of the flow velocity based on decorrelation estimate. Once the decorrelation function of a specific transducer has been assessed, measured decorrelation values in blood signals can be converted to displacements; when the decorrelation measurement is performed at a controlled time interval, flow velocities can be derived from the ratio of displacement and time.

The beam profile calculated with the computer model exhibits rapid changes of the sound intensity in the near field. Since the lateral decorrelation is mainly determined by beam characteristics, the decorrelation rate will be range dependent. Thus, in order to measure local velocity, the lateral decorrelation rate needs to be assessed as a function of axial beam positions for the complete scan depth. It should be noticed that most of the computer simulation results were obtained over the large range of the near field

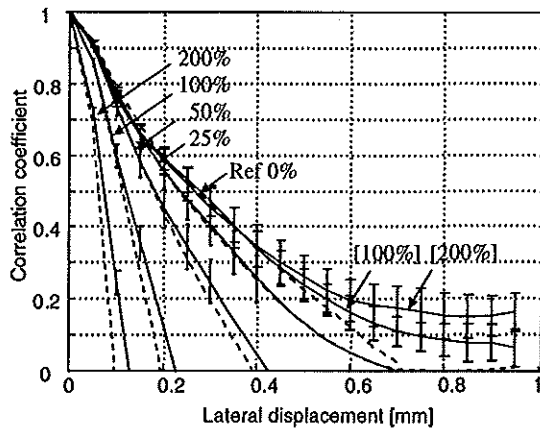


Fig. 7. The curves (indicated by [200%] and [100%]) simulated with only transverse velocity gradients showing little difference with the reference curve (0% velocity gradient). The correlation curves obtained with axial velocity gradients decrease rapidly as the gradient increases from 25% to 200%. The results predicted by the theoretical model in (2.4.1) are plotted in dotted lines

(0.5~4 mm). Assessment of the local beam decorrelation properties was not within the scope of this study.

The effect of the axial beam modulation is negligible in IVUS imaging due to an almost 90° angle between the ultrasound beam and the flow direction. Noise signals may bias decorrelation estimate. Since the lateral decorrelation function is reduced by a constant factor, a high noise level could be detected from the offset at the beginning of the correlation curve. Another solution to the noise problem is using the decorrelation measured in a stationary arterial tissue as a reference noise level; the noise decorrelation can be then deducted from the total decorrelation measured in moving blood. The change in the system bandwidth does not alter the lateral decorrelation function significantly, but increases measurement variations in decorrelation estimate. For the purpose of local velocity assessment, the decorrelation needs to be measured in a small range-gated window. The size of a correlation window should also be sufficiently small to reduce velocity differences in the correlation window in order to limit the error caused by the axial velocity gradient. The use of a small window with a limited number of data points, however, may induce high variations in correlation measurements. Thus, there is a trade-off in the window length between variations in decorrelation estimate and the resolution of velocity measurement or possible error caused by velocity gradients. Alternatively, several decorrelation values should be obtained for one window position to reduce the measurements variation.

For a time-delay estimator, echo decorrelation usually results in variation/jitter errors, which has an indirect effect as far as the corresponding peak value is still detectable. Decorrelation sources that are not related to the lateral displacement, however, will directly produce an overestimate in the velocity measurement using a decorrelation method. Thus, all the undesired decorrelation sources must be identified and excluded from the decorrelation-displacement calculation.

So far we have discussed the decorrelation properties of the IVUS beam assuming that the blood is a cloud of randomly distributed point scatterers. However, normally red blood cells tend to form clusters, a process called aggregation, and arrange themselves in "strings" called rouleaux. In the flowing blood, rouleaux are positioned along the direction of flow. The presence of RBC aggregation and rouleaux is a function of the cyclic variation of the local shear: regions of high shear (near static structures) have low aggregation and areas of low shear (near the center of the free lumen) have high aggregation (De Kroon et al. 1993). The shape and size of the backscattering particles may have a significant effect on the decorrelation phenomenon. For example, the echo from a single point scatterer moving across a beam will decorrelate faster than the echo arising from a long string of aligned scatterers moving across the same beam.

Therefore, the influence of the rouleaus on decorrelation estimate needs to be investigated.

The computer mode based on the impulse response method is able to delineate the complicated intensity distribution of the near field. The efficiency of the model in terms of computation time was improved by implementing the calculation of each scatterer response in the frequency domain. In principle, this modeling method can be used to study different types of IVUS transducers such as a phase array transducer from the extreme near-field up to the far-field. Knowledge of the lateral beam modulation obtained with the computer model will also provide important information for optimization of the RF lumen enhancement techniques.

## 6 CONCLUSION

Results of this study demonstrate that it is feasible to derive blood velocity from the original RF intravascular echo signals by means of decorrelation analysis. Localized velocity measurements require detailed assessment of the lateral decorrelation rate at different axial positions along the beam. To overcome the problem of the high variation in a small window, an approach for velocity estimation should be based on multiple assessments of the decorrelation of echo signals.

## 7 REFERENCES

1. Bonnefous O. Statistical analysis and time correlation processes applied to velocity measurement. *IEEE Ultrasonics Symp* 1989;887-892.
2. Bendat JS, Piersol AG. *Random data: Analysis and measurement procedures*. New York: Wiley-Interscience, 1983.
3. Céspedes I, Huang Y, Ophir J, Spratt S. Methods for estimation of subsample time delays of digitized echo signals. *Ultrasonic Imaging* 1995; 17:142-171.
4. De Kroon, MGM, Slager, CJ, Gussenhoven WJ, Serruys PW, Roelandt JRTC, Bom N. Cyclic changes of blood echogenicity in high-frequency ultrasound. *Ultrasound Med Biol* 1991;17:723-728.
5. Dickinson RJ, Hill CR. Measurement of soft tissue motion using correlation between A-scans. *Ultrasound Med Biol* 1982;8:263-271.
6. Dotti D, Lombardi R. Estimation of the angle between ultrasound beam and blood velocity through correlation functions. *IEEE Trans Ultrason Ferroelec Freq Contr* 1996;43:864-869.
7. Foster SG, Embree PM, O'Brien WD. Flow velocity profile via time-domain correlation: Error analysis and computer simulation. *IEEE Trans Ultrason Ferroelec Freq Contr* 1990;37:164-175.



8. Gronningsaeter A, Angelsen BAJ, Heimdal A, Torp H. Vessel wall detection and blood noise reduction in intravascular ultrasound imaging. *IEEE Trans Ultrason Ferroelec Freq Contr* 1996;43:359-369.
9. Gronningsaeter A, Angelsen BAJ, Gresli, A, Torp, H. Blood noise reduction in intravascular ultrasound imaging. *IEEE Trans Ultrason Ferroelec Freq Contr* 1995;42:200-208.
10. Hein A, O'Brien D. Current time-domain methods for assessing tissue motion by analysis from reflected ultrasound echoes-A review. *IEEE Trans Ultrason Ferroelec Freq Contr* 1993;40:84-102.
11. Li W, Gussenhoven, EJ, Zhong Y, The SHK, Pieterman H, van Urk H, Bom N. Temporal averaging for quantification of lumen dimensions in intravascular ultrasound images. *Ultrasound Med Biol* 20:117-122, 1994.
12. Li W, Van der Steen AFW, Lancée CT, Gussenhoven EJ, Bom N. Lumen enhancement and flow estimation by temporal correlation of radio frequency intravascular ultrasound. in *Proc 18th IEEE EMBS* 1996a.
13. Li W, Van der Steen AFW, Lancée CT, Gussenhoven EJ, Bom N. Temporal correlation of blood scattering signals in vivo from radiofrequency intravascular ultrasound. *Ultrasound Med Biol* 1996b;22:583-590.
14. Pasterkamp G, van der Heiden MS, Post MJ, Ter Haar Romeny B, Mali WPTM, Borst, C. Discrimination of intravascular lumen and dissections in a single 30 MHz ultrasound image: use of 'confounding' blood backscatter to advantage. *Radiology* 1993;187:871-872.
15. Stepanishen PR. Transient radiation from pistons in an infinite planar baffle. *J. Acoust. Soc. Am.*1971; 49:1627-1638.
16. Trahey GE, Smith SW, Von Ramm OT. Speckle pattern correlation with lateral aperture translation: Experimental results and implications for spatial compounding. *IEEE Trans Ultrasonics* 1986;3:257-264.
17. Wagner RF, Smith SW, Sandrik JM, Lopez H. Statistics of speckle in ultrasound B-scan. images. *IEEE Trans Ultrasonics* 1983;30:156-163.
18. Wagner RF, Insana MF, Smith SW. Fundamental correlation lengths of coherent speckle in medical ultrasonic images. *IEEE Trans Ultrasonics* 1988;35:34-44.
19. Zhang X, Shikutani M, Yamamoto K. Measurement of displacement and flow vectors with a single ultrasound beam using a correlation technique (II) - Computer simulation and basic experiments. *Techn Report IEICE* 1995;35:23-30.



## CHAPTER 9

---

# ESTIMATION OF LOCAL BLOOD VELOCITY AND VOLUME FLOW WITH INTRAVASCULAR ULTRASOUND

W. Li, A.F.W. van der Steen, C.T. Lancée, E.I. Céspedes,  
E. J. Gussenhoven, N Bom.

As partly been published in:

Velocity estimation with high frequency intravascular ultrasound. *In Proceedings IEEE Ultrasonics Symposium 1996.*



**ABSTRACT**

Current intravascular ultrasound techniques produce real-time imaging of a vessel cross-section with a scan plane normal to blood flow. When a cluster of randomly distributed blood particles moves across the ultrasound beam, the received echo signals decorrelate as a function of time. This phenomenon may be used to estimate blood velocities by measuring the decorrelation rate from a sequence of blood scattering signals. A decorrelation-based method for measuring local blood velocity and quantifying volume flow from cross-sectional radio frequency intravascular echo signals was developed. Serial *in vitro* measurements were performed with a flow phantom to test the principle of the proposed velocity estimate method. Measurements were also carried out *in vivo* in pig experiments to determine the usefulness of this method in clinical settings. Preliminary results of this study indicate that the proposed decorrelation method is able to extract cross-sectional velocity profiles and volumetric flow both *in vitro* and *in vivo*.

**1 INTRODUCTION**

Assessment of vessel dimensions simultaneously with other functional parameters such as blood velocity and volume flow is invaluable for assessing the severity of a stenosis. Current ultrasonic methods for measurements of blood velocity include Doppler processing and time domain correlation techniques (Censor et al. 1988; Hein et al. 1993; Hoeks et al. 1993). In general, both techniques are used to measure the axial velocity component (velocity along the ultrasound beam) of the blood flow, requiring that the ultrasound beam has a beam-to-flow angle  $\ll 90^\circ$ . An example of such a method is the forward looking intracoronary Doppler transducer mounted at the tip of a guide wire (Johnson et al. 1989; Tadaoka et al. 1990; Doucette et al. 1992; Di Mario et al. 1995). Doppler catheters provide an integrated measurement of velocity components from which the peak or mean velocity is usually extracted. The use of Doppler velocimetry alone, however, does not allow direct assessment of volumetric blood flow. For the purpose of measuring volumetric flow, the cross-sectional area and the velocity component of the flow normal (i.e., perpendicular) to the measurement plane must be assessed.

With the advent of intravascular ultrasound (IVUS) techniques that permit real-time imaging of a vessel cross-section, several studies have reported the combination/simultaneous use of intracoronary Doppler for velocity measurement and IVUS imaging for area measurement to obtain volumetric flow (Eichhorn et al. 1992; Grayburn et al. 1992; Chou et al. 1993; Isner et al. 1993; Sudhir et al. 1993). The velocity and area measurements obtained by combining these two techniques, however,

cannot be obtained simultaneously from the same arterial cross-section due to intrinsic spacing between the Doppler and imaging transducers. The inability to assess the hemodynamic variables coincidentally in time and space could limit the simplicity and clinical applicability of these methods. Additionally, multiple catheter approaches suffer from possible interference between devices: for example, the Doppler transducer may create harmonic interference that results in cross-talk on the IVUS image. Thus, a means of extracting blood flow velocity directly from IVUS data may provide a better approach for assessment of morphologic data and volumetric flow over the same arterial cross-section.

Unlike other medical imaging techniques, one feature of IVUS imaging is that the ultrasound beam is normally oriented almost perpendicular to the blood flow; the majority of the flow stream, therefore, consists of transverse velocity components (velocity across the ultrasound beam). The presence of transverse velocities is one main cause for decorrelation of the received echo signals as blood scatterers move across the ultrasound beam. Earlier studies with a 30 MHz IVUS imaging system have documented the time-varying characteristics of blood scattering in vivo (Li et al. 1995, *Chapter 6*; Li et al. 1996a). Several groups (Pasterkamp et al. 1993; Li et al. 1994&1995, *Chapter 6&7*; Gronningsaeter et al. 1995, 1996) have demonstrated that rapid changes in blood echoes can be used to improve the IVUS image quality by suppressing/enhancing the echo intensity of blood. When excluding other non-motion related decorrelation factors, decorrelation of echo signals is related to the axial and lateral velocities of the ultrasound medium. Dickinson et al. (1989) reported a decorrelation based method for tissue motion detection. Zhang et al. (1993) and Dotti et al. (1996) incorporated the decorrelation measurement to estimate the beam-to-flow angle on the scan plane in order to retrieve the true blood velocity vector.

The goal of this research was to develop an approach to extract flow information from cross-sectional IVUS data. In our earlier computer simulation studies, the decorrelation properties of a circular IVUS transducer have been investigated (Li et al. 1996b, *Chapter 8*). This paper presents a radio frequency (RF) processing method for measuring local blood velocity and quantifying volume flow by means of decorrelation estimation. The principle of the decorrelation-based velocity estimation is discussed. A series of in vitro experiments was performed to test the proposed method. Finally, results of in vivo evaluation will be given.

## 2 PRINCIPLES

The geometric relationship between blood flow and the IVUS imaging catheter is illustrated in Fig. 1. The coordinate system is set with reference to the central axis of

the ultrasound beam (z-axis) and the catheter axis (x-axis). One commonly used IVUS imaging method comprises a single rotating transducer system with a flexible drive shaft. Cross-sectional data are scanned by rotating the transducer at a constant speed along the imaging plane (y-axis). In this study, the velocity vector perpendicular to the ultrasound beam and across the imaging plane ( $V_x$ ) is termed the *transverse* velocity, which corresponds to the *lateral* displacement

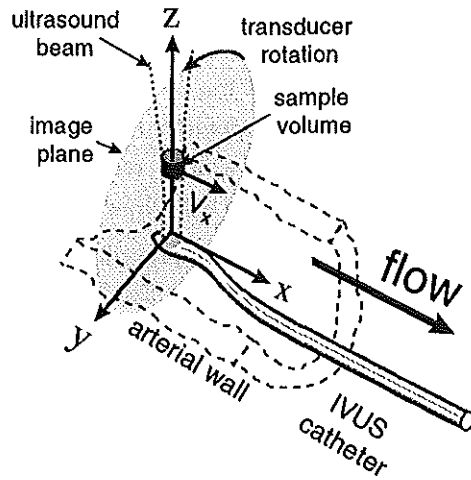


*Fig. 1. The coordinates of the IVUS imaging setup. The z-axis represents central axis of the ultrasound beam. the catheter axis is along the x-axis and the imaging plane is along the y-axis.*

of blood scatterers. The transverse velocity represents the direction of the main stream of blood flow and is estimated by means of a decorrelation procedure. The velocity vector along the ultrasound beam axis ( $V_z$ ) is termed the *axial* velocity. This velocity component is usually smaller than the transverse velocity due to a nearly  $90^\circ$  beam-to-flow angle. The axial velocity can be measured by the time shift of the RF echo signal. The transducer velocity ( $V_y$ ) is determined by the scanning speed of a mechanical IVUS system.

In general, the direction of flow can have any arbitrary angle with respect to the reference axis of the ultrasound beam, resulting in a three-dimensional velocity vector. However, in common practice the angle between the catheter axis and the flow direction is usually very small. Finet et al. (1993) demonstrated that this angle could hardly exceed  $10^\circ$  for both coronary and peripheral arteries. Assuming a worse case beam-to-flow angle of  $75^\circ$  (an angle of  $15^\circ$  between catheter and flow), the contribution of the axial velocity to the total velocity in flow estimation is lower than 4%. Since this level of error is well within the required parametric resolution in practice, volumetric flow can be directly derived from the transverse velocity and the contribution of other flow velocity components may be neglected.

## 2.1 Decorrelation estimation method

The decorrelation of the received IVUS signals as a function of time can be evaluated from a sequence of  $N$  RF traces ( $S_1 \dots S_N$ ) acquired at a fixed time interval  $T_s$  as determined by the pulse repetition rate. The received RF signals with zero mean amplitude are range-gated with a rectangular window of length  $L_w$ . The signal decorrelation is estimated with the following steps:

The first step is a phase matching procedure that aligns the windows of  $S_2 \dots S_N$  with that of  $S_1$ . Because of the presence of an axial velocity component, the RF traces are shifted in time as illustrated in Fig. 2a. The time shift between two consecutive RF traces in the range window is measured by determining  $\delta T$  where the cross-correlation function reaches maximum. After obtaining a set of  $\delta T_i$  ( $i=2, \dots, N$ ), each RF window in trace  $S_i$  is shifted by  $\sum \delta T_k$  ( $k=2, \dots, i$ ) to line up with the first window (Fig. 2b). The mean time shift measured at this window position is  $\overline{\delta T}$ .

In the second step, the correlation coefficient  $\rho_{i,j}$  between trace  $S_i$  and  $S_j$  in the aligned RF windows is calculated for different combinations of  $i$  and  $j$ :

$$\rho_{i,j} = \frac{\sum_{k=1}^K S_i(k) S_j(k)}{\sqrt{\sum_{k=1}^K [S_i(k)]^2 \sum_{k=1}^K [S_j(k)]^2}} \quad i=1,2 \dots N-1, j=2 \dots N, \quad (2.1.1)$$

where  $K$  is the maximum overlapping window length after the phase alignment defined as:  $K = N_j - N_i(N-1)$ .  $N_l$  and  $N_i$  are the corresponding number of samples in  $L_w$  and  $\overline{\delta T}$ , respectively. Excluding points outside the overlapping range ensures that correlation values are measured from the signals of the same scattering volume. The correlation coefficient between two traces separated by an interval of  $m = (j-i) * T_s$  are evaluated by averaging all the available measurements:

$$\rho_m = \frac{\sum_{k=1}^{N-m} \rho_{k,k+m}}{N-m} \quad m=1,2 \dots N-1. \quad (2.1.2)$$

Finally, a linear model is fitted to the discrete correlation values  $\rho_m$  ( $m=1 \dots N-1$ ), yielding a continuous correlation curve as a function of time:

$$\rho(t) = 1 - \alpha t. \quad (2.1.3)$$

In the following analysis, the slope  $\alpha$  is termed as the *decorrelation slope* that characterizes the decorrelation procedure as a function of either time or displacement.

For each range-gated window, the decorrelation slope  $\alpha$  and the mean time shift  $\overline{\delta T}$  of the RF sequence are measured to obtain local, adjacent estimates. An example of time shift and decorrelation for a series of  $N=5$  echo signals is shown in Fig. 2c.



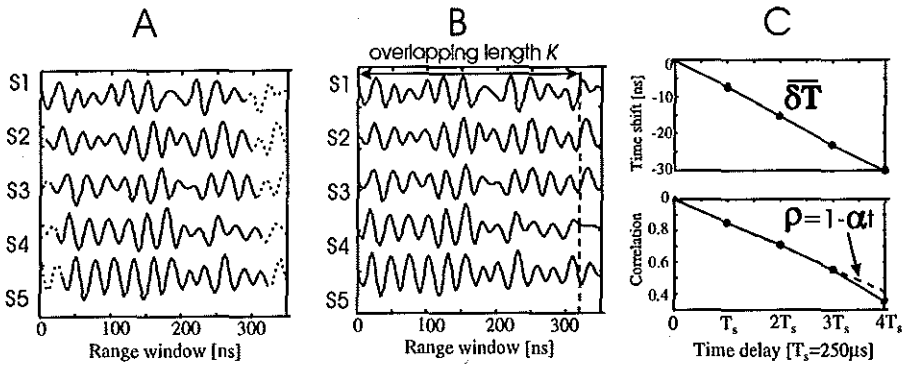


Fig. 2. A) Range-gated window showing the time shift in 5 RF traces. B) Result of RF traces lined up by the phase matching procedure. C) Time shift (upper panel) measured as a function of time delay in units of  $T_s$ . The mean time shift  $\overline{\delta T}$  is derived from the averaged value of individual measurements. The correlation values (lower panel) obtained at different time delay are fitted with a linear model (dotted line) to derive the decorrelation slope  $\alpha$ .

## 2.2 Estimation of velocity distribution along a radius

In a computer simulation study (Li et al. 1996b, Chapter 8), we have demonstrated that the RF signals from scatterers moving across the near field of an ultrasound beam

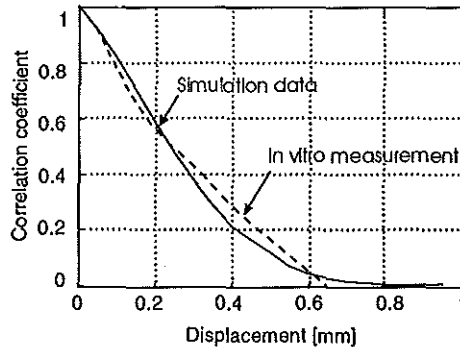


Fig. 3. Typical lateral decorrelation curves obtained with a computer model (solid line) and in vitro measurements (dotted line). The computer simulated curve was derived in the near field (0.5~4 mm) of an circular IVUS transducer (transducer diameter: 1mm, frequency: 30 MHz, bandwidth: 20 MHz). The in vitro curve was measured at the beam position of 2-3 mm using the contrast agent as ultrasonic scattering medium. Both curves show a monotonous decrease of correlation with the increase of the lateral displacement in an approximately linear manner.

decorrelate monotonously and approximately linearly with displacements. Data obtained with a dedicated in vitro experimental setup (described later) show a similar lateral decorrelation curve as the previously simulated result (Fig. 3). Based on these observations, a decorrelation-to-velocity estimate approach has been developed that consists of the following steps:

1) *Calibration step.* In a controlled experimental environment, the decorrelation of the ultrasound beam at the  $i$ th axial window position is characterized with a linear model (Fig. 4a):

$$\rho_i = 1 - \alpha_i^x \Delta x, \quad (2.2.1)$$

where  $\rho_i$  is correlation output,  $\Delta x$  is the lateral displacement and  $\alpha_i^x$  is the displacement decorrelation slope that is a characteristic of the IVUS transducer used. Since the beam intensity may change significantly in the near field,  $\alpha_i^x$  is a range dependent factor that requires to be calibrated by a controlled experiment.

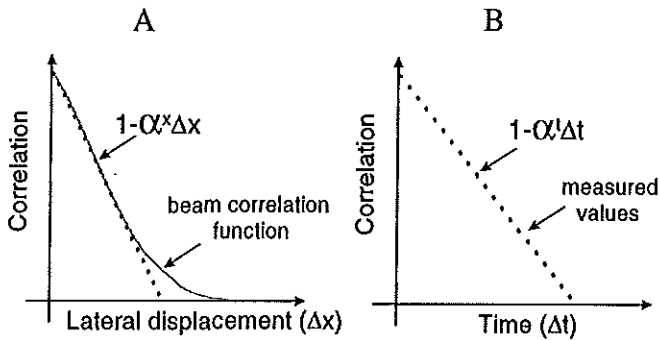


Fig. 4. Illustration of the decorrelation-to-velocity procedure. A) Beam decorrelation as a function of the lateral displacement at a given range distance of the transducer (solid line). This function, which can be estimated by experiment or theory, is approximated with a linear model to obtain the displacement decorrelation slope  $\alpha^x$ . B) Decorrelation values measured at a fixed time interval (dots). A straight line is fitted through the measured points to obtain the time decorrelation slope  $\alpha^t$ .

2) *Measurement step.* At each scan angle, a sequence of RF traces is acquired at high pulse repetition rate with a known time interval  $T_s$ . Using the procedure described in (2.1.1)-(2.1.3) the time decorrelation slope  $\alpha_i^t$  at the  $i$ th window can be measured (Fig. 4b):

$$\rho_i^t = 1 - \alpha_i^t \Delta t. \quad (2.2.2)$$

3) Ignoring decorrelation components that are not related to the lateral displacement of blood scatterers in the measurement step,  $\rho_i$  and  $\rho_i'$  are related by the transverse velocity  $V_x$ . Equating  $\rho_i$  in (2.2.1) with  $\rho_i'$  in (2.2.2), we obtain

$$V_x(i) = \Delta x / \Delta t = \alpha_i' / \alpha_i^x. \quad (2.2.3)$$

Equation (2.2.3) indicates that the transverse velocity can be estimated from the ratio between the *calibrated* decorrelation slope [ $\text{mm}^{-1}$ ] and the *measured* decorrelation slope [ $\text{s}^{-1}$ ].

The axial velocity is derived from the mean time shift  $\overline{\delta T}$  measured by the phase matching procedure:

$$V_z(i) = \frac{c \overline{\delta T}_i}{2T_s}, \quad (2.2.4)$$

where  $c$  is the sound velocity and  $T_s$  is the pulse repetition rate.

### 2.3 Volume flow quantification

Velocity measurements along a radius can be repeated at adjacent angular positions in a scan plane to measure the velocity distribution over the entire lumen cross-section. The 2D profile is represented as  $V_x(\theta, r)$  in a polar coordinate system. The volumetric flow can be calculated by integrating the local transverse velocity with the area element over the complete vessel cross-section:

$$Q = \sum_A V_x(\theta, r) \Delta A(\theta, r) = \Delta r \Delta \theta \sum_{\theta=1}^{N_\theta} \sum_{r=1}^{R(\theta)} V_x(\theta, r) R(r), \quad (2.3.1)$$

where  $R(r)$  is the radial distance at index  $r$ ;  $N_\theta$  is the number of angular measurements and  $R(\theta)$  is a radial definition of the lumen boundary at angular index  $\theta$ . The resolution of the flow mapping is determined by  $\Delta \theta$  and  $\Delta r$ , which are the scanning step sizes in the angular and radial measurements, respectively. The mean velocity is calculated from the lumen cross-sectional area  $CSA$  with:

$$V_{mean} = Q / CSA. \quad (2.3.2)$$

As discussed earlier, the axial velocity component has a much lower value than the transverse velocity in the IVUS application, and therefore only transverse velocities are considered in (2.3.1) for estimation of the flow volume.

### 2.4 Compensation of transducer velocity

The rotation of the transducer during real-time imaging induces an additional displacement of the ultrasound beam along the  $y$ -axis in relation to blood scatterers. The measured transverse velocity is therefore the combined value of the blood velocity  $V_x$  and transducer velocity  $V_y$  vectors. If the transducer has a perfect circular shape, a

lateral displacement along the x or y directions will have the same decorrelation effect. The transducer used in this study, however, has an elliptical surface with the long axis in x direction and short axis in y direction. In this case, the decorrelation rate along the y-axis could probably be higher than the x-axis; a correction factor is needed in calculation of the combined transverse velocity  $\tilde{V}_t(i)$ :

$$\tilde{V}_t(i) = \sqrt{[V_x(i)]^2 + [\beta V_y(i)]^2}, \quad (2.4.1)$$

where  $V_y(i)$  is the transducer velocity at the  $i$ th window as determined by the frame rate  $F_r$  and the radial distance  $R(i)$ :  $V_y(i) = 2\pi F_r R(i)$ . The coefficient  $\beta$  is the correction factor that accounts for a different decorrelation rate in the y-axis and needs to be calibrated. The transverse flow velocity can be extracted from the measured velocity by

$$V_x(i) = \sqrt{[\tilde{V}_t(i)]^2 - [2\pi\beta F_r R(i)]^2}. \quad (2.4.2)$$

## 2.5 Velocity mapping by combining axial velocity measurements

Correlation estimation of local velocity using a small window may have a considerable amount of variations. At the expense of spatial resolution, one approach to solve this problem is averaging the flow data along the angular and radius directions. An alternative approach is to combine the axial and transverse velocity measurements. Because the beam-to-flow angle is typically close to but slightly different from an absolute value of  $90^\circ$ , an axial velocity component can be detected by the phase shift. Since the axial velocity estimates exhibit less variability than the corresponding transverse velocity estimates, it may be advisable to utilize the axial velocity whenever possible.

The two velocity components  $V_x(i)$  and  $V_z(i)$  measured in the  $i$ th window are related by the beam-to-flow angle  $\theta$  as:

$$\cot(90^\circ - \theta) = \frac{V_x(i)}{V_z(i)}. \quad (2.5.1)$$

Because the beam-to-flow angle  $\theta$  is constant for all adjacent windows along a radius, the ratio of the transverse and axial velocities can be estimated from their mean values:

$$\kappa = \cot(90^\circ - \theta) = \frac{\bar{V}_x}{\bar{V}_z} \quad (2.5.2)$$

Then, the local velocity distribution along a radius can be reconstructed from the shape of the axial velocity profile  $V_z(i)$  and the velocity ratio  $\kappa$ :

$$\hat{V}(i) = \kappa V_z(i). \quad (2.5.3)$$

Expression (2.5.3) indicates that the local transverse velocity distributions can be obtained from the axial velocity profiles using  $\kappa$  as a scaling factor

### 3 EXPERIMENT MATERIALS AND METHODS

**IVUS imaging system:** Ultrasonic data were acquired using a 30 MHz IVUS imaging system (Du-MED, Rotterdam, The Netherlands) with a single-element transducer mounted on the tip of a 4.3 F catheter. The bandwidth of the system was 20 MHz, yielding an axial resolution of approximately 75  $\mu\text{m}$ . The image scanning rate was 16 frames per second.

**Velocity measurement:** For the subsequent in vitro/vivo data (except for in vitro experiment I), the length of range-gated windows  $L_w$  was set to 260  $\mu\text{m}$  (70 data points at 200 MHz sample frequency), which was approximately 5 times the wave length (round trip). The velocity profile measurement was performed by moving the range window along a radius at a step of 185  $\mu\text{m}$  (50 samples, 30% overlapping). RF data were interpolated to obtain a time resolution of 1ns in the phase matching procedure. The cross-sectional velocity data were averaged using a 3 by 3 low pass filter for color mapping display.

#### 3.1 In vitro experiments

**Flow phantom:** To study the relationship between the RF correlation and flow velocities, a setup consisting of a 40 cm long circular plastic tube phantom and a pump were used to generate a stable parabolic flow (Fig. 5). The inner diameter of the tube was 4 mm. The flow rate was controlled by a valve and measured with an electromagnetic flowmeter. The mean flow velocity was calculated from the tube cross-sectional area (catheter area was deducted when the catheter was inside the tube)

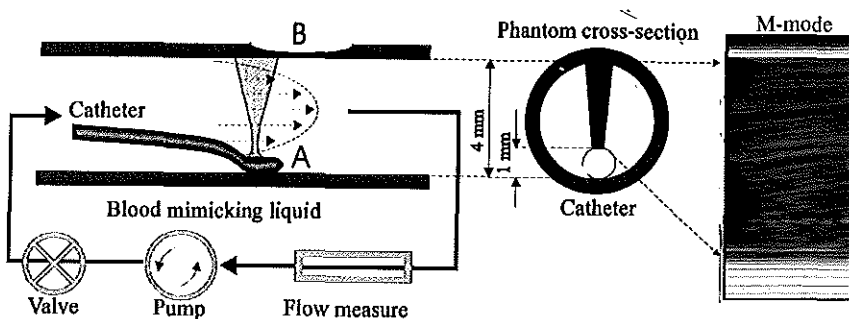


*Fig. 5. Illustration of RF data acquisition for in vitro experiment setup. The contrast agent was used for blood mimicking. The catheter was positioned either inside the tube (A) or outside the tube (B). A small part of the tube wall (B) was made thinner to allow the penetration of ultrasound beam. An example of the acquired RF sequence is displayed as M-mode image on the right.*

and the readout of the flowmeter. Water with ultrasound contrast agent (Quantison™, Andaris) in concentration of  $7.5 \times 10^9$  particles/liter was used as a blood-mimicking fluid.

**Data acquisition:** The orientation of the transducer was carefully adjusted in a way that the distance of the tube wall was maximum and the echo amplitude of the wall reflection was optimal. The received RF signal was amplified 40 dB by the amplifier of the imaging system and digitized by a dual channel digital oscilloscope (LeCroy 9400, Chestnut Ridge, NY, USA). To avoid jitter between RF traces, the pulse generator was synchronized with the internal sampling clock of the oscilloscope. The acquisition parameters for in vitro measurements are listed as follows:

- sample frequency: 200 MHz
- sample duration: 10  $\mu$ s (2000 samples)/trace
- pulse repetition rate: 4 KHz ( $T_s = 250 \mu$ s)
- RF traces per angle: 30 traces/angle.

For analysis of variability, the data acquisition was repeated 5 times at each flow setting. The mean values and standard deviations were calculated from these repeated measurements.

**In vitro experiment I: Relationship between decorrelation and flow:** This experiment was designed to verify the hypothesis that the decorrelation of an RF sequence acquired at a fixed angle is related to the mean flow velocity. Decorrelation measurements were performed with the IVUS catheter positioned inside the tube. The mean flow velocities were set from 0.1 to 50 cm/s in steps of 2.5 cm/s. At each flow setting, the time decorrelation slope ( $\alpha'_i$ ) was measured from 30 RF traces using the decorrelation method. The measurement window was positioned at 1.5 mm (the center point between the transducer and tube wall) and the window length was 1 mm (in this experiment only).

**In vitro experiment II: Calibration of transducer decorrelation:** In order to calibrate the decorrelation properties at each axial position, the catheter was placed outside the tube to obtain an undisturbed parabolic velocity profile, which allowed reconstruction of velocity distributions from the flow measurements. Measurements were performed at 4 different flow settings (mean velocities of 8~22 cm/s). The calibration procedure was performed in three steps: First, the time decorrelation slope at each range-gated window ( $L_r=260 \mu$ m) was obtained from the mean of the 5 repeated measurements. Secondly, the corresponding lateral displacement of the range

window was calculated from the velocity estimated from the parabolic profile. With the calculated displacement value, the time decorrelation slope [ $s^{-1}$ ] was converted to the displacement slope [ $mm^{-1}$ ]. By taking the mean of the measurements of the 4 flow settings, a set of displacement decorrelation values was obtained at different radial positions from 1 to 3 mm. Measurements from the two edge parts were excluded because of high velocity gradients and strong ring-down effects. In the third step, the calibrated displacement decorrelation slope ( $\alpha_i^x$ ) as a function of the beam position was obtained by fitting a nonlinear curve through the data points.

**In vitro experiment III: Velocity measurement in a radius:** This experiment was designed to test the decorrelation method for measurement of the local velocity along one radius. Velocity measurements were performed at 6 different flow settings (mean velocities of 3~18 cm/s) with the catheter placed inside the tube. The transverse velocities were measured according to (2.2.3) with the calibration curve obtained in experiment II. The flow velocity profiles were obtained by combining the transverse and axial velocity measurements according to (2.5.3).

**In vitro experiment IV: Flow measurement in a cross-section:** A stepper-motor device was used to rotate the transducer for acquisition of cross-sectional RF data. Four scans were acquired at flow rates between 1 and 3 ml/s with mean velocities from 8.9 to 27 cm/s. The flow value was calculated with the cross-sectional velocity distribution according to (2.3.1) and compared to the readout of the flow meter.

### 3.2 In vivo experiment

**In vivo data acquisition:** In vivo experiments were performed in the iliac artery of Yorkshire pigs. The system used in vitro did not allow real-time cross-sectional RF data acquisition because of the limitation in memory capacity. To acquire real-time cross-sectional RF data in vivo, a PC based acquisition system has been built with a 500 MHz waveform digitizer and a fast memory board (Signatec, Corona, CA, USA). The system is capable of digitizing RF data at 200 MHz sample frequency and storing in real-time up to 128 Mbytes of RF data in the memory board. The large memory capacity enables acquisition of a sequence of RF cross-sectional frames from a number of cardiac cycles. The acquisition parameters for in vivo measurements are listed as follows:

- sample frequency: 200 MHz
- sample duration: 10  $\mu s$  (2000 samples/line)
- pulse repetition rate: 15.6 KHz ( $T_s = 64 \mu s$ )

- scan lines: 1000 lines/frame
- frame rate: 16 frames/second.

During the experiments, the echo catheter was advanced through a 7F sheath into the iliac artery. At the site of interest, a total of 60 RF frames was acquired, yielding a measurement period of 3.75 seconds. The original 1000 scan lines were grouped into 200 sequences with 5 RF traces per sequence. Due to lack of internal clock synchronization, the accuracy of the time shift measurement was limited by the jitter between RF traces. The axial velocity measurements were not included in the in vivo experiment. The flow data and velocity mapping were obtained only with the transverse velocity components measured by the decorrelation method.

Because calibration for the decorrelation along the y-axis was not available at the time of this experiment, the transducer velocity was compensated with  $\beta=1$  in (2.4.2). Assuming a smaller diameter may have a faster decorrelation rate, this could probably undercompensate  $V_y(i)$ , resulting in an overestimate of the flow velocity.

## 4 RESULTS

### 4.1 In vitro experiments

**In vitro experiment I:** Fig. 6 plots the measured decorrelation slope as a function of the mean flow velocity. The decorrelation value increases as the flow rate increases by an almost linear relationship with a zero offset (linear regression:  $y=0.01x-0.012$ ,  $r=0.99$ ,  $p \ll 0.0001$ ). This curve demonstrates that the decorrelation of the RF sequences is closely related to the transverse velocity. The use of a decorrelation slope is suitable to quantify the decorrelation procedure induced by the lateral displacement of scatterers, thus providing the basis for the decorrelation-to-velocity method.

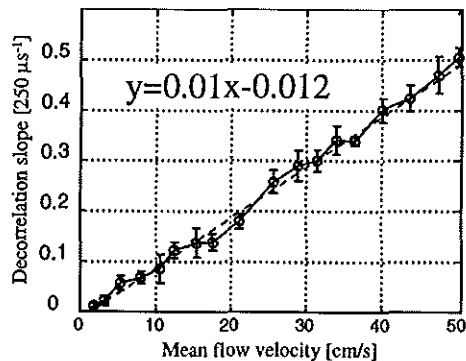


Fig. 6. The curve of the measured decorrelation slope (in units of time interval  $T_s$ :  $[250 \mu\text{s}]^{-1}$ ) and the flow velocity showing a linear dependency of the two variables. The linear fit was plotted as a dotted line.



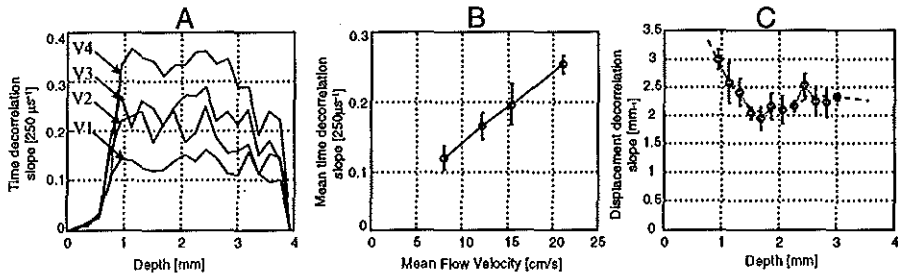


Fig. 7. A) The curves of the time decorrelation slope (in units of time interval  $T_s$ : [250  $\mu\text{s}^{-1}$ ]) measured as function of the depth for 4 different flow settings. High variations in decorrelation measurements can be observed. B) Mean values by averaging the entire radial range showing a linear relation to the flow velocity. C) The values of the displacement decorrelation slope [mm]<sup>-1</sup> obtained by converting the time and velocity to the displacement. The data points averaged over the 4 measurements of V1~V4 were fitted with a nonlinear model to obtain a calibration curve as a function of the depth (dotted line).

**In vitro experiment II:** Fig. 7a depicts that the values of the time decorrelation slope increase with an increase of the mean flow velocities but shows a considerable amount of variations over the measurement depth. Parabolic distributions were not evident because the curves were modulated by the beam dependent decorrelation factor. In Fig. 7b, the plot of the mean slope values averaged over the entire measurement depth as a

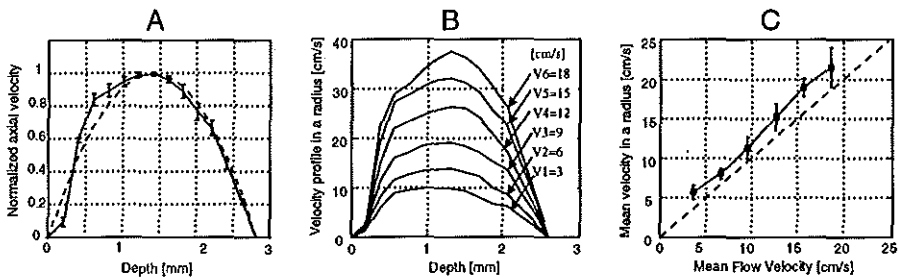
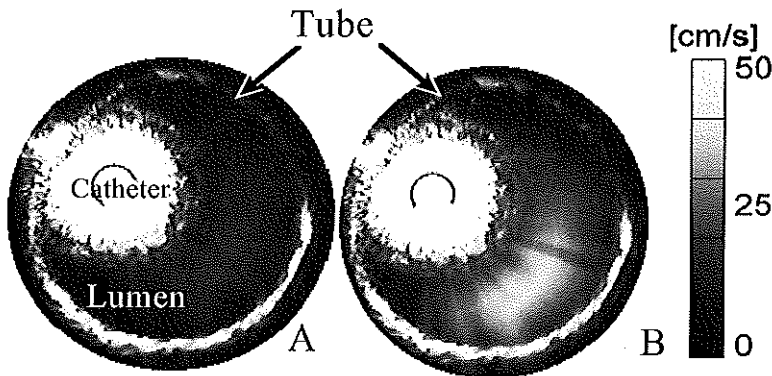


Fig. 8. A) The normalized axial velocity showing a similar distribution as a parabolic curve (dotted line). The distribution curve was obtained from 6 velocity settings and normalized by the maximum value. B) Velocity profiles derived from the axial velocities and scaled with the corresponding  $\kappa$  values. C) Mean transverse velocities measured from the entire radius showing a linear relation to the flow velocity. The measured mean velocity values in the radius are consistently higher than the mean cross-sectional velocities calculated from the flow rate.

function of the flow velocities confirms the linear relationship observed in experiment I. The calibration curve derived by nonlinear fitting is shown in Fig. 7c. The displacement slope was in the range of  $2 \sim 3$  [ $\text{mm}^{-1}$ ], corresponding to a half correlation length of  $0.33\sim 0.5$  mm. Higher decorrelation rates were observed in the extreme near field probably caused by the rapid changes in ultrasound intensity.

**In vitro experiment III:** The distribution of normalized axial velocities obtained from 6 flow settings shows a trend comparable to a parabolic velocity profile (Fig. 8a). The curve was distorted in the region close to the transducer due to the strong ring-down interference. Standard deviations in the local axial velocity measurements were low. The velocity profiles derived by combining the transverse and axial velocity measurements at each flow setting depict a class of reproducible curves with values increased accordingly with the mean velocities (Fig. 8b). The scaling factor derived from the mean transverse and axial velocities was measured  $\kappa=7.6 \pm 0.6$  (Mean  $\pm$  SD) for all velocity settings.

The mean transverse velocities estimated from the entire radius increase linearly with the mean flow velocities, but are higher than the flow settings (Fig. 8c). This bias is due to the insertion of the catheter inside the tube, which causes a flow redistribution at the measurement cross-section; higher velocities are expected to be found in the region that has a longer radius between the transducer and the wall. Standard deviations of the mean velocity measurements were about 10% of the mean values.



*Fig. 9. In vitro color flow mapping images obtained at low (A) and high (B) velocity settings. The cross-sectional velocity profiles were derived from the axial velocity distribution. The color scaling bar was determined by the ratio between the mean transverse and axial velocities.*

**In vitro experiment IV:** Fig. 9 shows the cross-sectional velocity profiles derived from the RF scans and color-mapped with the IVUS image data. The cross-sectional velocity profiles were derived from the axial velocity distribution. The color scaling bar was determined by the ratio between the mean transverse and axial velocities. High velocities were observed on the central regions with a longer radius towards the transducer. The flow rates measured from cross-

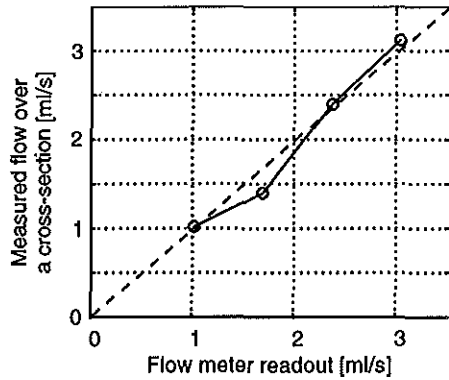


*Fig. 10. Flow rates estimated from the cross-sectional RF velocity data showing a good agreement with readouts of the flow meter*

sectional velocity data show a good agreement with the flow readings (Fig. 10). The paired differences between the measured values and the flow readouts were  $0.1 \pm 0.3$  ml/s (Mean  $\pm$  SD), which was approximately 4% of the mean flow rate.

#### 4.2 In vivo experiment

The IVUS image with color flow mapping is shown in Fig. 11. Pulsatile parabolic-like velocity profiles can be observed. The cross-sectional velocity distribution is similar to the in vitro results (Fig. 9). The flow volume curve shows a reproducible cyclic change in the range of 1~3 ml/s in accordance with the cardiac cycle. The mean cross-sectional velocities change from 20 cm/s to 70 cm/s between diastole and systole, which is in the range of common peripheral flow velocities in pigs. The variations in the peak of the flow measurements are partly due to the limited frame rate that undersamples the rapid changing flow curve.

## 5 DISCUSSION

A method to extract cross-sectional velocity distributions and volumetric flow from intravascular ultrasound data has been developed. Unlike Doppler velocimetry where flow is derived from the maximum/mean velocities and assumed flow profiles, the decorrelation method allows flow measurement at all points in a cross-section. Thus, no assumptions are made concerning the shape of the lumen area or prior knowledge of velocity profiles. Since the area of integration and the flow velocity are computed from

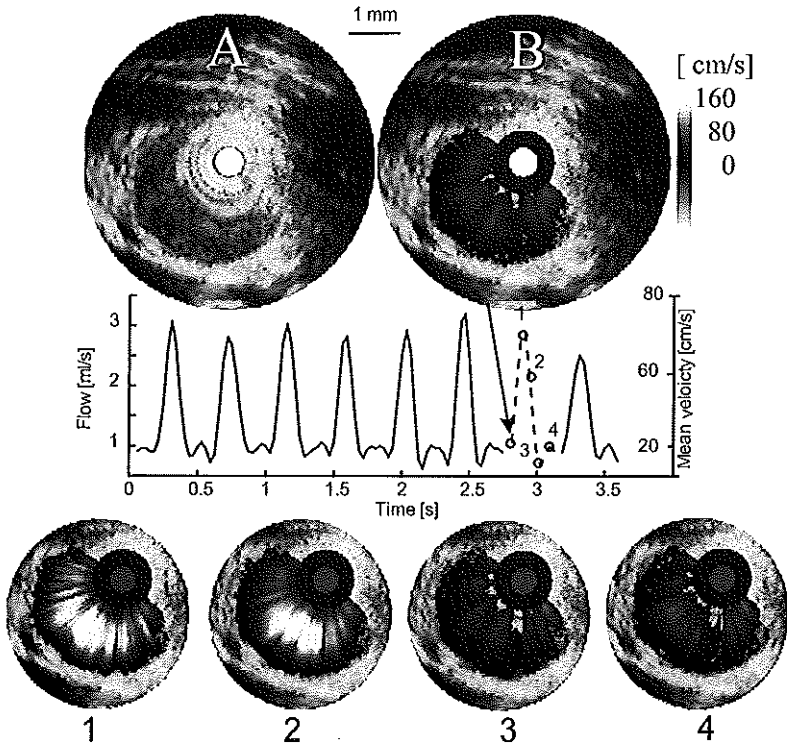


*Fig. 11. IVUS image (A) with color flow mapping (B) obtained in vivo showing the potential of the decorrelation method for velocity profile display and flow volume measurement. The upper panel shows the original echo image and the image with color velocity display. The volume flow (left y-axis) is plotted as a function of time in the middle panel, showing cyclic changes of the flow curve, and the corresponding mean velocity is displayed on the right y-axis. To demonstrate the changes of the cross-sectional velocity distributions over a cardiac cycle, the flow images obtained at the cardiac phase 1-4 are displayed on the bottom panel (see color pictures on the cover).*

the same signals, the derived vessel dimensions and flow information are obtained simultaneously and in place.

The approximately normal angle between the flow direction and the scanning plane in IVUS imaging, on one hand, limits straightforward application of a conventional ultrasonic method for velocity estimates. On the other hand, this unique geometric configuration allows assessment of blood volume flowing through the imaging plane. The relatively fixed geometric relationship between blood flow and ultrasound beam

avoids errors caused by an undetermined beam-to-flow angle encountered in many clinical applications of ultrasonic flow measurements.

Decorrelation of echo signals is a complex process that is not only related to motion, but also associated with other decorrelation sources. Several decorrelation sources have been addressed for error analysis of time delay estimates with correlation techniques (Bonnefous et al. 1986; Foster et al. 1990). In our earlier computer simulation study, we have investigated the influence of a number of factors on estimates of the lateral displacement using a decorrelation method (Li et al. 1996b, *Chapter 8*). For example, electronic noise in the echo signals results in decorrelation. Two echo signals can differ only due to corruption of independent realizations of the noise source. The non-motion-related decorrelation must be isolated in order to obtain an unbiased velocity estimate. Estimation of velocity with a single decorrelation value, therefore, is very sensitive to errors caused either by other sources of decorrelation that are not related to motion or high variations in range-gated correlation measurements (this is discussed next). An important feature of the described method is the use of multiple decorrelation values to improve both the accuracy and precision of the velocity measurements. The correlation values measured with a sequence of RF traces provide information of a decorrelation curve at various time delay; this permits analysis of the decorrelation procedure as a complete curve instead of a single value at a specific delay. The use of a decorrelation slope by linear fitting integrates the multiple correlation values effectively to provide a quantitative assessment of decorrelation. This approach is expected to be less sensitive to noise signals because at a given noise level, the slope of a decorrelation curve is affected less than individual decorrelation points (Li et al. 1996b, *Chapter 8*).

The axial spatial resolution of flow mapping is determined by the size of a range-gated correlation window; a small window is mandatory in order to assess local flow velocities. Using a small sampling volume also reduces the error induced by velocity gradients/variations within the resolution cell. A decrease of the size of the range window increases the measurement variations in the decorrelation estimation. Results of our computer simulation indicate the degree of the variations is inversely proportional to the term:  $\sqrt{BT}$ :  $B$  is the bandwidth of the imaging system and  $T$  is the time of the range cell. For the window size (260  $\mu\text{m}$ ) used in this study, the variations in individual correlation measurements may reach a value as high as 40% ( $B=20$  MHz,  $T=350$  ns). This further explains why a multiple correlation approach is essential to obtain reliable decorrelation measurements for velocity estimation. Since the volumetric flow is derived from integration of the velocity data over the entire cross-section, a lower variability is expected. For the display of velocity profiles, the combination of the axial velocity distribution with the gain controlled by the mean

velocity ratio provides an alternative approach to obtain a more precise color flow mapping. Variations in estimation of the velocity ratio are effectively reduced with the use of the mean transverse and axial velocities over an entire radius. This approach, however, will highly depend on the availability of accurate measurements of axial velocities. When the axial velocity is not detectable due to an absolute  $90^\circ$  beam-to-flow angle, the velocity profiles can still be mapped with the transverse velocity measurements. As demonstrated by results of the *in vivo* study where velocity profiles were mapped only with transverse velocities, the absence of axial velocity measurements will not impose fundamental limitation on the decorrelation-based method.

For echo data acquired at a fast pulse repetition rate, the arterial tissue can be considered as a static structure. Thus, the decorrelation computed in the stationary tissue is very likely caused by non-motion-related decorrelation source such as noise. A possible approach to improve the current method is to use the decorrelation value of tissue echoes as a baseline measurement of noise. Assuming that blood and tissue echo signals have a similar noise level, the tissue decorrelation can be deducted from the total decorrelation of moving blood to remove the influence of some undesired decorrelation interference.

## 6 CONCLUSIONS

We have presented a decorrelation based method that provides a unique opportunity to measure local blood velocities and volumetric blood flow at the scanning plane of the cross-sectional IVUS image. The simultaneous display of morphologic data together with flow information may allow integration of structural and functional information for the assessment of the atherosclerotic diseases with improved visualization of tissue components.

Results of *in vitro* experiments demonstrate that the decorrelation method can achieve local measurement of blood velocity over a complete vessel cross-section with sufficient spatial resolution for color flow mapping. Volumetric flow estimated from the cross-sectional velocity profiles correlates well with the readouts of an independent flowmeter. Preliminary *in vivo* experiments performed with a commercial imaging system demonstrate the feasibility of applying this method in patients. Further validation studies are needed in order to evaluate the accuracy and reproducibility of this method.

## 7 REFERENCES

1. Bonnefous O. Statistical analysis and time correlation processes applied to velocity measurement. *IEEE Ultrasonics Symp* 1989;887-892.
2. Censor D, Newhouse L, Vontz T, Ortega HV. Theory of ultrasound Doppler-Spectra velocimetry for arbitrary beam and flow configurations. *IEEE Trans Biomed Eng* 1988;35:740-751.
3. Chou TM, Sudhir K, Iwanaga S, Chatterjee K, Yock PG. Measurement of volumetric coronary blood flow by simultaneous intravascular two-dimensional and Doppler ultrasound: Validation in an animal mode. *Am Heart J* 1993; 2:237-243.
4. Dickinson RJ, Hill CR. Measurement of soft tissue motion using correlation between A-scans. *Ultrasound Med Biol* 1982;8:263-271.
5. Dotti D, Lombardi R. Estimation of the angle between ultrasound beam and blood velocity through correlation functions. *IEEE Trans. Ultrason. Ferroelec. Freq. Cont.* 1996;43:864-869.
6. Doucette JW, Corl D, Payne HM, Flynn AE, Goto M, Nassi M, Segal J. Doppler guide wire for intravascular measurement of coronary artery flow velocity. *Circulation* 1992;85:1899-18991.
7. Eichhorn EJ, Alvarez LG, Jessen Me, Fass Sm, Chao RY, Haagen D, Graburn PA. Measurement of coronary and peripheral artery flow by intravascular ultrasound and pulsed Doppler velocimetry. *Am J Cardiol* 1992;70:542-545.
8. Di Mario C, Gil R, Serruys PW. Long-term reproducibility of coronary flow velocity measurements in patients with coronary artery diseases. *Am J Cardiol* 1995;75:1177-1180.
9. Finet G, Maurincomme E, Tabib A, Crowley RJ, Magnin I, Roriz R, Beaune J, Amie M. Artifacts in intravascular ultrasound imaging: analyses and implications. *Ultrasound Med Biol* 1993;19:533-547.
10. Foster SG, Embree PM, O'Brien WD. Flow velocity profile via time-domain correlation: Error analysis and computer simulation. *IEEE Trans Ultrasonics* 1990;37:164-175.
11. Grayburn PA, Willard JE, Haagen Dr, Brickner ME, Alvarez LG, Eichhorn EJ. Measurement of coronary using high-frequency intravascular ultrasound imaging and pulsed Doppler velocimetry: in vitro feasibility studies. *J Am Soc Echocardiogr* 1992;5:5-12.
12. Gronningsaeter A, Angelsen BAJ, Heimdal A, Torp HG. Vessel wall detection and blood noise reduction in intravascular ultrasound imaging. *IEEE Trans Ultrasonics Freq Contr* 1996;43:359-369.

13. Gronningsaeter A, Angelsen BJ, Gresli, A, Torp, H. Blood noise reduction in intravascular ultrasound imaging. *IEEE Trans. Ultrason Ferroelec Freq Contr* 42:200-208; 1995.
14. Hein A, O'Brien D. Current time-domain methods for assessing tissue motion by analysis from reflected ultrasound echoes-A review. *IEEE Trans. Ultrason Ferroelec Freq Contr* 40:84-102; 1993.
15. Hoeks APG, Arts TGJ, Brands PJ, Reneman RS. Comparison of the performance of the RF cross correlation and Doppler autocorrelation technique to estimate the mean velocity of simulated ultrasound signals. *Ultrasound Med Biol* 1993;19:727-740.
16. Isner JM, Kaufman J, Rosenfield K, Pieczek A, Schainfeld R, Ramaswamy K, Kosowsky B. Combined physiologic and anatomic assessment of percutaneous revascularization using a Doppler guidewire and ultrasound catheter. *Am J Cardiol* 1993;71:70d-86d.
17. Johnson EL, Yock PG, Hargrave VK, Srebro JP, Manubens SM, Seitz W, Ports TA. Assesment of severity of coronary stenoses using a Doppler catheter: validation of a method based on the continuity equation. *Circulation* 1989;80:625-635.
18. Li W, Gussenhoven, EJ, Zhong Y, The SHK, Pieterman H, van Urk H, Bom N. Temporal averaging for quantification of lumen dimensions in intravascular ultrasound images. *Ultrasound Med Biol* 1994;20:117-122.
19. Li W, van der Steen AFW, Lancée CT, Honkoop J, Gussenhoven EJ, Bom N. Temporal correlation of blood scattering signals from intravascular ultrasound. in *Proc IEEE Ultrason Symp* 1995:1515-1518.
20. Li W, Van der Steen AFW, Lancée CT, Gussenhoven EJ, Bom N. Temporal correlation of blood scattering signals in vivo from radio frequency intravascular ultrasound. *Ultrasound Med Biol* 1996a;22:583-590.
21. Li W, Lancée CT, Céspedes EI, van der Steen AFW, Bom N. Decorrelation properties of an intravascular ultrasound beam. 1996b (submitted).
22. Pasterkamp G, van der Heiden MS, Post MJ, Ter Haar Romeny B, Mali WPTM, Borst, C. Discrimination of intravascular lumen and dissections in a single 30 MHz ultrasound image: use of 'confounding' blood backscatter to advantage. *Radiology* 1993;187:871-872.
23. Sudhir K, Macgregor JS, Barbant SD, Foster E, Fitzgerald PJ, Chatterjee K, Yock PG. Assessment of coronary conductance and resistance vessel reactivity in response to nitroglycerin, ergonovine and adenosine: In vivo studies with simultaneous intravascular tow-dimensional and Doppler ultrasound. *JACC* 1993;21:5:1261-1268.
24. Tadaoka S, Kagiya M, Hiramatsu O, Ogasawara Y, Tsujioka K, Wada Y, Sawayam T, Kajiya F. Accuracy of 20-MHz Doppler catheter coronary artery velocimetry for measurement of coronary blood flow velocity. *Cathet Cardiovasc Diagn* 1990;19:205-213.



25. Zhang X, Shikutani M, Yamamoto K. Measurement of displacement and flow vectors with a single ultrasound beam using a correlation technique (II) - Computer simulation and basic experiments. Techn Report IEICE 1995;35:23-30.



## CHAPTER 10

---

### SUMMARY



---

## SUMMARY

As quantitative intravascular ultrasound (IVUS) is becoming widely applied in routine clinics, there are increasing needs for improvement of the image quality, automated tools for image analysis or extension of the diagnostic capability of IVUS imaging techniques. The work presented in this thesis deals with these technical challenges by means of processing both the standard video image and the original radio frequency (RF) signals in intravascular ultrasound.

In *Chapter 1* the IVUS scanning mechanisms and some background information about ultrasonic imaging are introduced. The principles of three categories of the contour detection techniques in video image data are described, and the advantage of RF processing approaches is addressed, followed by some examples of applying RF analysis in IVUS data.

*Chapter 2* presents a validation study in which the accuracy and reproducibility of quantitative IVUS measurements were investigated. By comparing IVUS with other standard imaging techniques such as histology and angiography, it was demonstrated that the accuracy of IVUS measurements was high for the quantitation of vessel lumen and lesion areas. In both in vitro and in vivo studies, ultrasonic measurements agreed well with histology and angiography, except for a 17% underestimation in histologic lumen probably caused by the tissue fixation process. Variations in IVUS measurements induced by observer variability were 5%, 13% and 10% for the lumen, lesion and percent area obstruction, respectively. This degree of observer variability is within the acceptable range of routine clinical applications. It was concluded in this validation study that the quantitative measurement of vessel dimensions with IVUS imaging is accurate and reproducible.

The assessment of wall distensibility or compliance with IVUS imaging requires identification of the lumen boundary in each frame of an image sequence. *Chapter 3* describes a contour detection method that allows frame-to-frame tracking of the lumen boundary semi-automatically for analysis of the local wall displacement. This semi-automatic approach not only abates the need for extensive manual contour tracing of a considerable number of IVUS frames, but also improves the beat-to-beat reproducibility in the sequential measurement. A high measurement reproducibility is critical for analyzing a small change of the lumen dimension during a cardiac cycle.

The contour detection method was applied in the measurement of regional large artery compliance in pigs as well as in the assessment of wall distensibility in human diseased arteries. Results of both studies demonstrated the clinical utility of the proposed method for analyzing arterial wall compliance/distensibility with IVUS image data.

*Chapter 4* deals with three-dimensional (3D) image processing for volumetric

quantitation and 3D reconstruction of serial IVUS data. The pull-back data acquisition and image segmentation are the important steps to obtain accurate volumetric measurements and optimal 3D reconstruction of a vessel segment. Two types of spatial registration techniques, the displacement sensing device or continuous/stepper motors, can be used for 3D acquisition during a catheter pull-back procedure. The ECG-gated data acquisition is an efficient method to minimize the image artifact caused by the cardiac motion.

To reduce the time of analysis and the subjectivity of manual contour tracing, a semi-automatic approach for detection of the lumen and plaque contours on an IVUS slice sequence was developed. This method is based on the concept that edge points derived from longitudinal contours guide and facilitate the contour detection in the cross-sectional images. Furthermore, user interaction has been incorporated into the contour detection algorithm, which allows contour correction/redetection by a simple point-clicking manner. Comparison of computer-derived contours with manual tracings showed that this method enabled accurate detection of the lumen and plaque contours in a 3D intravascular ultrasound data set.

In *Chapter 5* the accuracy and reproducibility of the semi-automatic contour detection method were further evaluated in a phantom study as well as in intracoronary ultrasound data. The ultrasonic measurements of phantom lumen area and volume revealed an excellent agreement with the true phantom areas and volumes; mean differences in various segment diameters (2~5 mm) were less than 4% for the areas and 2% for the volumes. Intra- and interobserver comparison showed high correlations and small mean differences that were mostly in the order of a few percent. Thus, the proposed analysis system provided accurate measurements of phantom dimensions and can be used to perform highly reproducible area and volume measurements in 3D intravascular ultrasound in patients.

The high backscatter level of blood may reduce the intensity contrast at the lumen interface, causing difficulties in identification of the lumen boundary in IVUS images. *Chapter 6* and *7* tackle the problem of echogenic blood using two different approaches. In *Chapter 6* a video processing method is presented that enhances the lumen boundary by averaging a number of video frames from the diastolic period of a cardiac cycle. The utility of this method was tested by comparing the lumen area measurements on the temporal-averaged image with the data of the same cross-section obtained from the single-frame and saline-filled images. It was found that intraobserver variations in the averaging method were 2.4 times smaller than the measurements of the single-frame images and close to the data obtained by saline injection (variation coefficient: single-frame: 8.8%; temporal-averaged: 3.6%; saline-filled: 2.9%). It was concluded that the temporal-averaging method improved the accuracy and reproducibility in measurements

of the arterial lumen containing strong blood scattering echoes and can be used to replace the laborious saline injection method that facilitates off-line quantitative analysis.

The efficiency of the video averaging method, however, is limited by lack of phase information in the echo signals. Moreover, the relatively long time interval between video frames restricts real-time application of a video-based approach. To overcome the inherent limitation of video image processing, an RF signal processing method for lumen enhancement was developed. In *Chapter 7* the time-varying characteristics of blood scattering were investigated in vivo by means of analysis of an RF sequence acquired at a fixed angle. Results showed that the correlation time of blood echo signals was approximately 1 ms, while the signals from tissue remained at a high correlation value throughout the acquisition period of 6 ms. The difference in the correlation properties provided a basis to apply an RF processing method for suppression of the blood echo intensity. In this study two RF processing techniques, temporal averaging and correlation weighting, were tested. The latter method utilized the correlation output as a weighting function to modulate the amplitude of the received RF signals, and was shown to be highly effective in distinguishing scattering echoes of moving blood from those of static tissues. A significant enhancement at the luminal interface was obtained when applying the correlation processing to a cross-sectional image data. This RF-based approach can in principle be used for real-time image enhancement and automated contour detection of the luminal boundary.

Assessment of blood velocity and volume flow in a diseased vessel has been highly clinically desirable for the functional evaluation of a stenosis. The unique spatial relationship between the blood flow and the ultrasound beam provides a new potential to quantify volumetric flow with the IVUS imaging technique. The feasibility of extracting blood velocity from the decorrelation of an RF sequence was studied in *Chapter 8* and *9*.

In *Chapter 8* the decorrelation properties of an IVUS ultrasound beam were studied through theoretical analysis and computer simulation. A computer model based on the impulse response method was developed to describe the near-field of a 30 MHz intravascular ultrasound transducer. The computer simulations showed that the decorrelation function was approximately linearly dependent on the lateral displacement. Once the lateral decorrelation function at each axial beam position is measured, the relationship between correlation and displacement can potentially be used to estimate flow velocity. Decorrelation of echo signals, however, is a complex process that is not only related to the lateral displacement, but also associated with other decorrelation sources such as noise. These decorrelation sources may cause a bias in a decorrelation-based velocity measurement and should be isolated from the decorrelation of the lateral displacement. High variations in the correlation

measurement with a small range window present a major challenge for local velocity estimation. Therefore, a velocity estimation approach should be based on multiple decorrelation measurements in order to reduce the variations.

*Chapter 9* describes a decorrelation method for measuring local blood velocity and quantifying volume flow from cross-sectional RF data. In this approach, the decorrelation of echo signals is characterized by a decorrelation slope; the transverse velocity is estimated from the ratio between the *calibrated* displacement slope [ $\text{mm}^{-1}$ ] and the *measured* time slope [ $\text{s}^{-1}$ ]. The volumetric flow is calculated by integrating the local transverse velocity over the complete vessel cross-section.

The proposed velocity estimate method was tested in a series of in vitro measurements and in vivo in pig experiments. The in vitro study showed that the decorrelation method enabled localized velocity measurement over a complete vessel cross-section with sufficient spatial resolution for color flow mapping. Volumetric flow estimated from the cross-sectional velocity profiles correlated well with the readouts of an independent flowmeter. Similar flow-mapped images with reproducible cyclic changes were also observed in vivo using a commercial imaging system, demonstrating the feasibility of applying this method in clinical settings.

In conclusion, a number of image data and RF signal processing methods has been developed for the purposes of contour detection, image enhancement and blood velocity estimation in intravascular ultrasound. Because of the variations in the image quality of current IVUS systems, application of a fully automatic contour detection method remains a difficulty; a semi-automatic approach often appears to be more practical in handling the diverse image quality in clinical data. Processing of the original RF data has shown promise both in improvement of the IVUS image quality and in extraction of the blood flow velocity. One may therefore anticipate that the advance of RF processing techniques will eventually lead to the concept of functional imaging that provides simultaneous information on vessel morphology as well as on functional status of a diseased artery.



## SAMENVATTING

Daar kwantitatief intravasculair ultrageluid (IVUS) meer en meer routinematig in de kliniek wordt toegepast, ontstaat er ook meer behoefte aan verbetering van de beeldkwaliteit, een geautomatiseerde analysemethode of uitbreiding van de diagnostische capaciteiten van IVUS-afbeeldingstechnieken. Het in dit proefschrift gepresenteerde werk behandelt deze technische uitdaging met verwerking van zowel de standaard beeldgegevens als de oorspronkelijke radio frequente (RF) signalen in intravasculair ultrageluid.

In *Hoofdstuk 1* worden de IVUS scan-technieken besproken en wordt enige achtergrond-informatie gegeven over beeldvorming met behulp van ultrageluid. De principes van drie categorieën contourdetectie-technieken in videobeelden worden beschreven en het belang van RF-verwerkingstechnieken wordt aangegeven, gevolgd door enkele voorbeelden van de toepassing van RF-analyse in IVUS-data.

*Hoofdstuk 2* geeft een verslag van een evaluatiestudie, waarin de nauwkeurigheid en de reproduceerbaarheid van kwantitatieve IVUS-metingen werden onderzocht. Door IVUS met andere standaard afbeeldingstechnieken, zoals histologie en angiografie, te vergelijken, werd aangetoond dat de nauwkeurigheid van IVUS-metingen voor het kwantificeren van vaatlumen of de uitbreiding van een lesie hoog was. In zowel in vitro als in vivo studies kwamen de ultrageluidsmetingen goed overeen met histologie en angiografie, behalve 17% onderwaardering van het lumen in weefselpreparaten, veroorzaakt door krimp door het fixeren van het weefsel. Observer-geïnduceerde spreiding bedroeg voor IVUS-metingen van het lumen, de lesie en het percentage oppervlak obstructie respectievelijk 5%, 13% en 10%. Deze variabiliteit in de waarnemingen ligt binnen acceptabele grenzen voor klinische routine-toepassingen. De conclusie van deze evaluatiestudie was dat kwantitatief meten van vaatafmetingen met IVUS-afbeeldingstechnieken nauwkeurig en reproduceerbaar is.

Voor het vaststellen met IVUS-afbeeldingstechnieken van distensibiliteit of compliantie is het nodig de omtrek van het lumen te kennen in iedere doorsnede van een beeldsequentie.

*Hoofdstuk 3* beschrijft een contourdetectiemethode die het mogelijk maakt frame voor frame de omtrek van het lumen semi-automatisch te tekenen voor het analyseren van de wandverplaatsing ter plekke. Door deze semi-automatische aanpak bestaat er niet alleen minder noodzaak voor het arbeidsintensieve, handmatig trekken van contouren in een aanzienlijk aantal IVUS-doorsneden, maar wordt ook de reproduceerbaarheid van een cyclus in de achtereenvolgende metingen verbeterd. Een hoge reproduceerbaarheid van de metingen is van cruciaal belang om een kleine verandering van de lumenafmeting gedurende een hartcyclus te kunnen analyseren.

De contourdetectiemethode werd toegepast in de metingen van regionale compliantie van de grote arteriën in varkens en voor het vaststellen van de distensibiliteit van de wand in humane arteriën met een afwijking. De resultaten van beide studies toonden de bruikbaarheid van de voorgestelde methode aan voor het analyseren van distensibiliteit / compliantie van de arteriewand met IVUS-beeldgegevens.

*Hoofdstuk 4* gaat over drie-dimensionale (3D) beeldverwerking voor volumetrische kwantificering en 3D reconstructie van seriële IVUS-data. 'Pull-back' data-acquisitie en beeldsegmentatie zijn belangrijke stappen bij het verkrijgen van betrouwbare volumetrische meetgegevens en optimale 3D reconstructie van een vaatsegment. Twee soorten ruimtelijke registratietechnieken, gebruik van een verplaatsingsmeter of continu/stappenmotor, kunnen toegepast worden voor 3D acquisitie gedurende een catheter 'pull-back' procedure. Met het ECG gesynchroniseerde data acquisitie is een efficiënte methode om beeldfouten veroorzaakt door de beweging van het hart tot een minimum te beperken.

Om de analyseduur te verkorten en de subjectiviteit van het handmatig trekken van de contouren te vermijden, werd een semi-automatische aanpak voor contourdetectie van lumen en plaque in een sequentie van IVUS-doorsneden ontwikkeld. Bij deze methode zijn punten afgeleid van longitudinale contouren een leidraad voor contourdetectie in dwarsdoorsnede-beelden. Voorts is het contourdetectie algoritme berekend op interactie van de gebruiker, waardoor correctie of herdetectie van een contour door middel van het eenvoudig aanklikken van een punt mogelijk is. Vergelijking van met de computer verkregen contouren met handmatig getekende, liet zien dat met deze methode lumen- en plaquecontouren in een 3D intravasculaire ultrageluidsdataset nauwkeurig gedetecteerd kunnen worden.

In *Hoofdstuk 5* worden de nauwkeurigheid en de reproduceerbaarheid van de semi-automatische contourdetectiemethode verder getoetst zowel in een fantoomstudie als bij toepassing op intracoronaire ultrageluidsdata. De ultrageluidsmetingen van lumenoppervlak en -volume van het fantoom kwamen goed overeen met de ware oppervlakken en volumes in het fantoom; de gemiddelde verschillen bij verschillende doorsneden (2-5 mm) van het segment waren minder dan 4% voor de oppervlaktes en 2% voor de volumes. Intra- en interobservervarianties waren meestal in de orde van enkele procenten. Het voorgestelde analysesysteem leverde dus nauwkeurige resultaten bij de metingen aan fantomen en kan worden gebruikt voor reproduceerbare metingen met 3D intravasculair ultrageluid in patiënten.

Het hoge backscatterniveau van bloed vermindert het contrast bij de overgang van het lumen naar de vaatwand en bemoeilijkt zo het vaststellen van de omtrek van het lumen in IVUS-beelden. In de *hoofdstukken 6 en 7* wordt het probleem van echogeen bloed op twee manieren aangepakt. In *Hoofdstuk 6* wordt een video verwerkingsmethode

gepresenteerd, die de omtrek van het lumen beter zichtbaar maakt door het middelen van een aantal videobeelden uit de diastolische fase van de hartcyclus. De bruikbaarheid van deze methode werd getest door de metingen van lumen oppervlakte op het tijd-gemiddelde beeld te vergelijken met de gegevens van dezelfde dwarsdoorsnede verkregen uit een enkele doorsnede en bij vulling met een fysiologische zoutoplossing. Het bleek dat de variaties bij dezelfde waarnemer bij de middelingsmethode 2.4 keer kleiner waren dan bij de enkele doorsnedebeelden en dicht bij de gegevens verkregen bij inspuiting met de zoutoplossing (variantie co-efficiënt: enkel beeld: 8.8%; tijd-gemiddeld: 3.6%; zoutoplossing: 2.9%). Er werd geconcludeerd dat de tijdmiddeling methode een verbetering te zien gaf van de nauwkeurigheid en de reproduceerbaarheid bij metingen van het lumen in arteriën waarin sterke bloedscattering optrad en dat deze methode een vervanging kan zijn voor de bewerkelijke injectie van fysiologisch zout die off-line kwantitatieve analyse vergemakkelijkt.

De efficiency van de video middelingsmethode wordt echter beperkt door gebrek aan fase-informatie in de echosignalen. Voorts beperkt het relatief grote tijdsinterval tussen de videobeelden real-time toepassing van een op video gebaseerde methode. Teneinde de aan verwerking van videobeelden inherente beperkingen te ondervangen, werd er een op de verwerking van het RF-sigitaal gebaseerde methode ontwikkeld voor verbetering van de afbeelding van het lumen.

In *Hoofdstuk 7* werden de tijdsafhankelijke eigenschappen van bloed scattering in vivo onderzocht door middel van analyse van een RF-sequentie verkregen onder een vaste hoek. De resultaten lieten zien dat de correlatietijd van van bloed afkomstige echosignalen ongeveer

1 ms was, terwijl de van weefsel afkomstige signalen gedurende de gehele acquisitietijd een hoge correlatiewaarde van 6 ms behielden. Het verschil in de correlatie-eigenschappen verschafte een basis voor het toepassen van een RF-verwerkingsmethode voor onderdrukking van de de echo-intensiteit van bloed. In deze studie werden twee RF-verwerkingsmethoden getest: tijdmiddeling en correlatieweging. De laatste gebruikte de correlatie-uitkomsten als een weegfunctie om de amplitude van de ontvangen RF-signalen te moduleren en bleek zeer effectief bij het maken van een onderscheid tussen verstrooiing van bewegend bloed en die van statisch weefsel. Een belangrijke verbetering bij de overgang van lumen naar weefsel werd bereikt toen de correlatiemethode toegepast werd op de gegevens van een doorsnedebeeld. Deze op het RF signaal gebaseerde methode kan in principe gebruikt worden voor real time beeldverbetering en automatische contourdetectie van het lumen.

Bepaling van bloedsnelheid en stroomvolume in een aangetast vat is klinisch gezien wenselijk voor het beoordelen van de functionaliteit bij een stenose. De unieke ruimtelijke relatie tussen stromend bloed en ultrageluidsbundel verschaft een nieuw middel om het stroomvolume te kwantificeren met behulp van de IVUS-afbeeldingstechniek. De haalbaarheid van het bepalen van de bloedsnelheid uit de decorrelatie van een RF-sequentie wordt bestudeerd in *Hoofdstuk 8* en *Hoofdstuk 9*.

In *Hoofdstuk 8* worden de decorrelatie-eigenschappen van een IVUS-bundel bestudeerd, gebruik makend van theoretische analyse en computer-simulatie. Op basis van de impuls respons methode werd een computermodel ontwikkeld om het nabijeveld van een 30 MHz intravasculaire ultrageluidstransducent te beschrijven. De computersimulaties toonden aan dat de decorrelatiefunctie bij benadering lineair afhankelijk is van de laterale verplaatsing. Als eenmaal de laterale decorrelatiefunctie op iedere positie van de as van de bundel is gemeten, kan de relatie tussen correlatie en verplaatsing mogelijk gebruikt worden om de bloedsnelheid te berekenen. Decorrelatie van echosignalen is echter een complex proces dat niet alleen aan de laterale verplaatsing is gerelateerd, maar ook geassocieerd is met andere decorrelatiebronnen zoals ruis. Deze decorrelatiebronnen kunnen een bias veroorzaken in een op decorrelatie gebaseerde snelheidsmeting en moeten worden geïsoleerd uit de correlatie van de laterale verplaatsing. Grote variaties in correlatiemetingen met een klein window zijn de belangrijkste factoren die de betrouwbaarheid van lokale snelheidsberekening nadelig beïnvloeden. Daarom moet berekening van de snelheid gebaseerd zijn op multi-pele decorrelatiemetingen, zodat deze variaties verkleind worden.

*Hoofdstuk 9* beschrijft een decorrelatiemethode om plaatselijke bloedsnelheid te meten en het stroomvolume te kwantificeren uit RF-data van dwarsdoorsneden. Bij deze benadering is de decorrelatie van echosignalen gekenmerkt door de richtingscoëfficiënt tegen de tijd of de verplaatsing; de transversale snelheid wordt berekend uit de verhouding tussen de gecalibreerde richtingscoëfficiënt van de correlatie tegen de verplaatsing [ $\text{mm}^{-1}$ ] en de gemeten richtingscoëfficiënt van de correlatie tegen de tijd [ $\text{s}^{-1}$ ]. De volumetrische doorstroom wordt berekend door de plaatselijke transversale snelheid te integreren over de gehele dwarsdoorsnede van het vat.

De voorgestelde snelheidsberekeningsmethode werd getest in een aantal in vitro metingen en in vivo experimenten in varkens. De in vitro proeven toonden aan, dat de decorrelatiemethode plaatselijke snelheidsmeting mogelijk maakt in een volledige dwarsdoorsnede van een vat, met voldoende spatiale resolutie voor "color flow mapping". Volumetrische doorstroom berekeningen op grond van snelheidsprofielen in een doorsnede kwamen goed overeen met de aflezingen op een onafhankelijke flowmeter. Dergelijke flow-mapped beelden met reproduceerbare cyclische

veranderingen werden ook in vivo waargenomen bij gebruik van een in de handel zijnde IVUS-apparaat, waardoor de haalbaarheid van toepassing in de kliniek is aangetoond.

Concluderend: een aantal methoden voor verwerking van beeldgegevens en RF-sigitaal werd ontwikkeld met als doel contourdetectie, beeldverbetering en bloedsnelheidsberekening in intravasculair ultrageluid. Door verschillen in beeldkwaliteit van de huidige IVUS-systemen blijft toepassing van volledig geautomatiseerde contourdetectie een moeilijke zaak; een semi-automatische aanpak blijkt dikwijls van meer praktische waarde bij het omgaan met verschillen in kwaliteit van klinische beelden.

Verwerking van de originele RF-gegevens is veelbelovend, zowel voor verbetering van de IVUS beeldkwaliteit als voor het afleiden van bloedstroomsnelheid. Daarom mag verwacht worden dat het voordeel van RF-verwerkingstechnieken zal leiden tot het idee van functioneel afbeelden, waarbij tegelijkertijd informatie over zowel vaatmorfologie als functionaliteit van een aangedane arterie beschikbaar is.



## APPENDIX I: MINIMUM COST ALGORITHM

The minimum-cost algorithm (MCA) is a global optimization technique based on dynamic programming. This method was introduced by Montanari and Martelli in their work of applying the dynamic programming approach to solve edge detection problems [1,2]. In general, the MCA-based contour detection procedure contains the following steps [3]: 1) image transformation; 2) cost calculation; 3) minimum-cost path detection. By transforming the original IVUS image into the polar coordinates, finding a closed two-dimensional contour such as the arterial lumen is simplified to determining an one-dimensional path on the transformed matrix.

### MCA optimization

Denote the transformed image matrix  $I(i,j)$  with  $i=1...M$  rows and  $j=1...N$  columns. A cost value  $C(i,j)$  is assigned to each element  $I(i,j)$ , which forms a cost matrix of the same size with a low value presenting a high possibility of the associated pixel being a contour point. Let a sequence of points  $p(i)$ ,  $i=1...M$  define a path  $P=\{p(1)...p(M)\}$  that travels from the top to the bottom of the cost matrix. To add the connectivity constrain of a contour, an allowable path meets:  $|p(i) - p(i-1)| \leq 1$ , which means each  $p(i)$  may have only three possible predecessors and three successors as illustrated in Fig. 1.

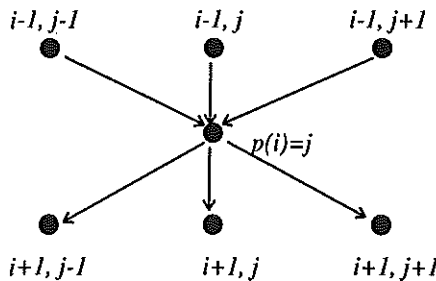


Fig. 1. Illustration of the three predecessors and successors of point  $p(i)$ .

The merit of a path being the required contour is evaluated by a simple accumulative cost function:

$$\zeta = \sum_{i=1}^M C(i, p(i)) \quad (A1)$$

The contour detection problem is now formulated as determination of an optimal path  $P_m$  that minimizes the merit function for all the admissible paths  $\chi$ :

$$P_n = \arg(\min\{\zeta\}) \quad (A2)$$

$$m \in k; P_k \in \chi$$

The MCA optimization procedure consists of two steps:

1. Determine the minimum value of the merit function  $\zeta^m$  for all  $P_i \in \chi$ .
2. Trace back the sequence  $P_m = \{p_m(1) \dots p_m(M)\}$  from which the minimum  $\zeta^m$  is obtained.

### *MCA implementation*

The first optimization step is realized by means of the following recursion:

$$\zeta_0(j) = 0$$

$$\zeta_i(j) = \min\{C(i, j) + \zeta_{i-1}(k)\} \quad i=1 \dots M; \quad j=1 \dots N \quad (A3)$$

$$k = \{j-1, j+1\}$$

The  $k$  value at which the minimum cost value is found is stored in an index matrix  $m(i, j)$ :

$$m(i, j) = \arg(\min\{C(i, j) + \zeta_{i-1}(k)\}) \quad (A4)$$

$$k = \{j-1, j+1\}$$

At the end of recursion, a sequence of merit values  $\zeta_{i=M}(j)$ ,  $j=1 \dots N$  is obtained. The minimum accumulative cost value is then determined:

$$\zeta^m = \min\{\zeta_{i=M}(j)\}$$

$$j = \{1 \dots N\}$$

The second step is to find the optimal path by tracing the index matrix  $m(i, j)$  backwards:

$$p_m(M) = \arg(\zeta^m) \quad i=M-1, \dots, 1 \quad (A5)$$

$$p_n(i) = m(i, p_m(i+1))$$

### *Cost calculation*

The definition of the cost matrix is crucial for the success of the MCA contour detection approach. A low cost value should be assigned to the point with a high possibility of being contour.

**Cost value for detection of the lumen:** The lumen boundary is characterized by the gray transaction from low to high intensity. The cost value for the lumen detection is derived from the first derivative of the gray intensity:



$$\begin{cases} C^L(i, j) = \begin{cases} (I(i, j-1) - I(i, j+1))F(I_l) \\ 0 & I(i, j-1) > I(i, j+1) \end{cases} \\ F(I_l) \propto 1/I_l \\ I_l = (I(i, j-1) + I(i, j))/2 \end{cases} \quad (A6)$$

The linear function  $F(I_l)$  modifies the derivative value according to the lumen intensity estimated by  $I_l$ . Since the lumen intensity is expected to be low, this function reduces the cost value when  $I_l$  is high.

**Cost value for detection of the total vessel wall:** The interface of the total vessel wall is identified by the echo-lucent media which is followed by the echogenic adventitia. The media interface is recognized by a black-ring structure on the IVUS image. After image transformation, the ring structure will be converted into a line pattern. To detect this feature, a pattern matching approach is applied for the cost calculation. A block of image data with size  $L$  rows by  $K$  columns is cross-correlated with three predefined templates  $L_p(l, k)$ :

$$\begin{cases} C_p^M(i, j) = \frac{1}{N_p} \frac{\sum_{l=0}^L \sum_{k=0}^K L_p(l, k)(I(i+l, j+k) - \bar{I})}{\sqrt{\sum_{l=0}^L \sum_{k=0}^K (I(i+l, j+k) - \bar{I})^2}} \\ C^M(i, j) = -\max\{C_p^M(i, j)\} \quad p=1,2,3; l=1\dots L; k=1\dots K \end{cases} \quad (A7)$$

where  $\bar{I}$  is the mean value of the data block,  $N_p$  is the normalized factor for each template and the means of the templates are set to zero. The three templates  $\{L_1 L_2 L_3\}$  are corresponding to three line patterns with angles of  $-\pi/4$ ,  $0$ , and  $\pi/4$  with respect to the tangent of the resample circle. The best match of the three line patterns  $C^M(i, j)$  is selected as the cost value.

## REFERENCES

1. Montanari. On the optimal detection of curves in noisy pictures. Communications of the ACM 1971(14): 335-345.
2. Martelli. Edge detection using heuristic search methods. Computer graphics and image processing 1972(1): 169-182.

3. Gerbrands JJ. Segmentation of noisy images. Ph.D. Thesis, Delft University of Technology, 21 June 1988.

## APPENDIX II: IMPULSE RESPONSE MODEL

This chapter describes the computer model that simulates the responses of a circular transducer when scatterers move cross the soundfield.

### General theory

The geometry of the computer model used in the simulation is illustrated in Fig. 1. Let  $u$  be the response of the element surface  $S$  in the soundfield of a point scatterer located at the end of pointing vector  $R$ .

If the soundfield contains only a single frequency component with wave number  $k$ , then the pressure response can be expressed as:

$$u(k) = C \iint_S 1/R \times \exp(-jkR) dS, \quad (A1)$$

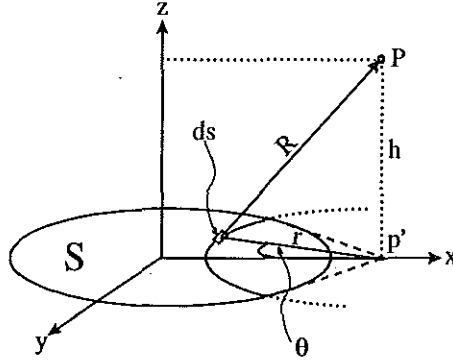


Fig. 1. Geometry of the ultrasound model.

where the wave number  $k=2\pi/\lambda$ , and  $C$  is a conversion constant. The relation between  $R$  and  $r$  is  $r^2 + h^2 = R^2$ . Differentiation of left- and right hand terms yields  $r.dr = R.dR$ . The elementary surface  $dS = r.dr.d\theta$  can now be expressed as a function of  $R$  :  $dS = R.dR.d\theta$ .

Equation A1 can be simplified to:

$$u(k) = C \int_{R_{min}}^{R_{max}} \int_{\theta_{min}}^{\theta_{max}} \exp(-jkR) dR.d\theta \quad (A2)$$

In order to use A2 in a discrete computer model the equation can be approximated by:

$$u(k) = CdR \sum_{i=1}^N (\exp(-jkR_i) \int_{\theta_{min}(i)}^{\theta_{max}(i)} d\theta), \quad (A3)$$

where  $N$  is the discrete number of increments  $dR$  that is used to sample the range of  $R$ . The equation A3 can be simplified into:

$$u(k) = CdR \sum_{i=1}^N [\theta_{max}(i) - \theta_{min}(i)] \exp(-jkR_i) \quad (A4)$$

Use of equation A4 for the computation of the response involves the following steps:

- define a number  $N$  for the range of  $R$ .
- determine the minimum and maximum value of  $R$ , and using  $N$ , the value of  $dR$ .
- at each value of  $R_i$  evaluate the phase term  $\exp(-jkR_i)$ .

- at each value of  $R_i$  evaluate the angles  $\Theta$ , where the wavefront intersects the element boundary.

Because of the reciprocity of the propagation of sound, the equation A4 also expresses the pressure at the location of the scatterer when the transducer is acting as the sound source. The roundtrip response  $U$  of the element acting as transmitter and receiver with a single scatterer in the sound field can be expressed in the frequency domain as:

$$U(k) = u(k) \cdot u(k) \tag{A5}$$

When instead of a single frequency a spectrum of frequencies is transmitted, the broadband response of the transducer is obtained by weighting the individual  $u(k)$  components with the amplitude and phase terms of the spectrum.

### *Implementation of the model*

A Pentium 200MHz personal computer system has been chosen as the platform for the model.

The calculations were performed using MATLAB (The MathWorks, Inc, MA, USA). The model was defined in a matrix representation, since the MATLAB performance is optimized for matrix operations.

A fixed value of  $N$  was set to 100 in order to obtain a reasonable accuracy and still a moderate size of the matrices to be calculated. The accuracy of the model will be discussed in a later section of this chapter.

The worst case value of  $dR$  at  $N = 100$  is .01 mm, which is still much lower than the .05 mm wavelength at the center frequency of 30 MHz.

### *The frequency spectrum*

For the simulation of the transducer response a Gaussian shaped time pulse was defined as:

$$puls(t) = \exp[-(t - t_0)^2 / 2\sigma^2] \cdot \sin(2\pi f_0 t), \text{ where}$$

$t_0$  is an offset to prevent the pulse from aliasing in the time window,  
 $\sigma = 4dt$  with  $dt = 1/fs$  controls the bandwidth of the pulse and,  
 $f_0 = 30 \text{ MHz}$  is the center frequency of the transducer.

This time series was sampled with  $fs = 200 \text{ MHz}$  and the frequency domain representation of the pulse was obtained by a 256 point FFT, from which only the positive frequencies of the spectrum were used. A further reduction of the data was obtained by selecting only those components with a magnitude of more than -20dB relative to the maximum component. This resulted in a spectrum of 44 non-zero complex frequency components described by 2 row vectors:

$F_{pulse}(1:44)$  and  
 $k(1:44) = 2\pi/c.f(1:44)$ , where  $c$  is the sound velocity.

### Model calculations

The scatterers are sorted in range windows, since the frequency response is defined in only 256 points, which corresponds with a range of only  $256*dt$  or  $1.28 \mu s$ . For each window the spectrum is phase corrected in order to let its timepulse start at the beginning of the window. For each scatterer inside the window the model returns a value for  $dR$ , a column vector  $R(1:100)$  and a column vector  $Theta(1:100)$ .

The one-way response  $u$  can now be expressed in matrix notation:

$$[u] = C dR [Theta \times F_{pulse}] .* \exp(-j [R \times k]),$$

where  $\times$  indicates a matrix multiplication and  $.*$  indicates an array multiplication;  $[u]$  is a 100 by 44 matrix.

Calculating  $u = \text{sum}([u])$ , where  $\text{sum}$  is a column wise summation, the matrix is reduced to a 44 element row vector containing the one-way frequency response of the input scatterer. The roundtrip response  $U_s$  is simply obtained by  $U_s = u .* u$  and is also a 44 element row vector.

The combined response of all the scatterers in one range window is obtained by adding their individual responses:

$$U_{total} = \sum_s U_s.$$

When all the scatterers in a range window have been calculated, the inverse FFT can be taken to produce the time trace of that particular window. Subsequent handling of all range windows will finally produce a single time trace of the total assembly of scatterers. The time signal can be used as an input for the correlation programs.

### Accuracy of the model

Since the calculation time of the model depends linearly on the number of increments  $N$ , the initial value of  $N$  was kept low ( $N=100$ ). In order to test the accuracy thus obtained, the model output was compared with the results of a much higher setting of  $N=1000$ . With  $N=1000$  the worst case value for the range increment drops from 10 to 1 micrometer, yielding an almost perfect estimation of the transducer area at a 10 times lower computation rate.

The complex response  $U(j)$  of a single scatterer was mapped over an area of 1 mm lateral by 10 mm axial. The step size in the lateral dimension was .01 mm, while the axial dimension was sampled at .1 mm intervals. In order to obtain meaningful phase information, a single frequency of 30 MHz was used. For the two models  $U_{1000}(j)$  and  $U_{100}(j)$  are obtained.

*Amplitude and phase response*

Let  $A_{100}(j) = \text{Abs}( U_{100}(j) )$  represent the amplitude distribution in the field at  $N = 100$ , and

let  $A_{1000}(j) = \text{Abs}( U_{1000}(j) )$  represent the amplitude distribution in the field at  $N = 1000$ .

Let  $\text{Phase}_{100}(j) = \text{Angle}( U_{100}(j) )$  represent the phase angle distribution in the field at  $N = 100$ , and

let  $\text{Phase}_{1000}(j) = \text{Angle}( U_{1000}(j) )$  represent the phase angle distribution in the field at  $N = 1000$ .

In Fig. 2 plots of  $A_{1000}(j)$  in the upper panel and  $\text{Phase}_{1000}(j)$  in the lower panel show the large model output.

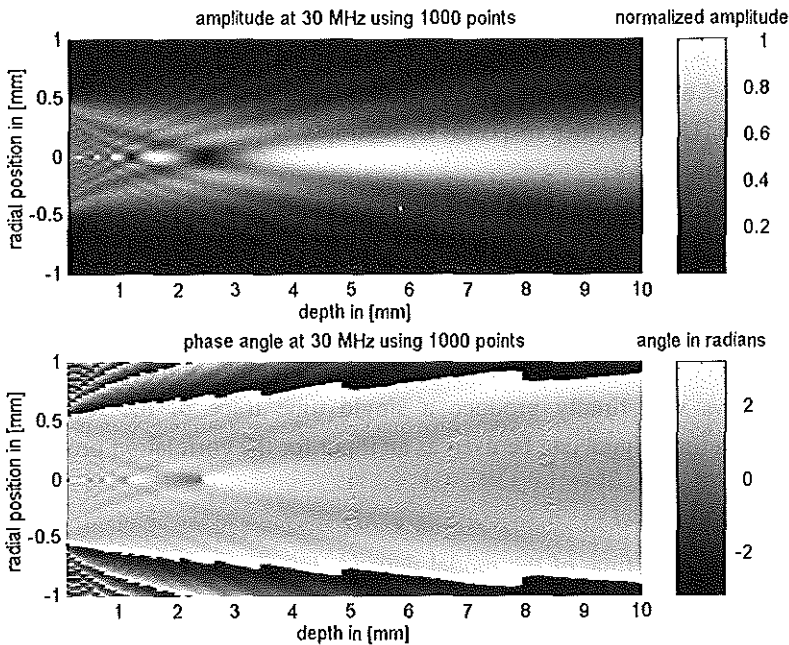


*Fig. 2. Upper panel: The magnitude of the large model is plotted as a function of scatterer position. The magnitude is normalized on the maximum value. Lower panel: The phase angle of the large model is plotted in radians as a function of scatterer position.*

*Amplitude and phase accuracy*

The amplitude errors introduced by the smaller model can be defined as the normalized amplitude difference:

$$\frac{A_{100}(j) - A_{1000}(j)}{\max(A_{1000}(j))} \cdot 100 \%.$$

As plotted in the upper panel of Fig. 3., data in this figure show that the model accuracy at  $N=100$  is good in most of the field. The area's where the errors increase are also the area's where the field is very weak, close to the edge and outside the transducer surface.

The errors in the phase angle introduced by the smaller model can be simply defined to be the absolute difference between the two models:

$$\text{Abs}( \text{Phase}_{1000}(j) - \text{Phase}_{100}(j) ).$$

As plotted in the lower panel of Fig. 3., data in this figure reveal a small perturbation in the phase at the transducer edge, generated by the small model, which persists over a considerable depth. In most of the field the phase approximation seems however

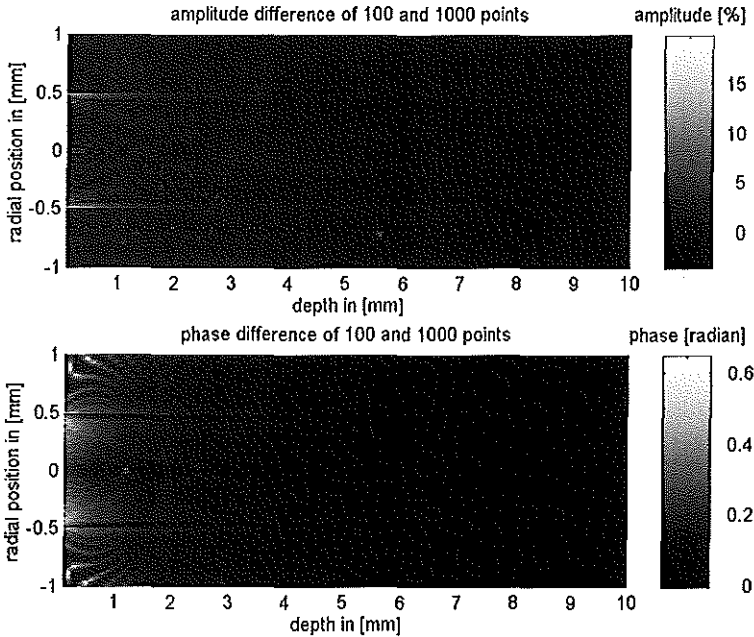


*Fig. 3. Upper panel: The amplitude error of the small model is plotted as a function of scatterer position. It's magnitude is defined as the difference between the two models normalized on the maximum value of the large model and expressed in percentage.*

*Lower panel: The error in the phase angle of the small model is plotted as a function of scatterer position. It's magnitude is defined as the absolute difference between the two models and expressed in radians.*

reasonably good. The phase approximation seems to be less accurate in the position extremely close to the transducer surface, but the error remains smaller than  $\pi/4$ .

*Computation time*

The performance of this method was tested in a series of 10,000 randomly distributed scatterers in the volume of  $X=2$  mm,  $Y=2$  mm and  $Z=9$  mm. The time to calculate the complex response in frequency domain was  $403.9 \pm 4.6$  s and the time to transform the frequency data into a time trace was 0.22 s. The average time for calculation of the response of one scatterer is in the order of 40 ms.



## ACKNOWLEDGEMENTS

In 1989, with a little knowledge about Holland, I was given an opportunity to join in the laboratory of Experimental Echocardiography as a visiting scholar. My very first impression came from a brand-new computer which had been arranged for me long before my arrival. I soon realized that this was a perfect opportunity to pursue my Ph.D. degree. Since then, I have been gaining support and friendship from all my colleagues in the lab. Without their assistance and generous contribution, it would not have been possible for me to complete this thesis.

Prof. N. Bom, my supervisor and promotor, supported me not only by guiding my research activities but also by helping me to settle in a new environment. Thanks to his guidance and encouragement, I was able to gradually build up the foundation of this thesis and thanks to his constant "push", I managed to finish the writing on time. Furthermore, I acknowledge his generosity for offering me a position to carry out my Ph.D. research and my wife a chance to come to work at our lab.

The enthusiasm of Prof. J.R.T.C. Roelandt has always been a great encouragement that makes me realize the clinical value of my work. Being the director of the Thoraxcentre, his open attitude towards new technologies is essential to the success of my Ph.D. research project, just as to that of many others. Therefore I am grateful for having him as one of my promotores.

I would like to express my gratitude to Dr. A.F.W. van der Steen, my supervisor and co-promotor, for his enormous effort in organizing my research work, planning my publications and reviewing manuscripts. During the preparation of this thesis, I benefited from both his inspiring suggestions and his management skill, from which I have learnt a great deal about what will be needed for a successful career in academics.

Dr. C.T. Lancée has contributed substantially to my thesis in developing a computer simulation framework and I am indebted to him for his critical reading and correction of other chapters.

The completion of my Ph.D. research reflects the importance of a close cooperation between engineers and clinicians, which has been the key for the success of many other projects at the Thoraxcentre. At the early stage of the project, I was very much pre-occupied by all sorts of technical problems without knowing the practical situation in clinics. Dr. E.J. Gussenhoven, with her years of experience in clinical research, dragged me out of my pure technical thinking and helped me to find a practical way of meeting clinical requirements. Also, I would like to thank her for her comments and corrections of some of the chapters.

I am grateful to Dr. C. von Birgelen for his significant contribution in quantitative three-dimensional intravascular ultrasound. His stimulating discussions and suggestions have been a very helpful feedback for the improvement of the computer analysis program.

I would like to thank Prof. J.H.C. Reiber and his group at the Leiden University Hospital for providing me an excellent start and for the fruitful collaboration in the automatic contour detection project. In particular, Ir. J.G. Bosch has given me a lot of useful suggestions during our discussions.

I acknowledge Prof. P.D. Verdouw and his group for their support in carrying out animal experiments, and Prof. P.W. Serruys, Prof. H. van Urk, Dr. P.J. de Feyter for providing me invaluable clinical feedback with their expertise.

I sincerely thank Ms. C. Eefting, our secretary, for her assistance in preparing so many documents for different types of application forms, letters and permits. The huge pile of files labeled 'Li's documents' in her drawer indicates only a very small part of what she has done for me during the past few years. Furthermore, I wish to thank Ms. T. Matla for her assistance in typing Chapters 2&3.

Throughout my Ph.D. training period, I have been helped by my colleagues in so many aspects that I could not possibly list all of them. I would like to thank F. Mastik for his support in software programming, F. van Egmond and J. Honkoop for their technical support in designing and building very special hardware. I am indebted to Dr. E.I. Céspedes for his suggestions and corrections of Chapters 8&9. I would like to acknowledge many others who have provided me help and support: Dr. H. ten Hoff, Dr. S.H.K. The, Dr. C. Di Mario, Dr. A. van der Lugt, Dr. N. de Jong, Dr. H. Pieterman, Dr. R.A. Wilson, Dr. B.M. ter Haar Romeny, Ir. C.J. Bouma, Drs. A. Hartlooper, Ir. C.L. de Korte, Ir. P.J.A. Frinking, Dr. S. Carlier, Ir. K.K. Djoa, Dr. N. van der Putten, Ing. N. Bruining, Ir. C.J. Slager, Dr. R. Krams.

Finally, I especially thank my wife, Y. Zhong, for her full support and understanding and my parents in China for their encouragement.

---

**PUBLICATIONS**

1. Li W, Gussenhoven WJ, Bosch JG, Mastik F, Reiber JHC, Bom N. A computer-aided analysis system for the quantitative assessment of intravascular ultrasound images. In: *Computers in Cardiology 1990*, Los Alamitos: IEEE Computer Society Press 1990: 333-336.
2. Li W, Gussenhoven WJ, Zhong Y, The SHK, Di Mario C, Madretsma S, van Egmond FC, de Feyter PJ, Pieterman H, van Urk H, Rijsterborgh H, Bom N. Validation of quantitative analysis of intravascular ultrasound images. *Int J Cardiac Imag* 1991 (6): 247-253.
3. Gussenhoven WJ, The SHK, Serruys PW, van Urk H, Pieterman H, van Egmond FC, Roelandt J, Lancée CT, Li W, Zhong Y. Intravascular ultrasound and vascular intervention. *J Interventional Cardiol* 1991 (4): 41-48.
4. Gussenhoven WJ, The SHK, Gerritsen P, van Urk H, Li W, van Egmond FC, Roelandt JRTC, Lancée CT, Bom N. Real-time intravascular ultrasonic imaging before and after balloon angioplasty. *J Clin Ultrasound* 1991 (19): 294 - 297.
5. Gussenhoven WJ, Bom N, Li W, van Urk H, Pieterman H, van Suylen RJ, The SHK: The hypoechoic media: a landmark for intravascular ultrasonic imaging. In: *SPIE Vol 1425 Diagnostic and therapeutic interventions 1991*: 203-206.
6. Gussenhoven WJ, Madretsma S, Pieterman H, The SHK, Li W, van Egmond FC, Bom N. Detection of vascular morphology by high frequency intravascular ultrasonic imaging. *Lasers Med Sci* 1991 (6): 349-354.
7. Li W, Bosch JG, Zhong Y, Gussenhoven WJ, Rijsterborgh H, Reiber JHC, Bom N. Semiautomatic frame-to-frame tracking of the luminal border from intravascular ultrasound. In: *Computers in Cardiology 1992*, Los Alamitos: IEEE Computer Society Press, 1992: 353-356.
8. Bom N, Lancée CT, Gussenhoven WJ, Li W, Ten Hoff H: Basic principles of intravascular ultrasound imaging. In: *Intravascular Ultrasound Imaging* (J.M. Tobis and P. Yock, eds) Churchill Livingstone Medical Publishers, New York 1992: 7-15.

9. Bom N, Lancée CT, Gussenhoven WJ, Roelandt J, Li W, de Kroon MGM. Intravascular scanning devices and their clinical value. In: Innovations in Abdominal Ultrasound, Heyder N, Hahn EG, Goldberg BB eds. Berlin, Springer Verlag 1992: 81-86.
10. Di Mario C, The SHK, Madretsma S, van Suylen RJ, Wilson RA, Bom N, Serruys PW, Gussenhoven WJ, Roelandt JRTC, Zhong Y, Li W: Detection and Characterization of Vascular Lesions by Intravascular Ultrasound: An In Vitro Study Correlated with Histology. *J Am Soc Echocardiogr* 1992 (5): 135-146.
11. The SHK, Gussenhoven WJ, Zhong Y, Li W, van Egmond FC, Pieterman H, van Urk H, Gerritsen P, Borst C, Wilson R, Bom N. Effect of balloon angioplasty on femoral artery evaluated with intravascular ultrasound imaging. *Circulation* 1992 (86): 483-493.
12. The SHK, Gussenhoven EJ, W Li, de Feyter P, Serruys PW, Wilson RA, Bom N: Intravascular ultrasonic assessment of lumen geometry and distensibility of the angiographically normal artery: a correlation with quantitative angiography. *Echocardiography* 1992 (9): 133-139.
13. Li W, Bosch JG, Zhong Y, The SHK, Gussenhoven EJ, Mastik F, van Egmond FC, Rijsterborgh H, Reiber JHC, Bom N. Image segmentation and 3D reconstruction of intravascular ultrasound images. In: *Acoustical Imaging Vol. 20* (Y. Wei & B. Gu, eds.). Plenum Press, New York 1993: 489-496.
14. Li W, Bouma CJ, Gussenhoven EJ, Ter Haar Romeny BM, Pasterkamp G, Rijsterborgh H, Pieterman H. Computer-aided intravascular ultrasound diagnostics. In: *Intravascular Ultrasound* (J. Roelandt, E.J. Gussenhoven, N. Bom, eds.) Kluwer Academic Publishers, Dordrecht 1993: 79-90.
15. Di Mario C, Li W, Linker DT, de Feyter PJ, Bom N, Serruys PW, Roelandt JRTC. Three-dimensional intracoronary ultrasound. Goals and practical problems. In: *Intravascular Ultrasound 1993* (J. Roelandt, E.J. Gussenhoven, N. Bom, eds.) Kluwer Academic Publishers, Dordrecht 1993: 63-77.
16. Gerritsen GP, Gussenhoven EJ, The SHK, Pieterman H, Zhong Y, Li W, Bom N, van Dijk LC, Du Bois NAJJ, van Urk H. Intravascular ultrasound before and after intervention: in vivo comparison with angiography. *J Vasc Surg* 1993 (18):31-40.

- 
17. Gussenhoven EJ, van der Lugt A, van Strijen M, Li W, Kroeze H, The SHK, van Egmond FC, Peters RJG, de Feyter PJ, van Urk H, Pieterman H. Displacement sensing device enabling accurate documentation of catheter tip position. In: *Intravascular Ultrasound 1993* (J. Roelandt, E.J. Gussenhoven, N. Bom, eds.) Kluwer Academic Publishers, Dordrecht 1993: 157-166.
  18. Lancée CT, Li W: Intravascular ultrasound: principles and instrumentation. In: *Cardiac Ultrasound* (Roelandt JRTC, Sutherland GR, Iliceto S, Linker D, eds.) Churchill Livingstone, Edinburgh 1993: 833-838.
  19. Li W, Gussenhoven EJ, Zhong Y, The SHK, Pieterman H, van Urk H, Bom N. Temporal averaging for quantification of lumen dimensions in intravascular ultrasound images. *Ultrasound Med Biol* 1994 (20): 117-122.
  20. Li W, von Birgelen C, Di Mario C, Boersma E, Gussenhoven EJ, van der Putten N, Bom N. Semi-automatic contour detection for volumetric quantification of intracoronary ultrasound. In: *Computers in Cardiology 1994*, Los Alamitos: IEEE Computer Society Press 1994:277-280.
  21. Roelandt JRTC, Di Mario C, Pandian NG, Li W, Keane D, Slager CJ, de Feyter PJ, Serruys PW. Three-dimensional Reconstruction of Intracoronary Ultrasound Images. Rationale, Approaches, Problems and Directions. *Circulation* 1994 (90): 1044-1055.
  22. Bom N, Li W, Gussenhoven EJ, Lancée CT, de Kroon MGM. Intravascular ultrasound: new techniques and possibilities. In: *New trends in vascular exploration, Proceedings of the IV International Meeting on Vascular Hemodynamics* (E. Borgatti, A. de Fabritiis, eds) Torino 1994: 139-145.
  23. Gussenhoven EJ, van der Lugt A, The SHK, Li W, van Egmond FC, Pieterman H, van Urk H. Peripheral Intravascular Ultrasonography. In: *Vascular Diagnostics* (P. Lanzer and J. Rösch, eds). Berlin/Heidelberg 1994: 481-489.
  24. van Egmond FC, Li W, Gussenhoven EJ, Lancée CT. Catheter displacement sensing device. *The Thoraxcentre J* 1994 (6):9-12.

25. van Strijen M, Gussenhoven EJ, van der Lugt A, Li W, The SHK, van Egmond FC, Lancée CT, Stijnen T. Reproduceerbare intravasculaire ultrageluidsbeelden verkregen met een catheterverplaatsingsmeter. *Ultrasonoor Bulletin* 1994 (22): 8-11.
26. Li W, Bom N, van Egmond FC. Three-dimensional quantification of intravascular ultrasound images. *Journal of Vascular Investigation* 1995 (1): 57-61.
27. Li W, Lancée CT, van der Steen AFW, Honkoop J, Gussenhoven EJ, Bom N. Intravascular Ultrasound Image Processing. *Thoraxcentre J* 1995 (3): 34-35.
28. Li W, van der Steen AFW, Lancée CT, Honkoop J, Gussenhoven EJ, Bom N. Temporal correlation of blood scattering signals from intravascular ultrasound. In: *IEEE Ultrasonics Symposium Proceedings 1995*: 1515-1518.
29. Bom N, Li W, Lancée CT. New Developments in Intravascular Ultrasound: Quantitative Aspects. *Proceedings ACCV'95 - Second Asian Conference on Computer Vision, Singapore.1995 (III)*: 278-280.
30. Bom N, Li W, van der Steen AFW, de Korte CL, Gussenhoven EJ, von Birgelen C, Lancée CT. Intravascular Ultrasound, possibilities of image enhancement by signal processing. In: Marwick TH, Reiber JHC, van der Wall EE (eds) *Advances in imaging techniques in ischemic heart disease*. Kluwer Academic Publishers, Dordrecht 1995: 113-125.
31. Bom N, Li W, van der Steen AFW, de Korte CL, Gussenhoven EJ, von Birgelen C, Lancée CT, Roelandt JRTC. Intravascular ultrasound: technical update 1995. In: *Quantitative Coronary Imaging (PJ de Feyter, C di Mario, PW Serruys, eds)*, Barjesteh, Meeuwes & Co., Rotterdam 1995: 89-106.
32. Bruining N, von Birgelen C, Di Mario C, Prati F, Li W, Den Hoed W, Patijn M, de Feyter PJ, Serruys PW, Roelandt JRTC. Dynamic three-dimensional reconstruction of ICUS images based on an ECG-gated pull-back device. In: *Computers in Cardiology 1995*. Los Alamitos: IEEE Computer Society Press 1995: 633-636.
33. Di Mario C, von Birgelen C, Prati F, Soni B, Li W, Bruining N, de Feyter PJ, Serruys PW. Three-dimensional reconstruction of two-dimensional intracoronary ultrasound: clinical or research tool? *Br Heart J* 1995 (73-S2): 26-32.

34. The SHK, Gussenhoven EJ, Pieterman H, van Bortel LMAB, Li W, Roelandt JRTC, de Feyter P, van Urk H. Assessment of regional vascular distensibility in disease iliofemoral arteries by intravascular ultrasound. *Ultrasound Med Biol* 1995 (21):17-24.
35. Gussenhoven EJ, van der Lugt A, Pasterkamp G, van den Berg G, Sie LH, Vischjager M, The SHK, Li W, Pieterman H, van Urk H. Intravascular ultrasound predictors of outcome after peripheral balloon angioplasty. *Eur J Vasc Endovasc Surg* 1995 (10): 279-288.
36. van der Lugt A, Gussenhoven EJ, Stijnen T, Li W, van Strijen M, van Driel E, van Egmond FC, van Suylen RJ, van Urk H. Comparison of intravascular ultrasound findings after coronary balloon angioplasty evaluated in vitro with histology. *Am J Cardiol* 1995 (76): 661-666.
37. Slager CJ, Laban M, Oomen JAF, von Birgelen C, Li W, Krams R, Schuurbiens JCH, den Boer A, Serruys PW, Roelandt JRTC, de Feyter PJ. Three-dimensional geometry and orientation of coronary lumen and plaque. Reconstruction from angiography and ICUS (ANGUS). *Thoraxcentre J* 1995 (3): 36-37.
38. von Birgelen C, Di Mario C, Li W, Prati F, Bom N, Roelandt JRTC, Serruys PW. Three-dimensional reconstruction of intracoronary ultrasound images: technical approaches, clinical applications and current limitations in the assessment of vessel dimensions. In: *Multiple Risk Factors in Cardiovascular Disease - Vascular and Organ Protection* (Gotto Jr AM, Lenfant C, Catapano AL, Paoletti R, eds), Kluwer Academic Publishers, Dordrecht 1995: 267-287.
39. von Birgelen C, Di Mario C, Li W, Slager CJ, de Feyter PJ, Roelandt JRTC, Serruys PW. Volumetric Quantification by Intracoronary Ultrasound: In: *Quantitative Coronary Imaging* (PJ de Feyter, C di Mario, PW Serruys, eds) Barjesteh, Meeuwes & Co., Rotterdam 1995: 211-226.
40. von Birgelen C, Di Mario C, Prati F, Bruining N, Li W, Roelandt JRTC. Intracoronary Ultrasound: three-dimensional reconstruction techniques. In: *Quantitative Coronary Imaging* (PJ de Feyter, C di Mario, PW Serruys, eds) Barjesteh, Meeuwes & Co, Rotterdam 1995: 181-197.

41. von Birgelen C, Di Mario C, Ruygrok PN, Prati F, Li W, Ligthart J, Gil R, de Feyter PJ, Serruys PW, Roelandt JRTC. Assessment of atherosclerotic plaques and coronary interventions by intracoronary ultrasound. *Thoraxcentre J* 1995 (7): 7-12.
42. von Birgelen C, Erbel R, Di Mario C, Li W, Prati F, Ge J, Bruining N, Gorge G, Slager CJ, Serruys PW, Roelandt JRTC. Three-dimensional reconstruction of coronary arteries with intravascular ultrasound. *Herz* 1995 (20): 277-289.
43. Wilson RA, Di Mario C, Krams R, Soei LK, Li W, Laird AC, The SHK, Gussenhoven EJ, Verdouw P, Roelandt JRTC. In vivo measurement of regional large artery compliance by intravascular ultrasound under pentobarbital anesthesia. *Angiology* 1995 (46): 481-488.
44. von Birgelen C, Di Mario C, van der Putten N, Li W, Gil R, Prati F, Ligthart J, Camenzind E, Ozaki Y, Serruys PW, Roelandt JRTC. Quantification in three-dimensional intracoronary ultrasound: importance of image acquisition and segmentation. *Cardiologie* 1995 (2): 67-72.
45. Li W, van der Steen AFW, Lancee CT, Honkoop J, Gussenhoven EJ, Bom N. Temporal correlation of blood scattering signals in vivo on radio frequency intravascular ultrasound. *Ultrasound Med Biol* 1996 (22):583-590.
46. Li W, van der Steen AFW, Lancee CT, Gussenhoven EJ, Bom N. Lumen enhancement and flow estimation by temporal correlation of radiofrequency intravascular ultrasound. In: *Proceedings 18<sup>th</sup> Annual Conference of the IEEE EMBS* 1996: 839.
47. Li W, Lancee CT, van der Steen AFW, Gussenhoven EJ, Bom N. Blood velocity estimation with high frequency intravascular ultrasound. In: *IEEE Ultrasonics Symposium Proceedings* 1996: 1485-1488.
48. Li W, Bom N, von Birgelen C, van der Steen AFW, de Korte CL, Gussenhoven EJ, Lancee CT. State of the art in ICUS quantitation. In: *Cardiovascular Imaging (JHC Reiber & EE van der Wall, eds.) Kluwer Academic Publishers, Dordrecht* 1996: 79-92.



49. Bruining N, von Birgelen C, Mallus M, de Feyter PJ, de Vrey E, Li W, Prati F, Serruys PW, Roelandt JRTC. ECG-gated ICUS image acquisition combined with a semi-automated contour detection provides accurate analysis of vessel dimensions. In: Computers in Cardiology 1996. Los Alamitos: IEEE Computer Society Press 1996: 53-56.
50. von Birgelen C, Di Mario C, Li W, Schuurbiers JCH, Slager CJ, de Feyter PJ, Roelandt JRTC, Serruys PW. Morphometric analysis in three-dimensional intracoronary ultrasound: An In-vitro and in-vivo study using a novel system for contour detection of lumen and plaque. Am Heart J 1996 (132): 516-527.
51. Li W, van der Steen AFW, Lancée CT, Céspedes EI, Carlier S, Gussenhoven EJ, Bom N. Potentials of blood-flow measurement. Semin in Intervent Cardiol 1997 (in press).
52. von Birgelen C, Li W, Bom N, Serruys PW. Quantitative three-dimensional intravascular ultrasound. Semin Intervent Cardiol 1997 (in press).
53. von Birgelen C, de Vrey E, Mintz RS, Nicosia A, Bruining N, Li W, Slager CJ, Roelandt JRTC, Serruys PW, de Feyter PJ. ECG-gated three-dimensional intravascular ultrasound: feasibility and reproducibility of an automated analysis of coronary lumen and atherosclerotic plaque dimensions in humans. Circulation (in press).
54. Li W, Lancée CT, Céspedes I, van der Steen AFW, Bom N. Decorrelation properties of intravascular echo signals (submitted).
55. Li W, van der Steen AFW, Lancée CT, Céspedes EI, Bom N. Estimation of local blood velocity and volume flow with intravascular ultrasound (submitted).
56. von Birgelen C, de Feyter PJ, de Vrey E, Li W, Bruining N, Nicosia A, Roelandt JRTC, Serruys PW. Evaluation of Simpson's rule for the ultrasonic assessment of coronary lumen and atherosclerotic plaque volume: an in vivo study with ECG-gated three-dimensional intravascular ultrasound (submitted).



**CURRICULUM VITAE**

Wenguang Li was born on 19 June, 1961, Guangdong, P.R. China. He studied Radioelectronics in the Physics Department of Fudan University from 1978 to 1982. During the four-year undergraduate program, he became interested in the field of medical instrumentation. After he received the B.S. degree in 1982, he continued his study as a graduate student in the Biomedical Engineering Department, Sun Yet-Sen University of Medical Sciences. In 1985, he received his M.S. degree and was appointed as a researcher at the same department lead by Prof. Y. Wu. During the period of 1985-1989, he worked on several government research projects in application of microcomputer-based techniques for real-time medical instrumentation.

In September 1989, he joined in the cultural exchange program between China and the Netherlands and came to work as a visiting scholar in the project of automatic contour detection of intravascular ultrasound image in the Department of Experimental Echocardiography of Thoraxcentre, under the supervision of Prof. Dr. Ir. N. Bom.

Since May 1992, he is employed by the Interuniversity Cardiology Institute of the Netherlands (ICIN) as a researcher and has been participating in the intravascular ultrasound project supported by ICIN 18 and the Dutch Technology Foundation.

